2009-07-01

Small Antenna Options for Ultra-Wideband (UWB) Applications

David Kearney
Technological University Dublin, david.kearney@tudublin.ie

Small Antenna Options for Ultra-Wideband (UWB) Applications

David Kearney

Small Antenna Options for Ultra-Wideband (UWB) Applications

David Kearney

M. Phil

Supervisor:
Max Ammann

Dublin Institute of Technology

Antennas and High Frequency Research Group

Date: July 2009

Abstract

Ultra-Wideband (UWB) systems provide a means for short range high data rate wireless transmission between electronic devices. Portable devices and in particular, mobile handsets, have the potential to harness the unprecedented connectivity associated with UWB's high speed, low power data transfer.

Over the course of this work, a number of small antenna options for UWB mobile handset applications are presented. Two key subgroups of the 3.1 – 10.6GHz UWB band are chosen and suitable antennas designed for both bands. At the upper end of the band, a ceramic planar inverted-F antenna is proposed to cover band groups 3 & 6 (6.3 – 9GHz). At the lower end of the band, a novel Dual-Band PIFA structure is presented and optimised to cover the band group 1 bands (3.1 – 4.8GHz).

Design work is carried out using CST Microwave Studio simulation software, and all parameter sweeps of critical dimensions are presented, as well as an in-depth examination of E-fields, Surface Currents and Radiation Patterns for both antennas.

Finally measurement prototypes are built up and measured to validate the simulation data. Correlation between measured and simulated results is observed and the performance of the antennas with respect to typical UWB antenna specifications is discussed.

Declaration

I certify that this thesis which I now submit for examination for the award of research masters is entirely my own work and has not been taken from the work of others save to the extent that such work has been cited and acknowledged within the text of my own work.

This thesis was prepared according to the regulations for postgraduate study by research of the Dublin Institute of Technology and has not been submitted in whole or in part for an award in any other Institute or University.

The work reported on in this thesis conforms to the principles and requirements of the Institute's guidelines for ethics in research.

Use of any material from this thesis has to be duly acknowledged.

Signature: _____ Date: _____

David Kearney

Acknowledgements

I would like to express my sincere gratitude to my supervisor Dr. Max J. Ammann for all his support, encouragement and guidance throughout this work. Thanks also to Dr. Patrick McEvoy whose advice and assistance were greatly appreciated.

I would also like to acknowledge the support of TDK Electronics Ireland over the course of this research and in particular Joseph Modro, Gerard Cunningham, Laurence Richard, Denver Humphrey, Pauline O'Riordan, Tom Cooney, Deirdre Hughes and Dr. Stephen Seawright whose experience and assistance over the past 15 months have proved invaluable.

Finally I would like to thank my parents, Sinead and Austin Kearney for their continued support and invaluable advice over the course of this work.

Abbreviations

ADS	Advanced Design System
BBMLA	Broad-Band Meander Line Antenna
CPW	Co-Planar Waveguide
CST	Computer Simulation Technology
DAA System	Detect and Avoid System
DCS	Digital Cellular System
DNG	Double Negative
DRA	Dielectric Resonator Antenna
EIRP	Effective Isotropically Radiated Power
ENG	Epsilon Negative
EM	Electromagnetic
FR4	Flame Retardant 4 (Printed Circuit Board Substrate)
FCC	Federal Communications Commission
GPS	Global Positioning System
GSM	Global System for Mobile Communications
HP	Hewlett Packard
IEEE	Institute of Electrical and Electronic Engineers
LC	Inductor-Capacitor Matching Circuit
LTE	Long Term Evolution
MB-OFDM	Multi-Band Orthogonal Frequency-Division Multiplexing
MLA	Meander line Antenna
NBML	Narrow-Band Meander Line

NIM	Negative Index Material
PCS	Personal Communication Services (Cellular 1850-1990 MHz)
PIFA	Planar Inverted-F Antenna
PTFE	PolyTetraFluoroEthylene (Teflon)
RF	Radio Frequency
SMA	Surface Mount Assembly
TDK	Tokyo Denki Kagaku
UWB	Ultra-Wideband
WLAN	Wireless Local Area Network
WiMAX	Wireless Metropolitan Area Network
WPAN	Wireless Personal Area Network

Contents

Chapter 2: Review of UWB Background & Key Antenna Parameters

Chapter 3: High Band UWB - Antenna Simulation Work

Chapter 4: High Band UWB - Antenna Measurement

Chapter 5: Low Band UWB - Antenna Simulation Work

Chapter 6: Low Band UWB - Antenna Measurement

Introduction

In 2002, the Federal Communications Commission (FCC) approved the operation of Ultra Wideband (UWB) systems within the 3.1 - 10.6 GHz spectrum in the U.S. UWB systems use carrier-based Multi-Band Orthogonal Frequency Division Multiplexing (MB-OFDM) to provide short range, high data-rate wireless transmission. They utilize much broader bandwidths than are used by existing wireless communication services such as Bluetooth & WLAN, enabling unparalleled wireless connectivity between electronic devices. Although UWB as a technology has not yet achieved the high levels of market penetration that were originally expected, it is highly likely that integration of UWB applications into mobile handsets will be pivotal to the realisation of UWB's potential and its ultimate success as a technology.

The following is a review of my research work on small antenna options for UWB applications. It focuses in particular on antenna solutions to support UWB functionality in a portable electronic device such as a mobile phone handset. Firstly, a brief review of classical fundamental limitation theory of electrically small antennas is presented. Work by Wheeler, Chu & McLean is summarised and discussed to give some insight into the challenges associated with designing a small-size, broad-band antenna. Some innovative work being done currently to try and push the boundaries of these theoretical limits is also presented.

A number of small antenna options for UWB mobile handset applications are then researched. Two key sub-bands of the 3.1 – 10.6 GHz UWB spectrum are identified as those most likely to be used for mobile handset UWB applications, and suitable antennas designed to cover these bands. At the upper end of the UWB spectrum, a ceramic Planar Inverted-F Antenna (PIFA) is investigated to cover band groups 3 & 6 (6.3 – 9 GHz). At the lower end of the spectrum, a novel

single-feed dual-Band PIFA structure is presented and optimised to cover the band group 1 bands (3.1 – 4.8 GHz). The proposed antennas are designed within strict size limits, to allow ease of integration into a mobile handset environment. Techniques for negating the de-tuning effects caused by the close proximity of other components within the handset are also discussed.

Design work is carried out using CST Microwave Studio simulation software, and all parameter sweeps of critical dimensions are presented, as well as an in-depth examination of E-fields, surface currents and far-field radiation patterns for the UWB antennas. To validate simulation work, measurement prototypes are built up using a standard ceramic screen-printing process. The prototypes are then measured using a Satimo Starlab 0.8 – 18 GHz near-field measurement chamber, and correlation between measured and simulated results is observed. Finally, the performance of the antennas with respect to typical UWB antenna specifications is discussed.

Chapter 1:
Review of Fundamental Limitation Theory

1.1 Introduction

Interest in the miniaturization of antennas is greater than ever before, as more and more applications such as GPS, Bluetooth, WLAN and UWB are integrated into portable devices such as mobile phone handsets, laptops, MP3 players, cameras & camcorders. UWB applications in particular pose a considerable challenge, with exceptionally demanding requirements on size, bandwidth and efficiency. Ultimately, limitations on these factors are determined by certain theoretical considerations which shall be reviewed.

As early as the 1940s, radiative properties of 'electrically small antennas' were investigated by Harold Wheeler, who first coined the term 'radiation power factor'. His work in 1947 on '*Fundamental Limitations of Small Antennas'* [1] as well as his 1975 paper on '*Small Antennas'* [2], will be reviewed.

Around the same time, L.J. Chu carried out extensive work on the physical limitations of omni-directional antennas [3]. He investigated the relationship between the size of an electrically small antenna, which fits inside a sphere of given radius, and its radiation quality factor, Q. This work was built on by Roger Harrington, who further elaborated on the relationship between size, bandwidth & efficiency [4]. His work in conjunction with Chu's, led to the famous 'Chu-Harrington Limit' for electrically small antennas.

James McLean's '*A re-examination of the fundamental limits on the radiation Q of electrically small antennas'* [5] from 1996, in which he calculates an exact expression for radiation Q (compared to Chu's previous approximation) will also be reviewed. This updated result proves particularly relevant for antennas whose sizes approach $\lambda/2\pi$. (*i.e.* antennas at the upper end of the 'electrically small' range). Further review of this material can be found in [6], [7] & [8].

Finally, some more recent work investigating real broad-band antenna designs which approach these theoretical limits will be reviewed [9], [10]. Some

novel structures, which attempt to optimise the volumetric efficiency (the use of the volume inside the sphere which encloses the antenna), to achieve surprisingly broad bandwidths will be examined, as well as the use of meta-material shells around an antenna to enhance performance.

1.2 Harold Wheeler's Work: 1947-1975

This review references two key papers by Harold Wheeler from 1947 and 1975 [1], [2]. In his work, Wheeler gives a definition for a 'small antenna' and puts forward the idea that the efficiency and bandwidth of an antenna are limited by its 'radiation power factor', which is related to its effective volume, and the volume of a 'radiansphere' at the frequency of operation.

1.2.1 'Small Antenna', Radianlength & Radiansphere

A 'small antenna' is defined as one with maximum dimension 'a', which is less than its radianlength 'l', where the radianlength is equal to $1/2\pi$ times the wavelength of operation of the antenna. Defining 'k' as the wave number associated with the electromagnetic field, $k = 2\pi/\lambda$, we can define a 'small antenna' as one where:

$$a \leq \lambda/2\pi = 1/k, \quad i.e.\ ka \leq 1 \quad (1)$$

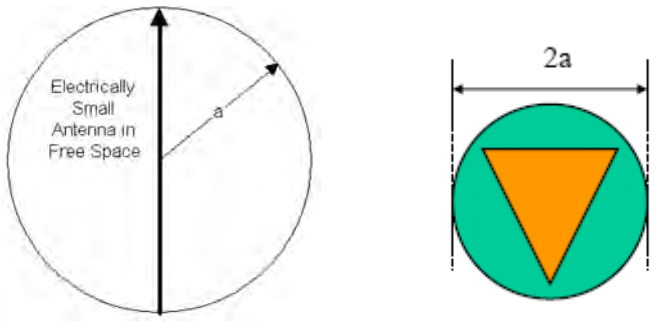

Fig. 1.1: Graphical representations of small antennas ($ka \leq 1$)

In other words, a small antenna is one which fits inside a sphere of radius $a=1/k$. Its greatest dimension is typically less than λ/4. Fig 1.1 gives some graphical representations of small antennas within a sphere of radius '*a*'.

Wheeler then defines a 'Radiansphere' as the spherical volume having radius of one radianlength $l = \lambda/2\pi$. This is the space around the antenna which is mainly occupied by the stored energy of its electric or magnetic field. Inside this sphere the reactive power density exceeds the radiation power density.

1.2.2 'Shape Factor' & Effective Volume of an Antenna

An antenna is essentially a capacitor or inductor which is tuned to resonance by a reactor of the opposite kind. The equations to calculate C and L include a correction factor or 'shape factor' term which depends on the structure of the antenna (*e.g.* capacitive plates or inductive loop). For a capacitive antenna, as in Fig. 1.2a, the shape factor k_a is multiplied by the area A to get the 'effective area', which includes some electric field outside the cylindrical volume of the antenna structure itself. For the inductive antenna, as in fig. 1.2b, the shape factor k_b multiplies the axial length of the cylindrical shape, b, to obtain the effective length of the magnetic path, which is augmented by the external return path. The effective volume of the antenna is then the actual volume of the antenna multiplied by this shape factor.

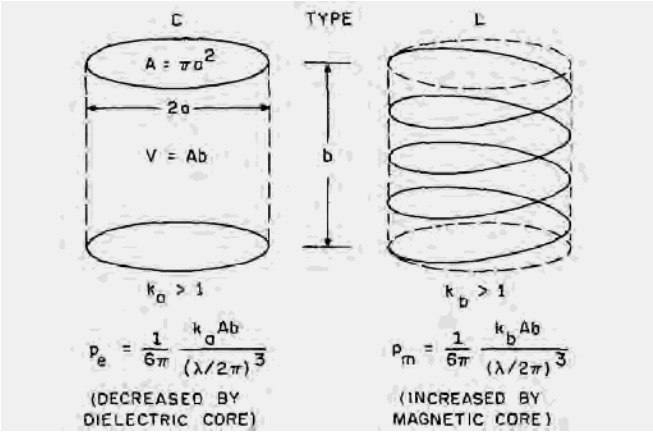

Fig 1.2 (a) Capacitive and (b) Inductive antennas including Radiation Power Factor in terms of effective volume for each type

1.2.3 Radiation Power Factor

The fundamental limitation on the bandwidth and the practical efficiency of a small antenna is the radiation power factor. This term describes the radiation of real power from a small antenna. Its value, except for the shape factor, is the same for both capacitor and inductor type antennas and is always much less than unity due to the small size of the antenna.

If we assume cylindrical antenna volumes, the radiation power factor depends on the ratio of the antenna effective volume $k_a Ab$ (or $k_b Ab$ – where Ab is the volume of the cylindrical antenna) to the cube of the Radianlength l^3.

$$P_{cap} = \frac{1}{6\pi}\frac{k_a Ab}{l^3} \quad , \quad P_{ind} = \frac{1}{6\pi}\frac{k_b Ab}{l^3} \qquad (2)$$

Using the radiation power factor we can calculate roughly what frequency bandwidth a certain size/type of antenna has the potential to give. The nominal or fractional bandwidth of the antenna is the radiation power factor (p) times the frequency of resonance.

Fig. 1.2 above also shows the radiation power factor for each antenna type. Since the radiation power factor is proportional to the effective volume of the antenna, this means it depends on both the antenna volume and the antenna structure (as the structure is taken into account in the shape factor). We can re-write the equation for the radiation power factor in terms of an antenna of spherical volume:

$$P_{cap} = \frac{2}{9}\left(\frac{2\pi.a'}{\lambda}\right)^3 \qquad (3)$$

where *a'* is the radius of the sphere of effective volume. From this it is clear the radiation power factor is proportional to the radius of the sphere of effective volume.

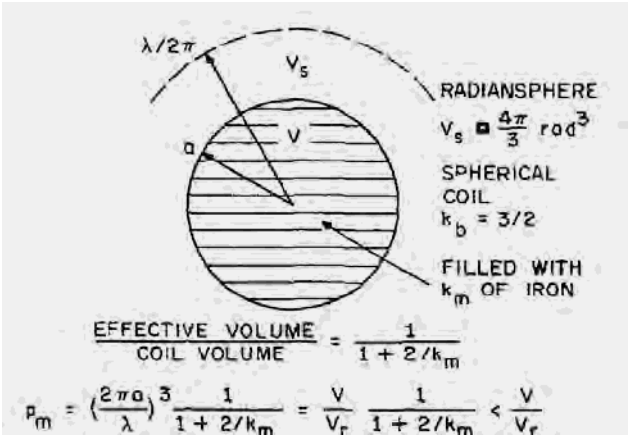

Fig 1.3: Spherical Coil Antenna

Fig. 1.3 shows a spherical coil antenna. Outside the sphere which encloses the antenna structure, stored energy or reactive power fills the radiansphere, but none of this exists inside the antenna sphere. It is this stored energy which poses a fundamental limit on the radiation power factor. The antenna structure itself can be optimised theoretically so there is no stored energy inside this sphere (*e.g.* by filling this sphere with perfect magnetic material), but the stored energy in the 'near-field' (inside the radiansphere, but outside the sphere of effective volume) is unavoidable.

Rearranging the RPF equation above, we can calculate the effective volume of an antenna once we have the radiation power factor;

$$V' = \frac{9}{2} P_{cap} . V_s \quad (4)$$

This is a useful quantity which gives a direct comparison of the bandwidth capability of different structures.

1.3 L.J. Chu's Work: 1948

In his work [3] Chu uses spherical wave functions to describe the antenna fields. He calculates gain G, for an arbitrary antenna and proposes an equivalent circuit for the antenna which can be used to calculate the quality factor, Q, of the antenna. To obtain high gains, the value Q of an antenna will increase incredibly rapidly and this represents a fundamental trade-off between antenna gain and bandwidth. His work, along with the work of Roger Harrington [4] led to the widely-acknowledged Chu-Harrington limit for small antennas.

1.3.1 Spherical Waves and their Equivalent Circuits

As with Wheeler's work, Chu describes an antenna with largest dimension $2a$, which can be enclosed in a sphere of radius 'a'. The field outside this sphere, as a result of some source distribution inside the sphere, can be uniquely expressed in terms of a set of orthogonal spherical vector waves propagating radially outward from the sphere.

It is possible to calculate the total electric and magnetic energy stored outside the sphere, but the total energy calculated in this way has no direct bearing on the performance of the antenna. We need to separate the energy associated with the local field around the antenna from the rest. To do this we reduce the field problem to a circuit problem, where the radiation loss is replaced by an equivalent conduction loss.

Total energy stored outside the sphere is equal to the sum of the corresponding energies associated with each spherical wave, and complex power transmitted across the sphere is equal to the complex powers associated with each spherical wave. Since there is no coupling between any two spherical waves, we can replace the space outside the sphere with a number of independent equivalent circuits**.**

The equivalent circuit consists of independent equivalent circuits for each spherical TM_n wave used to describe the field outside the sphere (see fig. 1.4). The voltage, current and impedance of the equivalent circuit for each wave can be

calculated by equating the complex power associated with the spherical waves to that of the circuits. The voltage is proportional to E_θ and the current is proportional to the magnetic field Hφ of the TM_n wave on the surface of the sphere. Normalized modal impedance Z_n is equal to the normalized radial wave impedance on the surface. The complex power fed into this equivalent circuit is equal to the complex power associated with the TM_n wave.

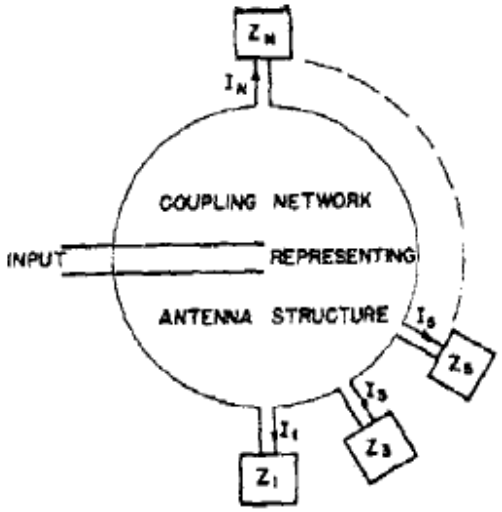

Fig 1.4: Equivalent circuit of a vertically polarized omni-directional antenna

Z_n can be expanded using spherical Bessel functions into a continued fraction form, which can be interpreted as a cascade of series capacitance and shunt inductances terminated with a unit resistance. For the simplest case, $n=1$, (representing a TM wave generated by an infinitesimally small dipole) the equivalent circuit is that of Fig. 1.5.

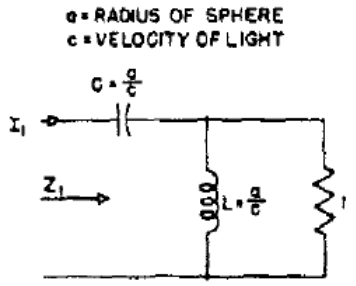

Fig 1.5: Equivalent circuit of electric dipole

1.3.2 Simplified RLC Equivalent Circuit

As '*n*' increases, the complexity of the equivalent circuit increases dramatically, so except for the *n*=1 case, it would be very time-consuming to calculate the total electric energy stored in all the capacitances of the equivalent circuit. To make the calculation more practical, we use a simple RLC circuit as an approximate equivalent circuit for Z_n. The frequency behaviour of this circuit is very similar to the original circuit in and around the operating frequency.

R, L and C for this new simplified circuit are calculated by equating the resistance, reactance and frequency derivative of the reactance of Z_n to those of the RLC circuit. This new simplified circuit is accurate enough to describe Z_n in the immediate neighbourhood of the operating frequency.

1.3.3 Q-factor for the spherical wave based on the simplified equivalent circuit

The Q-Factor Q_n for a spherical travelling wave can be calculated using the equivalent circuit. Later we will combine the Q_ns of all the spherical waves to give us an expression for the Q of the entire antenna. It is important to note that the bandwidth of the equivalent circuit of the TM_n wave is equal to $1/Q_n$, although as the value of Q_n becomes low, this relationship becomes less precise.

As can be seen from fig. 1.6, whenever $\rho = ka = 2\pi a/\lambda$ is greater than the order 'n' of the wave, Q_n is of the order of unity. In this case the stored electric energy in the equivalent circuit is very small, and thus the circuit behaves as a pure resistance. When $2\pi a/\lambda < n$ the circuit behaves as a pure capacitance and Q_n increases incredibly quickly as $2\pi a/\lambda$ decreases.

Rearranging this, it is clear that only when the radius of the sphere $a > n\lambda/2\pi$, will the TM_n wave propagate without a large amount of energy being stored in the neighbourhood of the sphere, *i.e.* when the sphere around the Antenna is too small to support any propagating modes, the Q of the Antenna becomes large, as these modes contribute little real power to radiation.

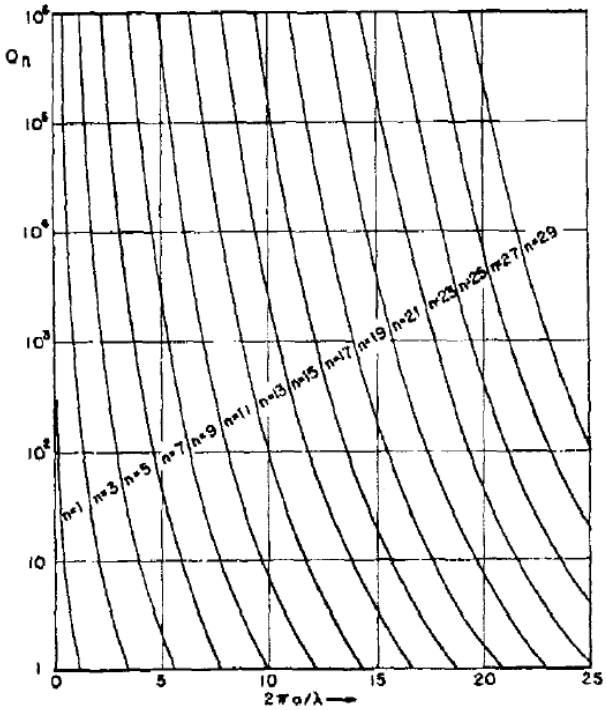

Fig. 1.6: Q_n of the equivalent circuit of TM_n or TE_n wave

1.3.4 Antenna Q-Factor

We can now define antenna Q at the antenna equivalent circuit input terminals:

$$Q = \frac{2\omega \times \textit{the mean electric energy stored beyond the input terminals}}{\textit{power dissipated in radiation}} \quad (5)$$

As we saw before, if the value of Q is high it is equivalent to the reciprocal of the fractional bandwidth of the antenna. If the antenna Q is low, it has a potential to have a broad bandwidth. Summing up the stored electric energy in the simplified equivalent circuits of the spherical waves outside the sphere and the total power radiated, we get the following expression for antenna Q:

$$Q = \frac{\sum{}' A_n^2 \frac{n(n+1)}{2n+1} Q_n(\rho)}{\sum{}' A_n^2 \frac{n(n+1)}{2n+1}} \quad (6)$$

where A_n are complex coefficients, n is the order of the wave, and Q_n are the independent Q's for each spherical wave. Higher modes fade away rapidly for roughly $ka<1$, since ka is basically the ratio of the dimensions of the antenna structure to the wavelength of operation. As the antenna size becomes small compared to wavelength, the structure doesn't allow several propagating modes and thus the higher modes become evanescent. Q for the lowest TM mode becomes:

$$Q = \frac{1+3k^2a^2}{k^3a^3[1+k^2a^2]} \quad (7)$$

Fig. 1.7 shows the Chu-Harrington theoretical limit for a single-mode antenna vs. efficiency based on this expression. Real dipoles and the Goubau clover-leaf

dipole antenna are also plotted (With both a TM and TE mode present, the value of Q would be halved). As $ka<<1$ the equation becomes;

$$Q \cong \frac{1}{k^3 a^3} \quad (8)$$

and the Q varies inversely with the cube of the sphere radius in radian wavelengths. Thus Q grows rapidly as size decreases and this relationship imposes a critical trade-off between bandwidth and size for electrically small antenna.

We can now calculate the lowest possible Q (and hence broadest possible bandwidth) achievable for an electrically small antenna based on its maximum dimension. This result is independent of the actual structure of the antenna inside the sphere (except in relation to which type of spherical mode, (TM or TE) or both, is excited by the antenna).

1.3.5 Efficiency and Fractional Bandwidth and the Trade-Off between the Two

Chu's work so far assumes the antenna has 100% efficiency. If the antenna is lossy however, this will not be the case, and a loss resistance element must be inserted into the equivalent circuit in series with the radiation resistance. Fig. 1.7 shows the Chu-Harrington relationship for several efficiencies. It can be seen that if a lower efficiency is acceptable, Q can be reduced, and hence bandwidth increased. This illustrates the fundamental trade-off between efficiency and bandwidth.

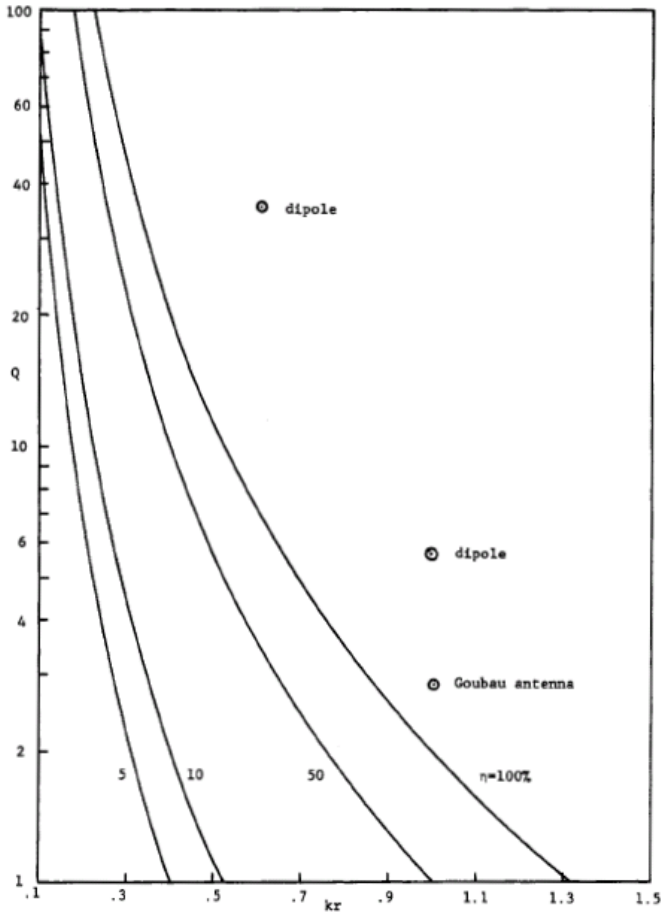

Fig. 1.7: Chu-Harrington Fundamental limitations for single-mode antenna vs. efficiency

Bandwidth is derived from Q by assuming that the antenna equivalent circuit is a resonant circuit with fixed values. Then the fractional bandwidth which is defined as the normalised spread between the half-power frequencies is:

$$Bandwidth = \frac{f_{upper} - f_{lower}}{f_{center}} = \frac{1}{Q} \quad (9)$$

This equation is useful when Q is much greater than 1, as the resonant circuit is a good approximation to the antenna in this case. As Q approaches 2 and below however, the expression becomes less accurate.

Most small antennas do not use the spherical volume efficiently and so, actual antenna sizes tend to be substantially bigger than this theoretical limit. From

this work we can see that improving the bandwidth for an electrically small antenna is only possible by (i) using the volume of the sphere in which it is enclosed as efficiently as possible, or by (ii) reducing the efficiency of the antenna.

1.4 James McLean's Work: 1996

In his work published in 1996 [5], McLean derives an alternative method for the calculation of minimum radiation Q for an antenna to that derived by Chu in the 1940s. This method leads to an exact expression for the radiation Q (compared to Chu's approximate expression) which agrees with Chu's work at the lower limit of electrical size (for very high values of Q), but becomes significantly different at the upper end of the range (as Q approaches 2 and below). McLean puts forward that the bandwidths of antennas near this upper range are limited even further than was originally put forward by Chu.

1.4.1 Chu's Approximate Theory

Chu calculates the radiation Q of an antenna by deriving an equivalent ladder network circuit for each spherical waveguide mode. He then simplifies the calculation by replacing the ladder network with a second order RLC circuit to allow ease of calculation for higher order modes. He assumes this circuit behaves as a lumped second order network over some limited range of frequency. This is a significant approximation to make and leads to an approximate expression, which appears to have an algebraic error present. Chu's expression for Q:

$$Q = \frac{1 + 3k^2a^2}{k^3a^3[1 + k^2a^2]} \quad (10)$$

differs from that obtained from his equivalent second order network, which gives.

$$Q = \frac{1 + 2k^2a^2}{k^3a^3[1 + k^2a^2]} \quad (11)$$

The two expressions are similar for lower values of *ka* (high *Q*) but begin to differ towards the upper limit of *ka* (*i.e.* as it approaches 1)

1.4.2 McLean's Exact Derivation of Radiation Q from Non-Propagating Energy

To derive his exact expression McLean begins with the fields of the TM_{01} mode. The field components Hφ, Eθ & Er can be calculated from an r-directed magnetic vector potential A_r, and from these field components, the total electric- and magnetic-energy densities ω_e and ω_m can be calculated. The electric-energy density expression is given as:

$$\omega_e = \frac{1}{2}\varepsilon\left(|E_\theta|^2 + |E_r|^2\right) \quad (12)$$

The propagating energy density ω_e^{rad} (the electric energy density which is associated with the travelling wave, *i.e.* the energy calculated from the field components which produce radiated power) can also be calculated. This energy density is computed using only the radiation fields.

From these expressions, the non-propagating electric-energy density $\omega_e^{'}$, which is the difference between the total electric-energy density ω_e and the propagating electric-energy density ω_e^{rad} can be calculated. Integrating this we can calculate the non-propagating electric energy $W_e^{'}$. We get;

$$W_e^{'} = \frac{4\pi\eta}{3\omega}\left[\frac{1}{k^3a^3} + \frac{1}{ka}\right] \quad , \ \eta = \sqrt{\frac{\mu}{\varepsilon}} \quad (13)$$

Total radiated power can be found by integrating the real part of the Poynting vector over a spherical surface of any radius, which gives:

$$P_{rad} = \frac{8\pi}{3}\eta \quad (14)$$

The quality factor Q is then;

$$Q = \frac{2\omega W_e^{'}}{P_{rad}} = \frac{1}{k^3 a^3} + \frac{1}{ka} \quad (15)$$

Alternatively, the Q Factor associated with the TM_{01}can be calculated easily from Chu's equivalent ladder network for this mode. Total electric energy stored in the circuit is;

$$W_e^{'} = \frac{1}{2} C \left| V_c \right|^2 = \frac{1}{2\omega} \frac{1}{ka} \quad (16)$$

Power dissipated in the resistor is:

$$P_r = \left| I_r \right|^2 R = \frac{k^2 a^2}{1 + k^2 a^2} \quad (17)$$

And Q is again:

$$Q = \frac{2\omega W_e}{P_r} = \frac{1}{k^3 a^3} + \frac{1}{ka} \quad (18)$$

Fig. 1.8 plots this newly derived exact expression vs. Chu's original approximate expression. It is clear from the graph that while the two expressions for Q agree for very small values of ka, as ka increases the expressions diverge, with the new expression giving a higher minimum value for Q (and hence smaller achievable bandwidth) than the original Chu hypothesis.

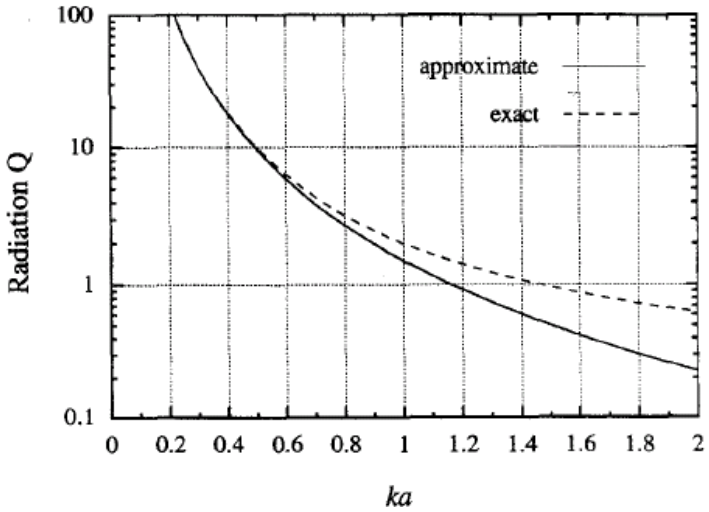

Fig. 1.8: Minimum Radiation Q vs. ka associated with TE01 or TM01 spherical modes; shows difference between Chu's approximate expression and McLean's exact expression

1.5 Recent work on approaching theoretical limits

1.5.1 Optimising Volumetric Efficiency (SkyCross)

SkyCross is a company which specializes in the design and manufacture of high performance antenna solutions for a variety of wireless device applications. They have developed a patented 'Meander Line Antenna' (MLA) structure [9] to offer broad and narrow-band solutions which approach the theoretical limitations on size vs. bandwidth.

Fig. 1.9 plots normalized antenna volume vs. fractional bandwidth for some SkyCross antennas vs. some reference antenna structures. Chu's theoretical limit is equivalent to the 100% efficiency line. As can be seen from the figure, some antenna structures such as the patch and dipole do not even approach Chu's theoretical limit, their structures not using the volume surrounding the antenna efficiently enough. The SkyCross Narrow-Band (NBML) and Broad-Band Meander Line (BBMLA) type antennas on the other hand, achieve performance very close to the theoretical Chu-Harrington limit. They do this through their high volumetric efficiency (*i.e.* they provide the most effective use of the physical

volume surrounding the antenna). All MLA antennas shown, exhibit a smaller physical volume for a given bandwidth than their generic counterparts.

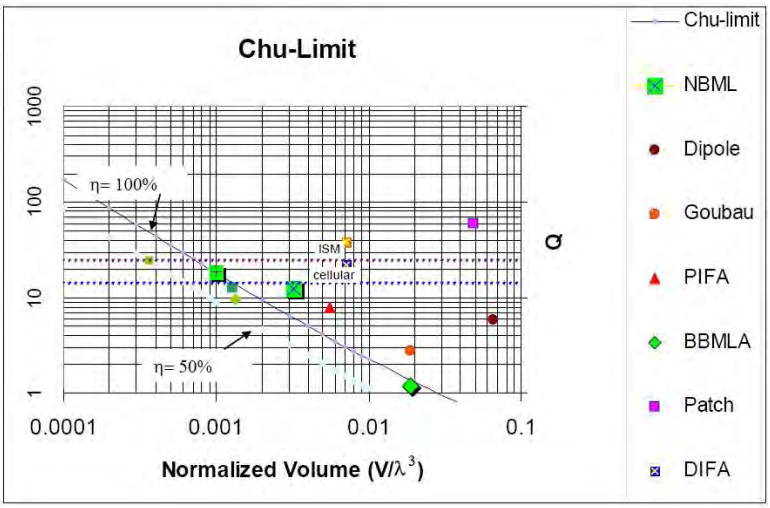

Fig. 1.9: Normalized volume vs. fractional bandwidth for a range of existing antenna types including SkyCross 'Meander Line Antenna' (MLA) designs

Efficiency also regulates the size limit, and thus having a reduced efficiency specification can provide greater bandwidth for a given size, or allow for a smaller antenna for a given bandwidth. Fig. 1.9 above also shows the Chu-limit for 50% efficiency.

1.5.2 Meta-materials

Recent work has been carried out by Ziolowski and Erentok [10] which uses 'Meta-material' shells around an antenna structure to reduce the overall size of an antenna and thus approach Chu's theoretical limit.

Meta-materials are artificial materials with unusual electromagnetic properties that are not found in naturally occurring materials. All 'natural' materials such as glass, diamond, etc., have positive electrical permittivity, magnetic permeability and index of refraction. These new artificially fabricated

materials however - termed as negative index (NIM) or double negative (DNG) materials – have negative material parameters. This creates the potential for new kinds of miniaturized antennas and microwave components to be created.

A standard electrically small dipole is a very inefficient radiator due to its small radiation resistance and large capacitive reactance. It is possible to match the dipole to improve its performance by adding an inductor and quarter-wave transformer, but these extra elements increase the overall size of the antenna network. Ziolowski and Erentok propose to surround the electrically small dipole in a meta-material environment, such as an isotropic, homogenous and dispersionless Epsilon Negative (ENG - negative permittivity) or a Double Negative (DNG) shell. This meta-material shell acts in essence as a distributed matching element which supplies complete resistive and reactive matching and thus an efficient electrically small radiating system can be achieved.

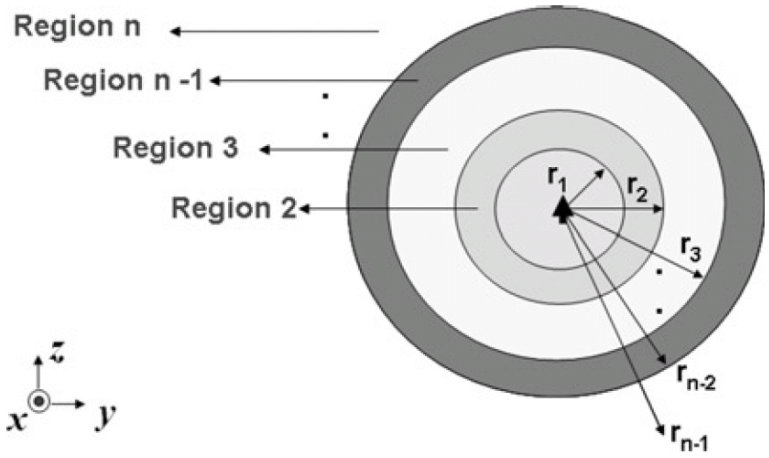

Fig.1.10: Infinitely small dipole in meta-material shell system

It was demonstrated analytically that if the ENG was treated as a frequency-independent medium, the predicted fractional bandwidths were significantly larger than those predicted by the Chu limit. However, it was also shown that if the more

realistic dispersion properties of the ENG shell were included, the high overall efficiency remained at the operating frequency, but the fractional bandwidths were reduced significantly, while still being slightly larger than those predicted by the Chu limit.

1.6 Conclusions / Summary

After a review of the key theory behind the fundamental limitations of realisable 'electrically small' antennas it is clear there will always be a trade-off between size and bandwidth, gain and efficiency. Wheeler's 'radiation power factor' (*P*) is an important one since the fractional bandwidth of the antenna is the radiation power factor times the frequency of resonance. The RPF depends on the shape, volume and radianlength of an antenna and is given by the expression:

$$P_{cap} = \frac{1}{6\pi}\frac{k_a Ab}{l^3} \quad (2)$$

The Chu-Harrington limit represents the fundamental theoretical limit on the size and bandwidth of all electrically small antennas. The closer an antenna approaches this limit the broader the bandwidth for a given size, or the smaller the size for a given bandwidth. Only by using the sphere which encloses the antenna as efficiently as possible, can we approach this theoretical limit. The expression for *Q* for the lowest TM mode as ka<<1 is:

$$Q \cong \frac{1}{k^3 a^3} \quad (8)$$

and since *Q* is inversely proportional to the fractional bandwidth of the antenna, this represents a fundamental trade-off between size and bandwidth for a small antenna.

McLean's more recent work gave us an expression for Q which agrees with Chu's for very small values of ka. As ka increases however, the expressions diverge, with the new expression giving a higher minimum value for Q (and hence smaller achievable bandwidth) than Chu originally hypothesised:

$$Q = \frac{2\omega W_e}{P_r} = \frac{1}{k^3 a^3} + \frac{1}{ka} \quad (18)$$

With the growing need for broad-band small-size antennas to provide a wide range of functionality in today's portable electronic devices, reaching this theoretical limit is more important than ever. Antenna designers have taken to using novel strategies such as volumetric efficiency optimisation and meta-material shell enhancement to approach as close as possible these theoretical limits.

Chapter 2:
Review of UWB Background & Key Antenna Parameters

2.1 Introduction

In this chapter the history and applications of Ultra-Wideband (UWB) as a technology are reviewed. A detailed background of UWB is given and UWB integration into mobile handsets in particular, is discussed. The various UWB band groups which will be used by mobile handset manufacturers are detailed as well as the respective antenna design challenges associated with each.

The main part of the research work that follows involves the investigation and design of two UWB antennas. The first, (A), is a ceramic chip Planar Inverted-F (PIFA) antenna for use with UWB band groups 3 & 6 (6.3 – 9 GHz). A strict limit on the overall volume of the ceramic block of 60mm^3 is imposed and the resulting performance characteristics are presented and discussed. The second, (B) is a novel dual-PIFA design for use with band group 1 (3.1 – 4.8 GHz). A limit on the overall volume of the ceramic block of 350 mm^3 is imposed for this antenna and the resulting performance characteristics are presented and discussed. The reasons behind choosing ceramic chip type antennas, as well as reasons for employing PIFA structures to meet the demanding UWB requirements are explained.

A review of the key antenna characteristics which will be used as metrics in the research work that follows is also presented. Critical parameters such as antenna gain, efficiency, directivity & far-field radiation pattern as well as Effective Isotropically Radiated Power (EIRP), which is critical to ensure the antenna remains within specified regulatory limits, are defined and discussed.

2.2 Ultra Wideband Background

2.2.1 Ultra-Wideband History & Applications

The Federal Communications Commission (FCC) approved the operation of UWB systems within the 3.1 - 10.6 GHz spectrum in the US in 2002. The spectrum is divided into six band groups as illustrated in fig. 2.1 (band group 6 overlapping band groups 3 & 4). Since UWB services occupy a wide band in the RF spectrum, there is great potential for high data-rate transmission. Also, since UWB radiated power levels tend to be lower than the minimum sensitivity of most electronic devices, UWB devices do not interfere with other narrow-band services operating within the same bands. As described in [11], UWB systems can transmit data up to 200 times faster than existing Bluetooth systems and are between five and 10 times more power-efficient than WLAN.

As well as the potential for extremely fast data rates and negligible interference with narrow-band systems, UWB also has the advantages of immunity to interference and multipath fading, as well as very low battery power consumption due to its low transmit-power. The most common UWB implementation uses the WiMedia Alliance's Multi-Band Orthogonal Frequency-Division Multiplexing (MB-OFDM) standard.

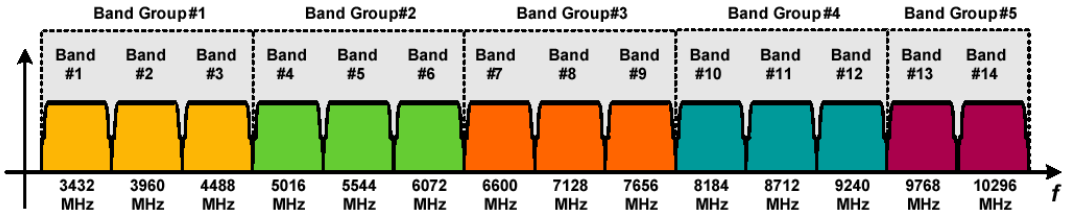

Fig. 2.1: FCC approved UWB Band Groups

UWB systems are best suited to short-range, indoor applications such as Wireless Personal Area Networks (WPANs) in homes. Since UWB has a far greater bandwidth than technologies such as Bluetooth and WLAN, UWB has the potential to allow a whole new level of wireless connectivity. It enables the

efficient transfer of data from digital imaging devices, wireless connection of printers and other peripherals to personal computers and the high-speed transfer of files between portable devices such as mobile handsets & MP3 players. It also allows the wireless connection of DVD players, BluRay™ players etc. to TV sets. This unparalleled wireless connectivity dispenses with the need for cables and eliminates the lack of mobility that is typically associated with the connection of numerous devices.

2.2.2 UWB Integration into Mobile Handsets

There is a belief by many in the industry [12], [13] that real market acceleration for UWB will only occur when UWB becomes integrated into mobile handsets, where it will be used (possibly combined with Bluetooth), to transfer music, pictures and video files at much higher data rates than exist at present. As described in [14], UWB integration into mobile handsets will allow users to create a wireless 'bubble' around them wherever they go, which will automatically connect to applications within its vicinity. This will allow instantaneous connectivity between mobile handsets and other devices such as computers, stereos, printers, TV screens and other mobile handsets. Since the space available within a mobile handset is extremely limited, an antenna solution to support UWB functionality within a mobile handset must exhibit reliable broadband performance while maintaining a very small physical size.

2.2.3 High Band UWB - Band Groups 3 & 6

The current global economic climate has caused a major slow-down in the growth of UWB as a technology, as handset manufacturers adopt a distinctly more cautious approach to next generation products. The likelihood is however, that UWB functionality will eventually be incorporated into handsets using some combination of Band Groups 1, 3 & 6, which would enable globally compatible products. Although the FCC authorized the unlicensed use of the entire 3.1 – 10.6

GHz band for UWB in the U.S. in 2002, disagreements globally over what quantifies 'harmful interference' between radio services operating in close proximity, has made it difficult to convince other territories to authorize use over such a large bandwidth.

Above 6GHz there are more bands available and these bands also tend to be less restricted, so the potential channel capacity is greater in the higher bands [15]. There are also less existing narrow-band services operating at the higher frequencies, so potential for interference issues is greatly reduced (although a 'detect and avoid' system has been proposed [16] to allow the co-existence of UWB and WiMAX at the lower bands). Bands above 6GHz also have the benefit of a smaller wavelength of operation and thus a smaller antenna size. For these reasons, band groups 3 & 6 (6.3 – 9 GHz) look like very likely candidates for UWB mobile handset integration.

2.3 UWB Antenna Design

2.3.1 Ceramic Chip Antenna

Within the scope of this research, it is proposed to investigate the potential of a number of ceramic chip type antennas to support UWB functionality within a mobile handset environment. Ceramic chip antennas were researched due to their low cost, small size, good mechanical strength and relative versatility compared to other mountable antennas. A ceramic chip antenna is manufactured using a screen-printing process, which involves printing aluminium patterns onto the six faces of a ceramic block substrate to create a pseudo-3-D structure. The ceramic block can then be easily mounted at any location on a mobile handset wiring board. Ceramic antennas also have the potential to harness the dielectric loading properties of the ceramic block to load the frequency of operation of the antenna, allowing lower frequency performance to be achieved without requiring an increase in the physical size of the chip. The type of ceramic material used is therefore critical to the design.

2.3.2 Planar Inverted-F Antenna (PIFA)

Mobile handset manufacturers such as Nokia, Sony Ericsson etc. tend to favour antennas which can be mounted directly onto a ground plane. The reason for this is that it allows them to populate the area on the underside of the board directly under the antenna with other components. This, in effect, halves the overall volume required by the antenna. For this reason a Planar Inverted-F Antenna (PIFA) type structure was chosen for its combination of low profile, good impedance control and 'on-ground' type structure.

The evolution of the design of a PIFA is detailed in [17] and can be summarised as follows: An ideal infinitesimally small dipole, which will have perfect omni-directional radiation, can be replaced by a quarter-wave wire monopole above a ground-plane (where the ground acts as a reflector) to achieve the same performance. Now if this monopole is folded by 90°, its overall height can be reduced while still maintaining good performance. Then by introducing a shorting pin connecting the monopole to ground, impedance matching at the input can be improved. Finally if the wire is replaced by a planar radiating patch, fed through the ground plane by a feeding pin, the overall bandwidth of the antenna can be enhanced. Fig. 2.2 shows the structure of a standard PIFA.

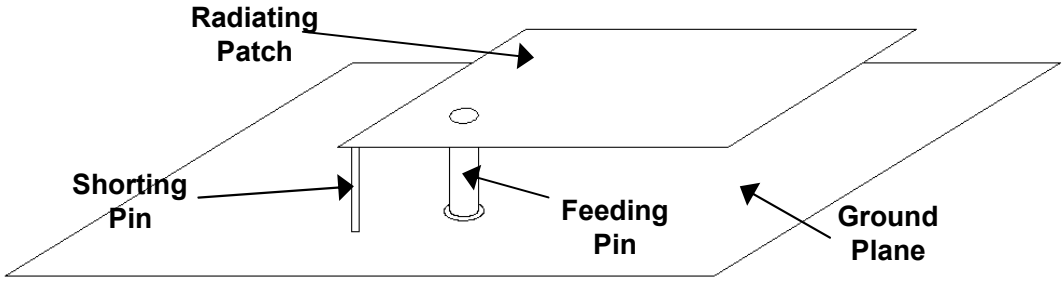

Fig. 2.2: Planar Inverted-F Antenna (PIFA) structure

Without the shorting pin connecting the radiating element to ground, the antenna is a simple microstrip 'Patch' antenna, as described in [18]. Microstrip patch antennas are low profile and inexpensive to manufacture but have the major

disadvantage of high Q (and thus extremely low bandwidth as discussed in Chapter 1). Adding the shorting pin to allow for impedance control at the input however, can significantly improve the bandwidth.

This impedance control is critical since the patch is a quarter-wave resonator and at resonance will have a high voltage and low current, (and therefore a very high impedance), at its open-circuit end. At the input to the antenna, the opposite case will be true and a very low impedance will be evident. Since the antenna will typically be connected to a 50Ω system, adding a shorting connection to the antenna (which becomes the low impedance point) and then adjusting the position of the feed to the point which provides the best 50Ω match, allows us to optimise the input match and thus the overall impedance bandwidth of the antenna.

PIFA antennas are popular choices for integration into mobile handsets due to their low profile, low cost and relatively low design-complexity. As mentioned before, since the PIFA can be printed onto a ceramic block, the dielectric loading properties of the block can be harnessed to further reduce size or improve performance at the lower band edge. It is worth noting however, that historically PIFAs have mainly been used in narrow-band systems such as Cellular & Bluetooth [19], [20], where the required bandwidth of operation of the antenna is much lower than required for UWB. Typical UWB antennas tend to be printed monopoles with very broad bandwidths as in [21], [22], but these types of antennas do not allow ground plane running underneath them and tend to be too large for mobile handset integration.

A lot of work has been carried out in the area of PIFA bandwidth enhancement, for example by optimising the widths of the feed and shorting plates as in [23] or by creating a tunable antenna type structure as in [24]. These structures tend to be very large in size however and are therefore unsuitable for mobile handset integration.

In the first half of this research the ceramic block around which the PIFA is built is used to achieve the maximum bandwidth possible while maintaining the specified size necessary for integration into a mobile handset. This is achieved by allowing the ceramic block to not only dielectrically load the PIFA, but also to resonate itself. Thus the block acts as a Dielectric Resonator Antenna (DRA) as

described in [25] and contributes to the overall radiation performance of the antenna.

2.3.3 Dual-Band PIFAs

Dual-band PIFAs as described in [26] have been investigated mainly as a solution to provide multi-band operation for applications such as cellular where an antenna which performs well at GSM, DCS & PCS bands is highly desirable. An interesting switchable-feed triangular PIFA design is presented in [27] for example, which allows both multi-band and broadband performance. However, its large size makes it unsuitable for mobile handset integration. Some other dual and multi-band PIFA designs can be found in [28], [29].

In the second half of this research, the possibility of using a dual-band PIFA antenna to provide a single broadband UWB response by combining separate narrow-band resonances is investigated. The aim of the research is to determine whether a dual-band PIFA can be designed to cover the UWB band group 1 bands while maintaining a size small enough to be suitable for mobile handset integration

2.4 Antenna Characteristics

The characteristics to be considered when evaluating an antenna's performance are described below. In particular, how they relate to UWB antennas is discussed. Typical target specifications for UWB operation are given for each parameter, based on current industry guidelines. These specifications will be used as a reference for the antenna research and design work which follows. In addition to the parameters mentioned below, an in-band VSWR of 3:1 (which corresponds to a return loss of greater than 6dB) or better, is desirable across the bandwidth of operation.

2.4.1 Antenna Efficiency

The radiation efficiency of an antenna is defined as the ratio of the power radiated by the antenna to the power at its input terminals. It is a measure of how efficiently an antenna radiates its input power as RF energy. When given in terms of a percentage, an antenna efficiency of 0% means all power absorbed by the antenna at its input is effectively lost within the device and no useful radiation occurs. An efficiency of 100% refers to a perfectly radiating antenna wherein all power absorbed at the input is radiated.

The term 'radiation efficiency' includes both conduction efficiency and dielectric efficiency, but does not take into account losses caused by mismatch at the antenna input. Radiation efficiency plus these mismatch losses (sometimes referred to as reflection efficiency) gives the 'total efficiency' of the antenna. At present, mobile handset manufacturers specify a total efficiency of around 55% (-2.5dB) or greater across the band of operation for a UWB antenna.

2.4.2 Antenna Directivity

As described in [18], antenna directivity is defined as the ratio of the radiation intensity measured in a certain direction from the antenna to the intensity which would be measured if the antenna radiated uniformly in all directions. The average radiation intensity is equal to the total power radiated by the antenna divided by 4π. This can be written as

$$D = \frac{U}{U_O} = \frac{4\pi U}{P_{rad}} \quad (19)$$

where U = radiation intensity, U_o = radiation intensity of an isotropic source and P_{rad} = total radiated power. Directivity is an important consideration when designing a UWB antenna for use in a mobile handset as it is critical for the

antenna to have as omni-directional a response as possible. High directivity in a particular direction is undesirable as the location and orientation of the handset will be constantly changing, necessitating an antenna which radiates well in all directions.

2.4.3 Antenna Gain

Antenna gain is a measure of both the directivity and efficiency of an antenna. It is defined as the ratio of the intensity radiated by an antenna in a given direction at an arbitrary distance, to the intensity that would be radiated at the same distance, by a hypothetical lossless isotropic antenna with the same input power. The radiation intensity corresponding to the isotropically radiated power is equal to the power accepted (input) by the antenna divided by 4π. Thus we can write gain, *G*, as;

$$G = 4\pi \frac{U(\theta,\varphi)}{P_{in}} \quad (20)$$

Since the radiated power, P_{rad}, is equal to the antenna radiation efficiency by the input power, P_{in},:

$$P_{rad} = Eff_{rad}.P_{in} \quad (21)$$

from equations (19),(20) and (21) we get that:

$$G = Eff_{rad}.D \quad (22)$$

Unless otherwise stated, 'gain' refers to the maximum gain of the antenna in some direction. An antenna with low gain will tend to be omni-directional, while an antenna with high gain will tend to be more directive and radiate a large amount of its power in a certain direction or directions. As with the radiation efficiency described above, the IEEE standards state that "gain does not include losses arising from impedance mismatches and polarization mismatches".

For all real antennas, the measured average gain, which is the gain averaged over the full 3D sphere, will always be lower than 0dBi since the gain of an antenna is a passive phenomenon, *i.e*. power is not added by the antenna, but simply redistributed to provide more radiated power in a certain direction than would be transmitted by an isotropic antenna. If an antenna has a positive gain in some directions, it must have a negative gain in other directions, as energy is conserved by the antenna.

Maximum antenna gain is of particular importance for UWB applications since the regulatory bodies of each country tend to restrict the power levels of UWB transmitters to avoid interference with narrow-band services operating within the same bands. This is discussed more in section 2.4.5.

2.4.4 Radiation Pattern

The Radiation Pattern of an antenna is a 3-dimensional graphical representation of the relative field strengths of the fields emitted by the antenna. It can also be thought of as the locus of points around the antenna which have the same electric field. It takes the form of a geometrical pattern and allows us to easily visualize the direction of peak gain of the antenna, as well as any nulls in the antenna's characteristic. It also gives an indication of how omni-directional or directive the antenna is overall. It can be plotted in 3D or as 2-dimensional cuts of the 3D sphere, using polar coordinates.

2.4.5 Effective Isotropically Radiated Power (EIRP)

The restrictions on the maximum gain of antenna as described in section 2.4.3 are actually enforced on the Effective Isotropically Radiated Power (EIRP) of a UWB transmitter. The EIRP of a transmitter (including the antenna) is the apparent power transmitted towards the direction of maximum antenna gain, if it is assumed that the antenna is isotropic and radiating equally in all directions. Thus the EIRP is given by the product of the maximum antenna gain and the transmitter power (in

reality, the actual antenna will not be radiating isotropically and so EIRP is just a theoretical measure of energy). The regulator for a particular piece of spectrum will limit the EIRP because it gives a good indication of the possibility of interference to services on similar frequencies.

The 'EIRP Density' is the EIRP spread over a given bandwidth. The spectrum regulatory body of each country restricts the EIRP density of various frequencies to accommodate needs of users and avoid RF interference. In Europe, the European Commission (EC) has applied an EIRP density limit of -41.3dBm/MHz on UWB transmitters in the 6 - 8.5 GHz band (see fig. 2.4 for EC EIRP restrictions on other UWB bands [30]). The FCC has applied similar restrictions in the U.S. but over a broader frequency range. Since the EIRP of the transmitter is directly proportional to the maximum gain of the antenna, measures must be taken to ensure this gain is kept within specifications. Thus it is desirable for a UWB antenna to have a high efficiency but a relatively low maximum gain. This suggests the need for a suitable omni-directional far-field radiation pattern. Details of how to measure the EIRP compliance of UWB devices are described in [31].

2.5 Summary

The reasons for choosing a ceramic chip antenna solution for UWB mobile handset integration have been discussed. The low cost, small size, good mechanical strength and relative versatility compared to other mountable antenna options make ceramic chip antennas a good choice for mobile handset applications. Size in particular is critical for a portable device and use can be made of the dielectric loading properties of the ceramic block to facilitate a small-size low-profile solution. The antenna pattern will be printed on a ceramic block substrate using standard aluminium screen printing process.

Also, the reasons for choosing a Planar Inverted-F Antenna (PIFA) structure have been discussed. The PIFA allows for an on-ground type antenna, which takes up minimum room within the handset and provides for impedance control which permits the maximum bandwidth to be achieved from a relatively

small physical size.

Finally, the critical antenna performance characteristics such as antenna gain, efficiency, directivity and radiation patterns which will be measured within this research work have been described. The importance of Effective Isotropically Radiated Power (EIRP), which is critical to ensure the antenna remains within regulatory limits, has also been reviewed.

EC EIRP Restrictions within UWB Spectrum		
Frequency Range (GHz)	**Maximum mean EIRP density (dBm / MHz)**	**Maximum peak EIRP density (dBm / 50MHz)**
Below 1.6	-90	-50
1.6 to 3.4	-85	-45
3.4 to 3.8	-85	-45
3.8 to 4.2	-70	-30
4.2 to 4.8	-41.3 (until December 31, 2010)	0 (until December 31, 2010)
	-70 (beyond December 31, 2010)	-30 (beyond December 31, 2010)
4.8 to 6.0	-70	-30
6.0 to 8.5	-41.3	0
8.5 to 10.6	-65	-25
Above 10.6	-85	-45

Fig. 2.4: European Commission EIRP Restrictions on UWB systems
(Source: European Commission, Radio Spectrum Policy Unit [30])

Chapter 3:
High Band UWB - Antenna Simulation Work

3.1 Introduction

An antenna design is researched for use in a mobile handset environment to enable UWB functionality at band groups 3 & 6 (6.3 – 9 GHz). The antenna will have a Planar Inverted-F Antenna (PIFA) structure and be printed on a ceramic chip substrate. It is required to meet standard UWB specifications of -6dB S11 or better and 50% efficiency or greater across the bandwidth of interest, while maintaining an overall volume of less than $60mm^3$. As discussed before, the antenna far-field radiation pattern must also be omni-directional. This is to allow reliable performance as the handset orientation and location are changed, as well as to regulate the maximum gain of the antenna to enable it to remain within specified EIRP limits. This chapter deals with the simulation work involved in researching and optimising this design, using the Computer Simulation Technology (CST) Microwave Studio electromagnetic simulation package.

The creation of a parameterized antenna model within CST is discussed as well as the set-up of the simulation environment surrounding the antenna. This includes the creation of models for the mobile handset test board, feed-line, connector, etc. A detailed review of the key parameter sweeps then follows. Parameter sweeps are a very useful way of optimising the critical dimensions of the design and parameters such as dielectric constant of the ceramic block, the block length, height and width, the feed position, etc. are all optimised in this way. The final optimised PIFA design is then presented along with simulated in-band efficiency and S11 data.

An external matching technique is then described to further optimise the antenna response. Results for the matched antenna are presented. Furthermore, to gain some more insight into the operation of the antenna, a detailed field and current analysis is carried out at the resonant frequencies. CST Microwave studio allows detailed analysis of E-fields & surface currents (which can be animated as

the phase is cycled). Finally, the far-field radiation patterns of the design are observed and discussed.

3.2 CST Simulation Model Set-Up

The CST Microwave Studio electromagnetic simulation package allows full 3D simulation of an antenna structure and uses a unique meshing and sub-gridding technique to accurately simulate the antenna performance and calculate a range of parameters including far-field radiation pattern, gain, efficiency (radiation and total), input impedance, return loss, etc. It also provides animated graphical analysis of electric and magnetic fields & surface currents at the frequencies of interest.

As a starting point, a model of a mobile handset wiring board was built up in CST. This model consists of a 40mm x 80mm FR4 substrate (1mm thick) with copper ground planes mounted on both sides, connected together by a number of copper vias running through the FR4 (see fig. 3.1). The board size and layer stack correspond to the dimensions of a typical mobile handset wiring board. The preferred location for the antenna to achieve maximum performance is in the top left corner of the board.

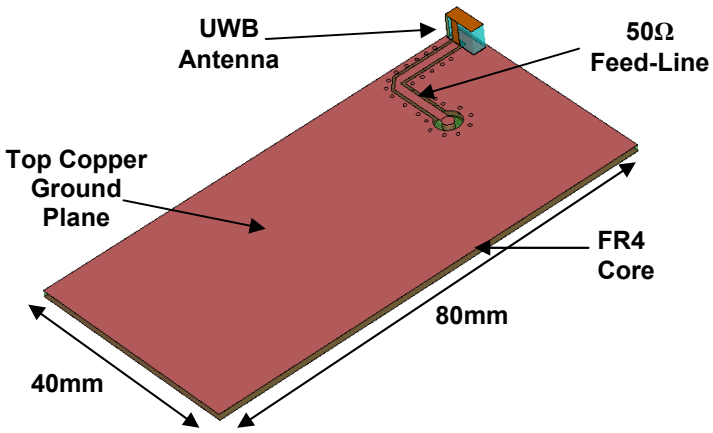

Fig. 3.1: CST Simulation model of 80mm x 40mm mobile handset test board including feed-line and mounted antenna

CST models were also created for a 50Ω ground-backed Co-Planar Waveguide (CPW) 'feed-line' (see fig. 3.2) which incorporates a 90° bend, and an SMA connector with a PTFE core (see fig. 3.3a) mounted on the underside of the board. The SMA pin is fed through the FR4 and the feed-line connects the antenna to this pin. The antenna model is then excited by adding a waveguide port at the end of the SMA connector (see fig. 3.3b). The reason for the presence of the SMA connector in the simulation model is that an equivalent connector in the measurement set-up will allow connection to the appropriate measurement equipment (network analyser, near-field measurement chamber, etc.).

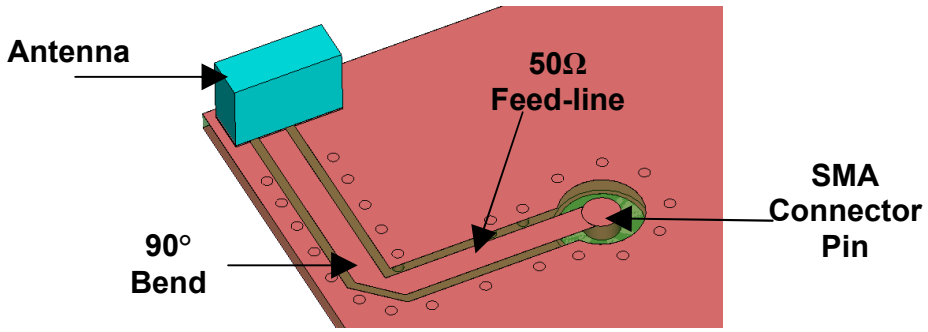

Fig. 3.2: CST Simulation model for 50Ω ground-backed coplanar waveguide 'feed-line' which incorporates a 90° bend

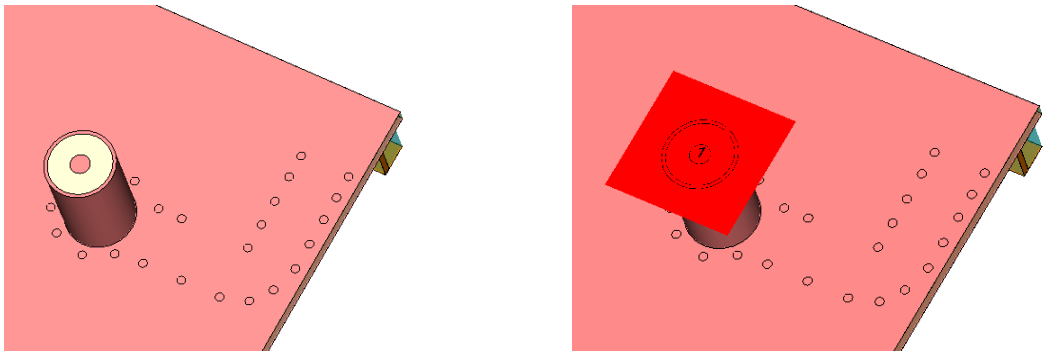

Fig. 3.3 (a): CST model of SMA connector with a PTFE core on underside of test board. 6 (b): SMA connector with waveguide port attached which will excite antenna during simulation

The feed-line and SMA connector models represent as closely as possible the actual feed-line and connector which will be used on the test board to measure the antenna prototypes. Creating accurate simulation models for them at this point will be invaluable when correlating simulated and measured results later on.

Due to the fact that a computer is only capable of calculating problems that have finite expansion, certain boundary conditions must be specified before simulating. To simulate infinite space around the antenna structure, we can set the boundary conditions to the option 'Open (Add Space)'. The software then adds a bounding box around the model where each face operates like free space (waves can pass this boundary with minimal reflections). This box is positioned to allow some extra space around the antenna structure for far-field calculation.

3.3 Optimization: Simulated Parameter Sweeps

This section details the simulation work carried out in designing and optimizing the proposed ceramic block PIFA antenna for use over the 6.3 – 9 GHz UWB band. Parameter sweeps of the critical dimensions of the design are presented and their effects on the performance of the antenna are outlined and discussed. An external matching circuit is used to fine-tune the design. A detailed description of the structure and dimensions are presented as well as analysis of the S11 and efficiency of the final design.

3.3.1 Parameterized Model

To begin with, a parameterised simulation model of a microstrip patch antenna was built up in CST Microwave Studio. A parameterised model allows easy adjustment of antenna dimensions and thus efficient optimisation of an antenna structure. The values of all dimensions of the structure were swept using the parameter sweep function in the CST simulator. The results of each sweep were then studied to observe the effect of adjusting the value of each particular

parameter, and to identify an antenna structure which provided optimum performance across the required frequency bands.

As described in [19] the resonant frequency of a microstrip patch or PIFA antenna can be approximately determined by:

$$f_{RES} = \frac{c}{4(W+L)\left(\sqrt{\varepsilon_r}\right)} \qquad (23)$$

where W and L are width and length of the radiating patch respectively, ε_r is the dielectric constant of the ceramic substrate and c is the velocity of light.

The patch antenna consists of a radiating 'patch' element suspended over a ground plane. The patch is printed on the top horizontal surface of a ceramic block. It is parallel to the ground plane and separated from it by the ceramic block. The antenna also has a vertical feeding element which connects the feed line on the mobile handset test board to the radiating patch (see fig. 3.4a).

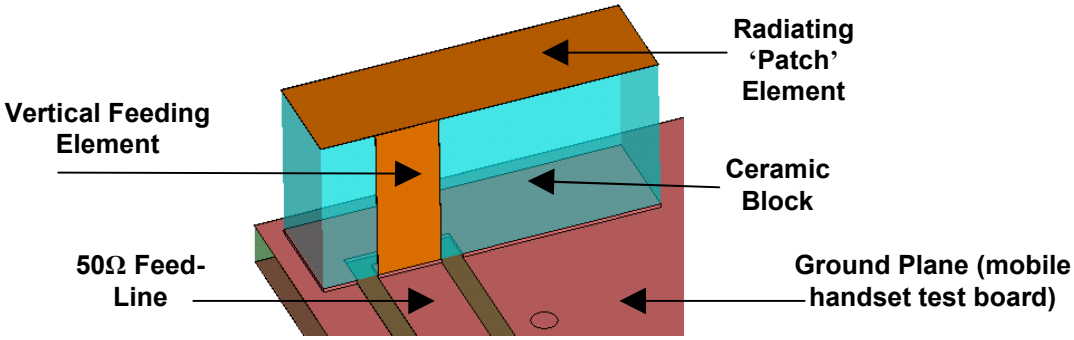

Fig. 3.4 (a): CST Simulation model of microstrip patch antenna printed on ceramic block

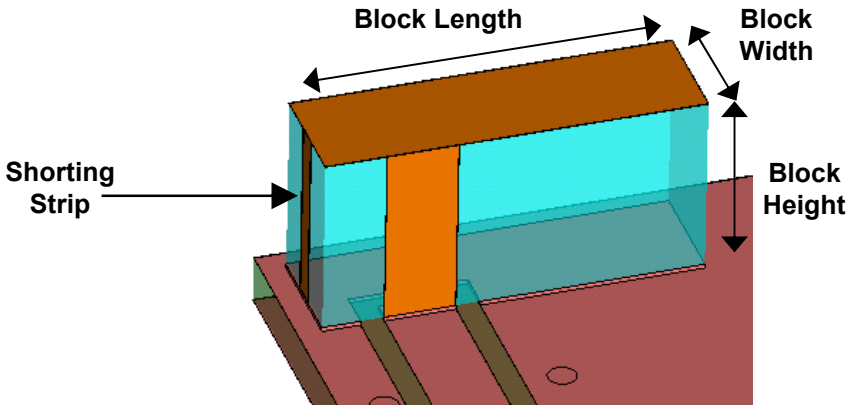

Fig. 3.4 (b): CST Simulation model of PIFA antenna printed on ceramic block

After some initial sweeps were carried out to verify the approximate antenna size required to achieve the necessary resonant frequency, the shorting strip was added to the end of the block nearest the feed, to create a PIFA structure as in fig. 3.4b. The critical factor in PIFA design is the positioning of the feed and grounding points relative to each other to achieve the best match to 50Ω at the input. Adding a grounding pin to the antenna and adjusting the feed position to the point which gives the best 50Ω match allows us to optimise the input match and thus the overall performance of the antenna.

Parameter sweeps of all critical dimensions of the antenna structure including block length, block height, block width, ceramic dielectric constant, feed width & position and shorting strip width & position were then carried out. As well as providing more detailed and accurate information regarding the dimensions of the antenna structure necessary to achieve the desired performance, simulated sweeps can provide invaluable information regarding the operation of the antenna. To illustrate this point, some key parameter sweeps of the antenna structure are presented along with observations and conclusions derived from the resulting data.

Two key results are observed for each of the sweeps - the real value of the input impedance of the antenna and the return loss or S11. The real value of the input impedance is presented to illustrate the true resonances of the antenna structure (i.e. the frequencies at which the antenna structure is resonating). These 'true resonances' are the resonances which were investigated, controlled and manipulated during the design process, by optimising various antenna parameters,

to achieve the final desired antenna performance. They appear as peaks on the real input impedance characteristic and have an imaginary impdedance of zero. Observing these resonances and how they can be shifted in value and frequency, gives us an important insight into the design mechanism of the antenna and how its performance was optimised. However, observing the resistive input alone does not give us the full picture when investigating the overall performance of the antenna.

The S11 or return loss, which is the ratio of the voltage reflected at the antenna input to the voltage fed into the antenna, gives a much clearer indication of the antenna's overall performance. A desirable S11 relies on having an input impedance which matches 50Ω as closely as possible across the band of interest (in this case the 6.3 – 9GHz UWB Bandwidth). This is due to the fact that the antenna will ultimately be integrated into a UWB system with an output impedance of 50Ω. Thus the S11 relies on a combination of the true resonances of the antenna structure and the best match to 50Ω. It is important to note therefore, that a peak value on the real value of the input impedance response does not necessarily translate into an optimum S11 response.

3.3.2 Sweep 1: Dielectric Constant ε_r of Ceramic Block

Dielectric loading of an antenna concentrates the electric fields surrounding the antenna into the area occupied by the dielectric material. It has two main effects on antenna performance, which are (i) pulling down in frequency or 'loading' the fundamental resonances of the antenna, by increasing the effective current path length and (ii) increasing the *Q* of the antenna and thus reducing the overall bandwidth performance. The degree of loading depends on the location of the dielectric material, the type of antenna and the value of the dielectric constant of the material.

To illustrate the effect of the dielectric loading caused by the ceramic block around which the antenna is built, a number of parameter sweeps were carried out. Figures 3.5a and 3.5b show plots of the real value of the input impedance (Ω) and S11 (dB) of the antenna respectively vs. Frequency (GHz) as the dielectric

constant ε_r of the ceramic block is swept from 1 to 12. All other dimensions remain constant. The considerable effect that the dielectric loading has on the performance of the antenna is immediately clear.

The red plot represents the antenna performance when ε_r =1. This is equivalent to having a block of air between the radiating element and the ground plane. A single resonance at 7.9GHz is clear from the impedance plot. As the value of the ε_r is increased, this resonance is loaded and reduced in frequency to 7.5GHz, 7GHz and 6.5GHz for ε_r =4, 8, & 12 respectively. A second effect of the presence of the ceramic block is that a dielectric resonant mode is excited within the block itself, which resonates at a slightly higher frequency than the PIFA resonance. The single resonance which exists when ε_r =1 is replaced by two resonances when ε_r =4, the second resonance appearing at around 8.8GHz. The frequency of this dielectric resonance is also reduced as the ε_r is further increased.

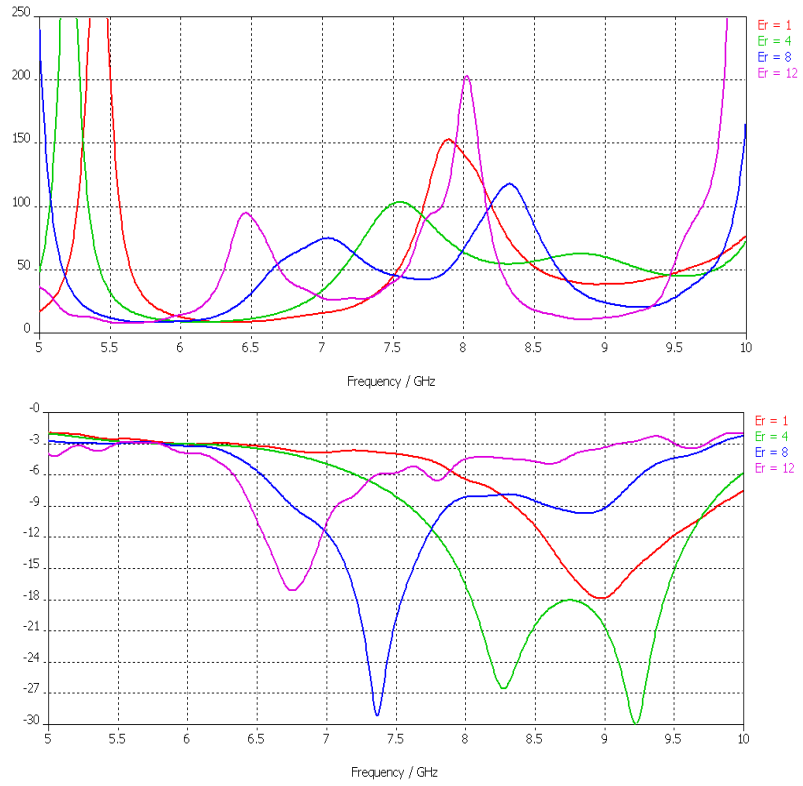

Fig. 3.5a: Real Value of Input Impedance (Ω) vs. Frequency (GHz) as dielectric constant of ceramic material is swept; 3.5b: S11 (dB) vs. Frequency (GHz) as dielectric constant of ceramic material is swept

In theory we can combine the response of this second resonance with the response of the lower PIFA resonance to achieve the broad bandwidth required for UWB. When ε_r =8, for example, the -6dB bandwidth on the S11 plot is 6.5GHz – 9.75GHz. After further sweeps an ε_r =7.5 was chosen due to its effective performance and the ready availability of ceramic material with ε_r =7.5 for measurement prototype manufacture.

3.3.3 Sweep 2: Ceramic Block Length

The graphs in fig. 3.6a and 3.6b show plots of the real value of the input impedance (Ω) and the S11 (dB) of the antenna respectively vs. Frequency (GHz), as the length of the ceramic block (and thus the radiating element) is swept between 5mm and 6.5mm in 0.5mm increments. All other dimensions of the antenna remain constant during this sweep.

As can be seen from the impedance plot, both resonances are shifted down in frequency as the block length is increased. This is as we would expect, since increasing the length of the radiating element will increase the length of the current path in the PIFA and reduce the lower resonance, while increasing the length of the ceramic block will increase the dielectric resonant length and decrease the frequency of the upper resonance. For example, when the block length = 5mm (red plot) the resonances are evident at 7.4GHz and 9.2GHz on the impedance plot. These are shifted down to 6.65GHz and 8.2GHz when the block length = 6.5mm (purple plot).

It is also interesting to note the effect on the real values of the input impedance. As the block length is increased, the real value of the input impedance is reduced at the lower resonance whereas it is increased at the upper resonance. For example, for block length = 5mm, peak real impedance at the resonances is 165 Ω and 65 Ω at the lower and upper resonances respectively. This has become distinctly inverted at block length = 6.5mm with corresponding real impedances of 65 Ω and 165 Ω respectively. To achieve the optimum bandwidth possible it will be necessary to find the best balance between the two resonances to achieve the maximum bandwidth possible. The effect of the sweep on the overall performance

of the antenna is illustrated in the S11 plot. A block length of around 6 allows for good combination of the resonances and exhibits a very broad bandwidth.

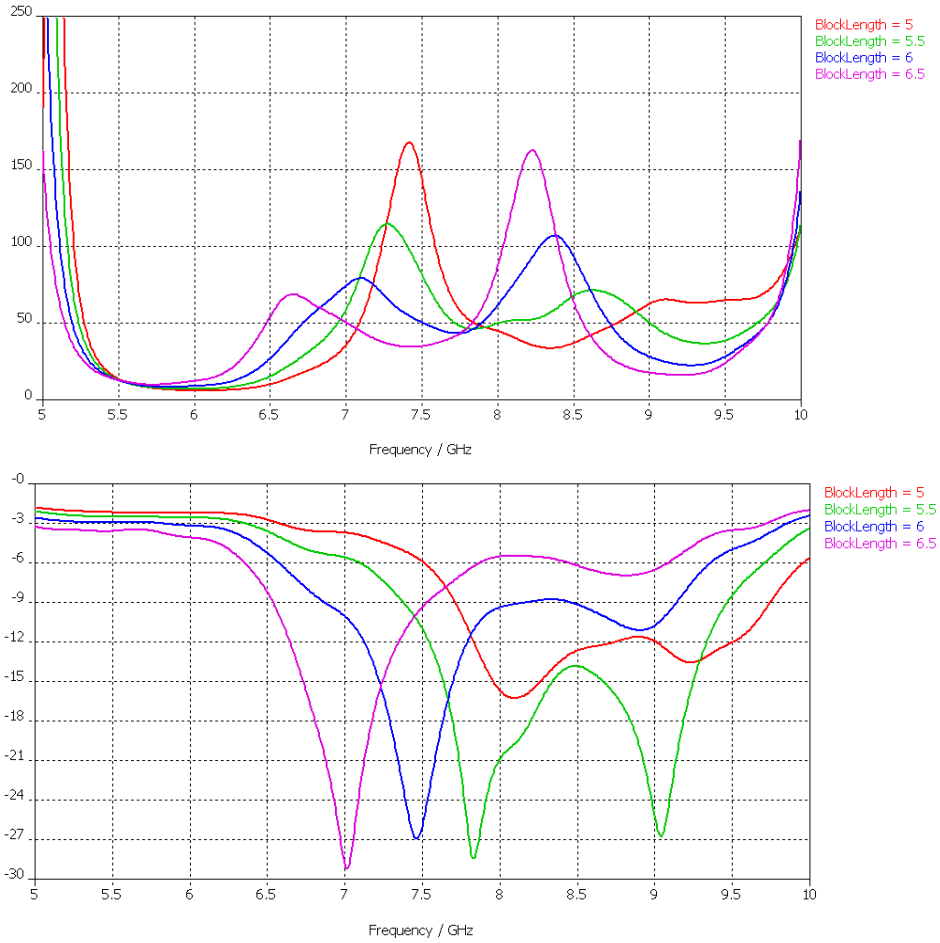

Fig. 3.6a Real Part of Input Impedance (Ω) vs. Frequency (GHz) as block length is swept,; 3.6b: S11 (dB) vs. Frequency (GHz) as block length is swept

3.3.4 Sweep 3: Ceramic Block Width

A parameter sweep of the width of the ceramic block as in fig. 3.4b also provides some useful results. The block width is swept from 2mm to 3.2mm in 0.4mm increments, with all other dimensions constant. As can be seen from the real value of the input impedance plot (Ω) vs. Frequency (GHz) in fig. 3.7a, varying the

block width has a notably different effect on each of the two resonances. Increasing the block width reduces the lower resonance in frequency. This again is as expected, since increasing the block width also increases the width of the radiating element and thus increases the path length of the quarter-wave resonance of the PIFA. Since the path length is not increased as much as when the block length was increased, the reduction in frequency is relatively small. For example with a block width of 2mm, the quarter wave resonance is at around 7.2GHz. This is reduced to around 6.7GHz when the block length is increased to 3.2mm.

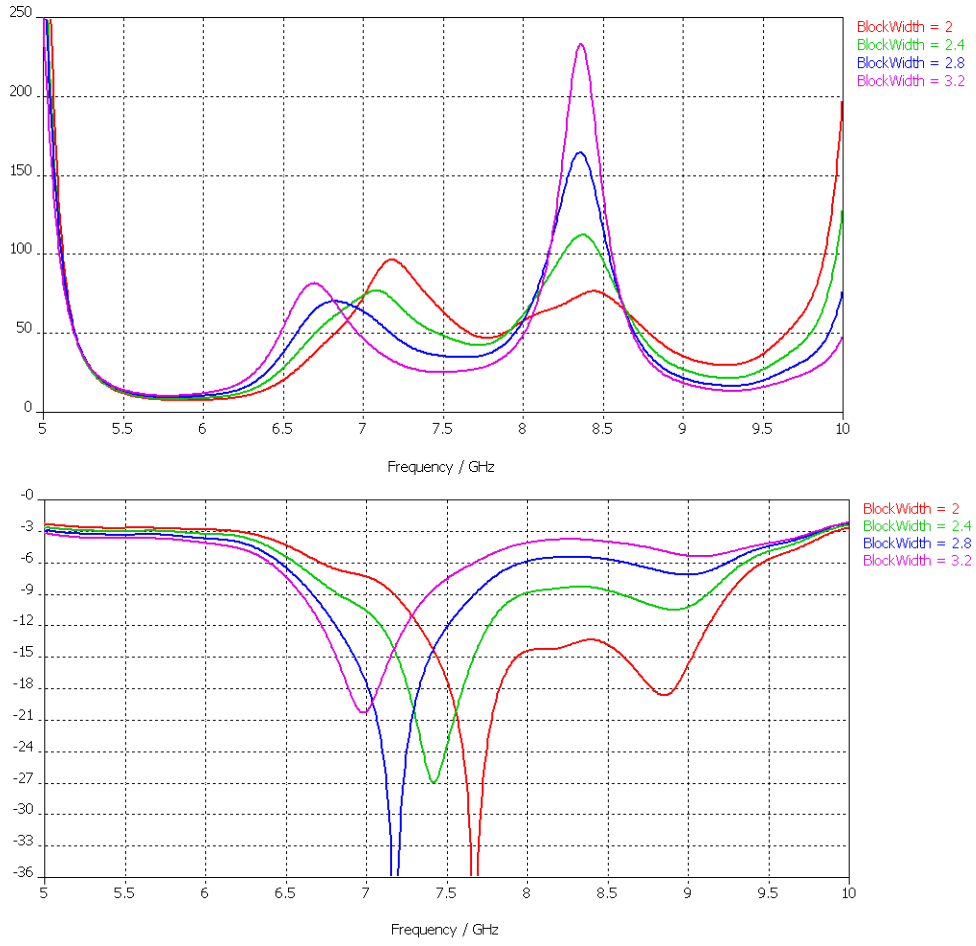

Fig. 3.7a: Real Part of Input Impedance (Ω) vs. Frequency (GHz) as block width is swept; 3.7b: S11 (dB) vs. Frequency (GHz) as block width is swept

The upper resonance, due to the resonance of the dielectric block itself is also affected by the variation of the block width, but in this case the resonant frequency remains effectively constant. The impedance on the other hand increases noticeably as the block width is increased. The closer the input impedance is to 50Ω at any frequency within the band of interest, the better the match at the input will be at this frequency. Thus the less energy will be lost due to input mismatch. Since the total efficiency of the antenna includes mismatch losses at the input, optimizing the match is critical in maximising the total efficiency of the antenna. The increase in the value of the input impedance evident in fig. 3.7a has a considerable effect on the match at the higher end of the bandwidth. As the block width becomes too large, performance at the higher end is degraded quite substantially as can be clearly seen in the S11 plots of fig. 3.7b. A block width of around 2.4mm shows a good balance between the two resonances allowing for good performance across most of the 6.3 – 9GHz band.

3.3.5 Sweep 4: Ceramic Block Height

A parameter sweep of the height of the ceramic block as in fig. 3.4b is also presented. The height of the block was swept from 3mm to 4.5mm in 0.5mm increments and the resulting plots are shown in figures 3.8a and 3.8b. The effect of varying the block height has the opposite effect on the resonances as varying the block width did. The lower resonance, due to the PIFA itself, remains constant in frequency, but the input impedance and thus the match is affected at this frequency. The upper frequency due to the dielectric block is reduced in frequency as the block height is increased.

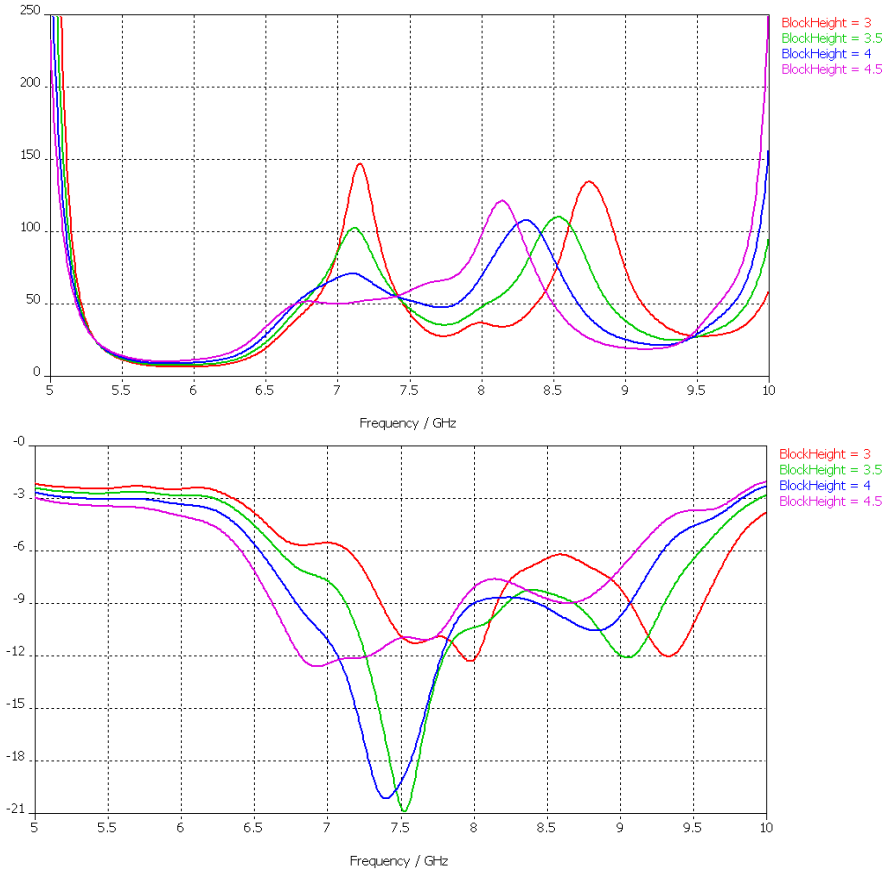

Fig. 3.8a: Real Part of Input Impedance (Ω) vs. Frequency (GHz) as block height is swept; 3.8b: S11 (dB) vs. Frequency (GHz) as block height is swept

3.3.6 Sweep 5: Feed Point Sweep

As discussed before, the positioning of the feed and grounding points to allow the best match possible over the required bandwidth is critical to PIFA antenna design. Keeping the position of the shorting strip stationary at one end of the PIFA and adjusting the feed position to the point which gives the best 50Ω match allows us to optimise the input match and thus the overall performance of the antenna. The importance of the relative positions of feed and grounding points for a PIFA antenna can be illustrated by examining a parameter sweep of the position of the feed point while keeping the position of the shorting strip fixed.

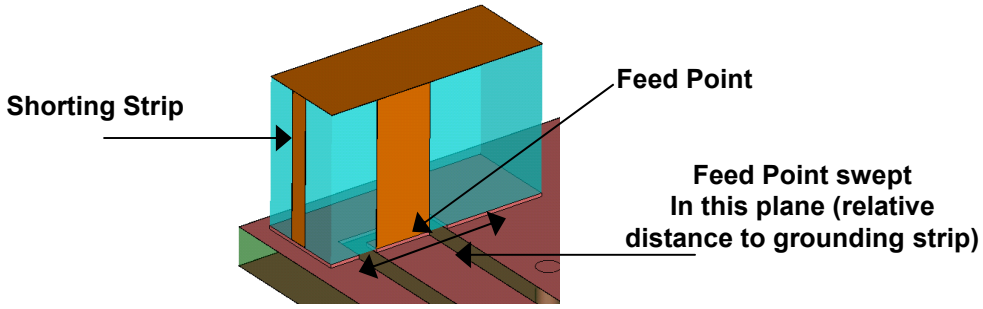

Fig. 3.9: PIFA antenna with grounding strip positioned half way along back face of ceramic block

In the plots of fig. 3.10 below, the feed position is swept from 1.5mm (this is relative to the edge of the mobile handset test board – *i.e.* 1.5mm from the edge of the board to the centre of the feeding strip) to 3mm from the edge in 0.5mm increments, in the plane illustrated in fig. 3.9. As the feed point approaches the open-circuit end of the antenna, the current path and thus the overall resonant length decreases and the lower resonance due to the main PIFA operation is shifted up as expected. When the feed position is at 1.5mm for example, the fundamental resonance is at 6.5GHz (red plot). When the feed is moved to 3mm, the fundamental resonance is shifted up to approximately 7.5GHz (pink plot). The upper dielectric block resonance is also shifted up in frequency, as the block becomes excited further from its edge. When the feed is at 1.5mm the dielectric block resonates at 8GHz, which shifts up to around 8.9GHz when the feed position is moved to 3mm from the edge of the board.

The increase in the value of the input impedance of the lower resonance as the feed point is moved closer to the open-circuit end is also very clear. As we discussed before, as the feed is moved closer to the open circuit end of the antenna the E-field increases and the current decreases, increasing the real value of the impedance. A feed position of around 2mm (green plot) gives a resonance very close to 50Ω and thus a corresponding S11 which provides a good -6dB bandwidth. The real value of the impedance for the upper dielectric resonance on the other hand, is reduced as the feed position is shifted up. Again a balance between the two is needed to provide the best overall bandwidth.

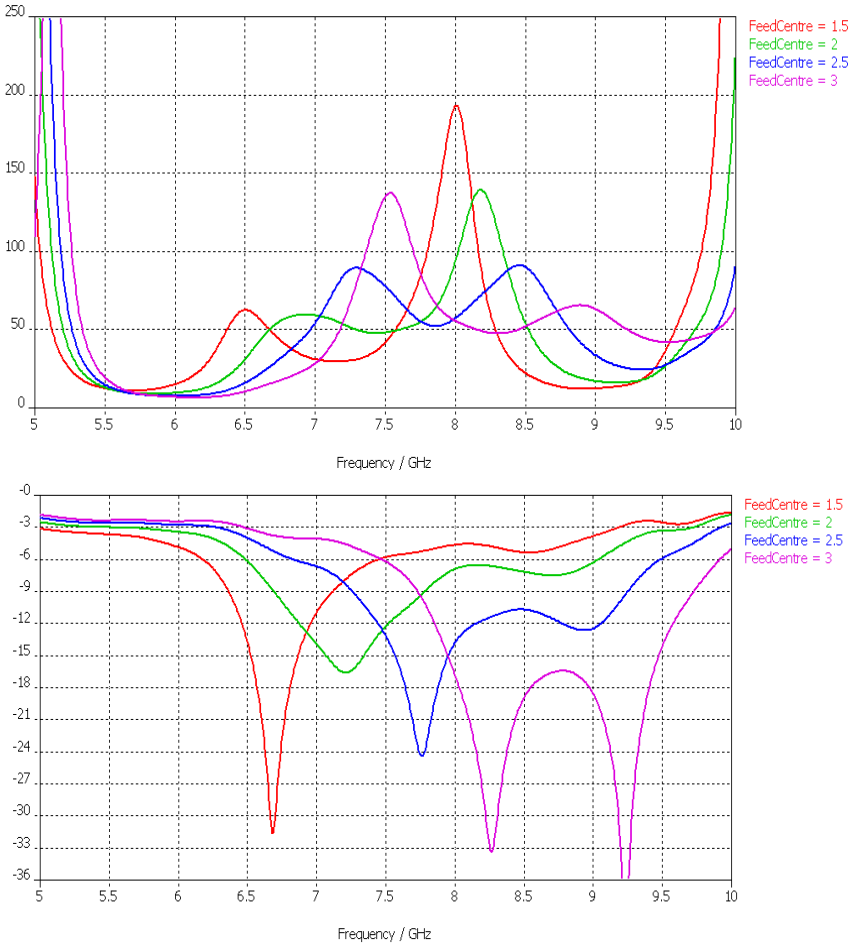

Fig. 3.10a: Real part of input impedance (Ω) vs. frequency (GHz) as location of feed point is swept;; 3.10b: S11 (dB) vs. frequency (GHz) as location of feed point is swept

3.3.7 Sweep 6: PIFA Fold-Over

The final parameter sweep worth looking at involves an additional 'fold-over' section which was added to the antenna structure as in fig. 3.11. This section is printed on the same face as the feeding strip and adds some extra area to the radiating element. It has the effect of improving the bandwidth of the two separate resonances allowing them to combine more effectively to achieve a better overall in-band response.

Fig. 3.12 shows plots of the real value of the input impedance and S11 (dB) respectively vs. frequency (GHz) as the extent to which this new fold-over section folds over is swept from 0mm to 1.275mm in 0.425mm increments. As the fold is

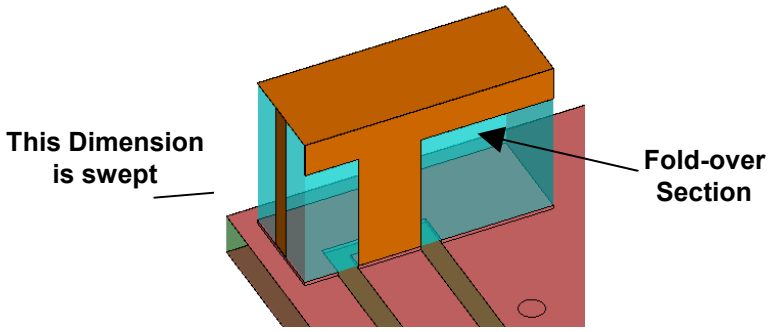

Fig. 3.11: CST Model of Final High-Band UWB Design including fold-over section

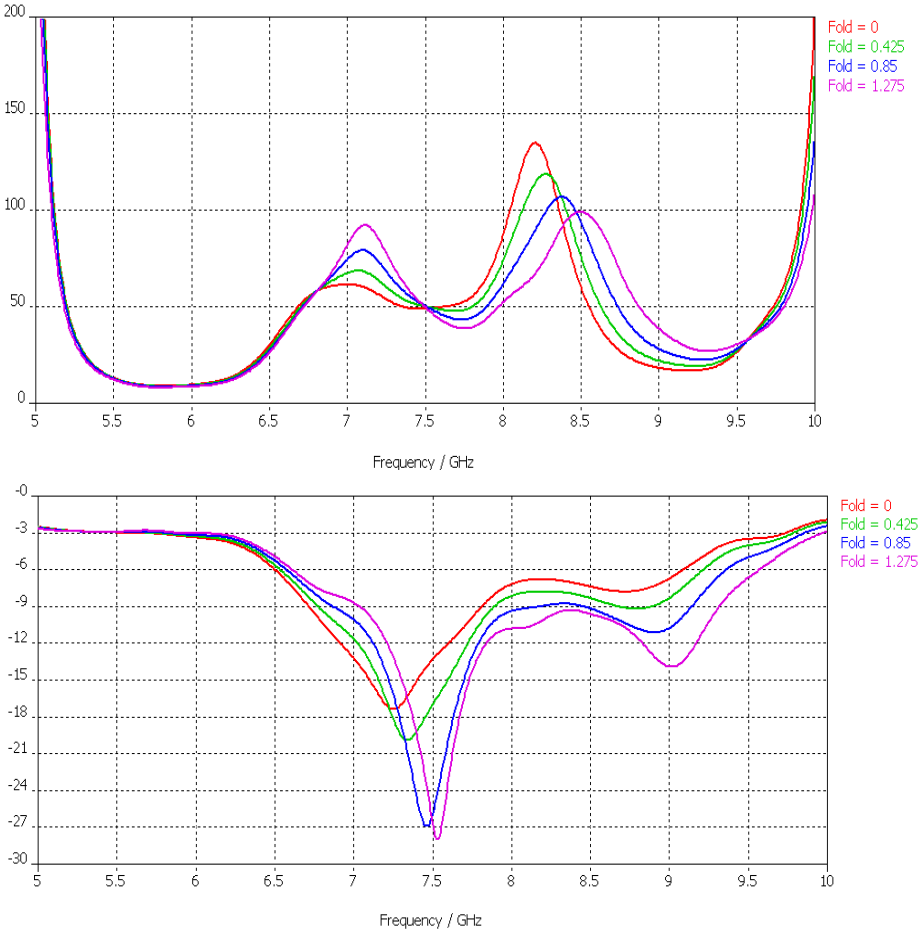

Fig. 3.12a: Real Part of Input Impedance (Ω) vs. Frequency (GHz) as extent of fold-over portion is swept; 3.12b: S11 (dB) vs. Frequency (GHz) as extent of fold-over portion is swept

increased, the real value of the input impedance at the lower resonance increases, while the value at the upper resonance decreases. Thus we can use the 'fold-over' section to fine-tune the balance between the responses of the two resonances and thus optimise the match across the entire 6.3 – 9 GHz band. A 'fold-over' value of 1mm was chosen for the final design as it provided the best balance of performance at lower and higher ends of the band.

It is worth noting that the addition of the fold-over section has the disadvantage of pushing the lower resonance up in frequency and thus degrading the performance slightly at the low end of the band. This can be negated by increasing the overall size of the block or increasing further the dielectric constant of the ceramic block material, but both of these solutions come at a price; an unwanted increase in antenna size or a decrease in mechanical strength respectively. A technique of external matching was therefore researched to resolve this issue. This involved adding surface mountable chip matching components at the input to the antenna to improve performance at the lower end of the band. Solving the problem in this way will illustrate how external matching can be used not just for narrow-band fine-tuning of an antenna, but also to improve a wideband UWB response within a mobile handset environment.

3.3.8 Final PIFA Design

After extensive parameter sweeps were carried out and the data cross-correlated, an optimum design for the UWB PIFA antenna was chosen. The antenna block has overall dimensions of 6mm x 4mm x 2.4mm (57.6mm^3) and dimensions of the metallic patterns on each face are given in fig. 3.13. All dimensions are in millimetres.

The simulated total efficiency (which includes radiation efficiency and input mismatch) can be seen in fig. 3.14a and the corresponding S11 response can be seen in fig. 3.14b. The antenna has a total efficiency of greater than 40% across the entire 6.3 – 9 GHz band and a total efficiency of greater than the desired 50% from 6.75 – 9 GHz. Similarly, the S11 response meets the required UWB specifications from 6.58 – 9.36 GHz. As mentioned before, a method of external

matching to improve this lower edge performance will be reported in the next section.

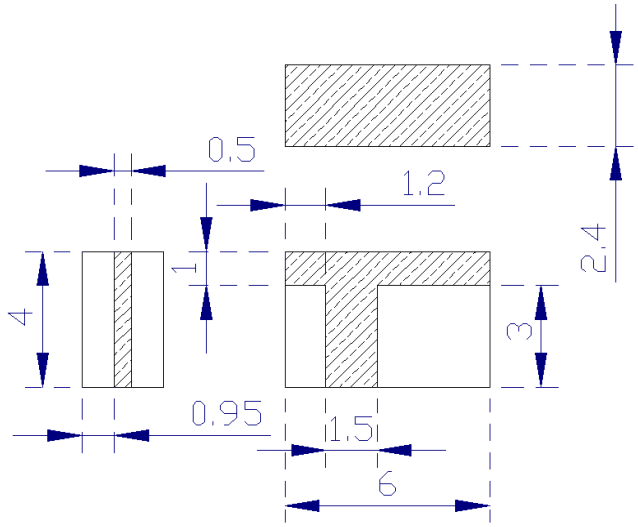

Fig. 3.13: Dimensions of the Final high-band UWB PIFA design (all dimensions in mm)

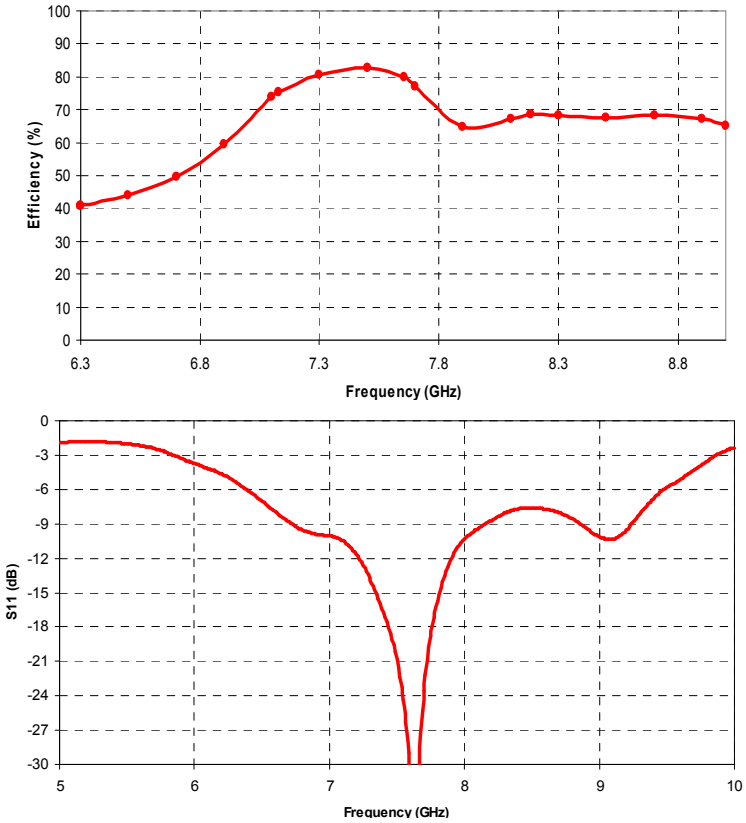

Fig. 3.14 (a): Simulated in-band Efficiency vs. Frequency (GHz) plot for final High-Band UWB Design; (b): Simulated S11 (dB) vs. Frequency (GHz) plot for final High-Band UWB Design

3.3.9 External Matching using chip components

The simulated antenna achieves the desired performance over the majority of the 6.3 – 9 GHz bandwidth. However its performance at the lower end of the band, around 6.3 – 6.5 GHz, does not meet the required UWB efficiency and S11 specifications. To demonstrate how improving the input match can enhance the overall performance, a technique of external matching was used to tune the response at the lower end of the band.

External matching can be realised using printed stubs on the mobile handset wiring board itself or by using a circuit consisting of surface mountable ceramic chip inductors and capacitors. Ceramic chip components tend to have a specified upper frequency limit of 3-4GHz, so close attention must be paid to the response in the higher UWB bands, to ensure the components are behaving as expected.

External matching components can be very useful in antenna design, especially when the antenna is placed in an environment which has other objects in close proximity. In a mobile handset for example, other components such as the battery, screen, chip components and other antennas can de-tune the performance of the antenna (the frequency of operation is often shifted up or down). When this is the case, a simple LC matching circuit can be used to re-tune or re-optimize the antenna. This negates the effect of these external factors and allows the antenna to achieve its original free-space performance.

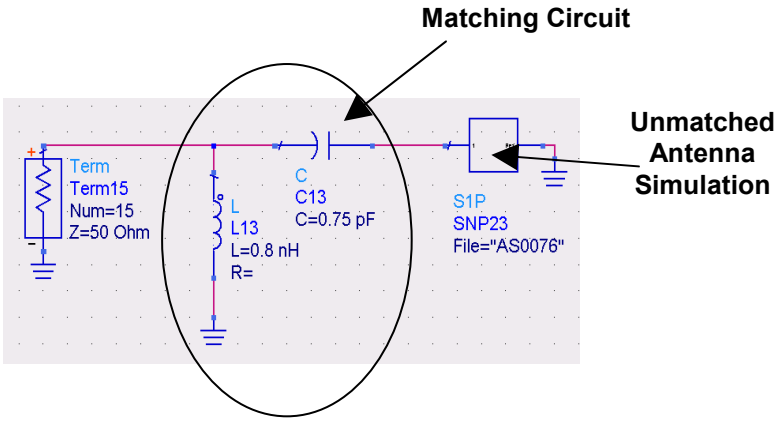

Fig. 3.15: ADS Simulation of external matching circuit

In the case of the UWB PIFA antenna we will illustrate how external matching can be used to tweak the antenna response and improve performance at the lower end of the 6.3 – 9 GHz bandwidth (at around 6 – 7 GHz). The S11 data from the CST simulation was exported into the Agilent ADS (Advanced Design System) circuit design package. An external matching circuit was simulated and optimized using ideal capacitor and inductor components. The final optimized ideal circuit model is illustrated in fig. 3.15. The matching circuit consists of a series capacitor of value 0.75pF and a shunt inductor of value 0.8nH. Smith chart data illustrating the improved match from 6 - 7 GHz is shown in fig. 3.16 and the effect of this matching circuit on the efficiency and S11 performance of the antenna can be seen in fig. 3.17. The S11 of the antenna has been improved at the lower end of the band and the antenna now exhibits a total efficiency of greater than 50% across the entire 6.3 - 9 GHz bandwidth.

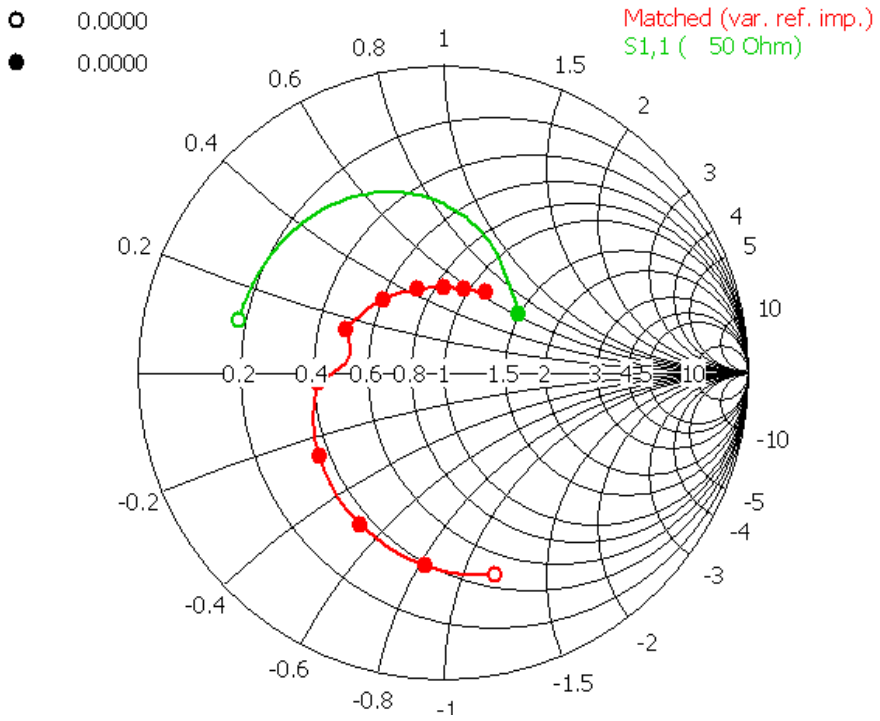

Fig. 3.16: Input Impedance of Antenna without matching (green) and with matching (red) from 6 to 7 GHz.

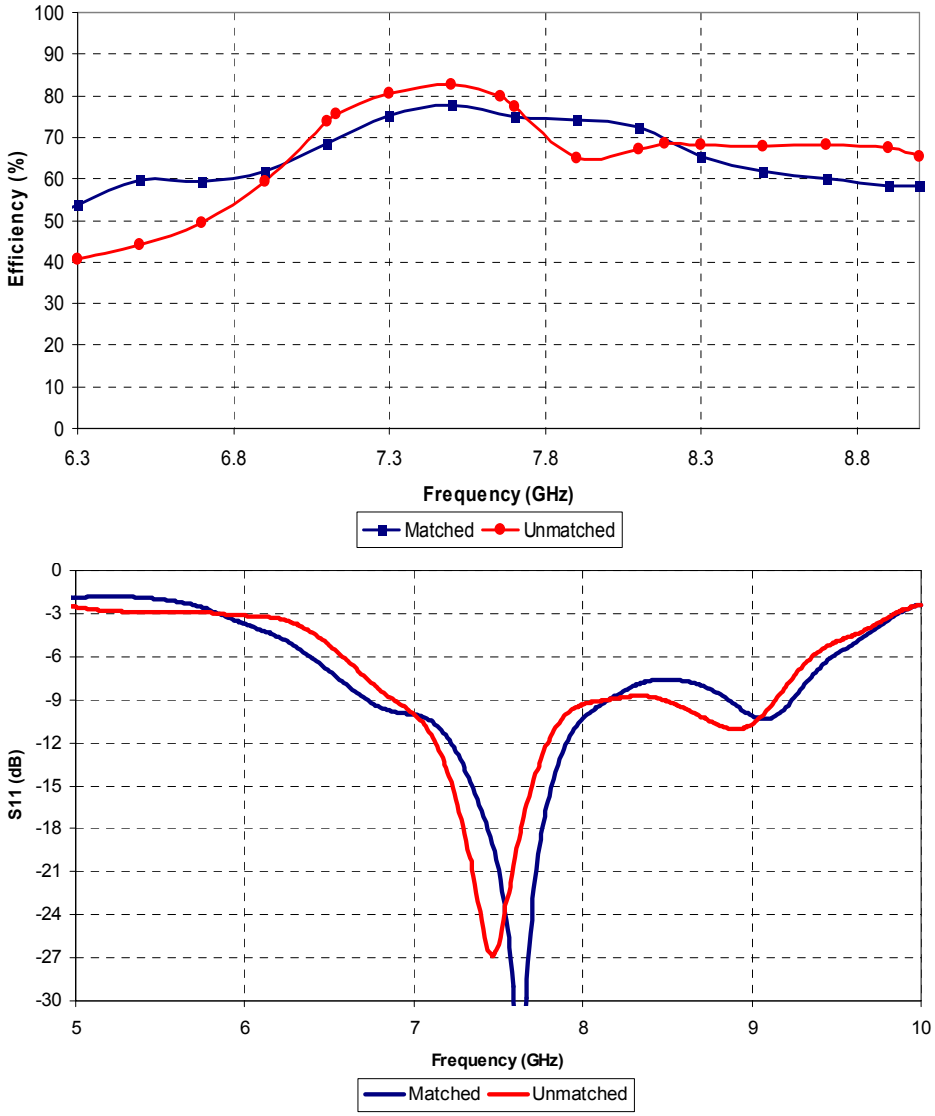

Fig. 3.17 (a): Simulated Matched and Unmatched Efficiency (%) vs. Frequency (GHz) for UWB PIFA; (b): Simulated Matched and Unmatched S11 (dB) vs. Frequency (GHz) for UWB PIFA

3.3.10 Simulation Summary

A ceramic PIFA antenna for use in a mobile handset has been researched, developed and optimised. The antenna enables UWB functionality in the 6.3 – 9 GHz bands. A detailed investigation into the effects of varying the critical parameters of the structure has been carried out using extensive simulated

parameter sweeps. An optimum design has been chosen, which performs well over the entire 6.3 – 9GHz band and which maintains a small physical size of 6mm x 4mm x 2.4mm, ideal for integration into a mobile handset. A method of external matching has also been presented to allow fine tuning of the antenna.

3.4 Field & Current Analysis at Resonant Frequencies

To gain some more insight into the operation of the proposed UWB PIFA antenna, some key antenna characteristics are observed at the resonant frequencies. The electric field surrounding the antenna, the surface current on the structure itself and the far-field radiation pattern and gain of the antenna are examined to provide a more comprehensive understanding of the operation of the antenna.

3.4.1 Input Impedance

The corresponding real value of the input impedance of the antenna (Ω) described in the previous chapter vs. Frequency (GHz) is plotted in fig. 3.18. As can be seen from the plot, the main PIFA resonance is located at around 7.1GHz and the DRA resonance at 8.4GHz. To gain some more insight into the operation of the antenna we will use CST to explore in more detail the E-fields, currents and far-field radiation patterns at the main PIFA resonance at 7.1GHz

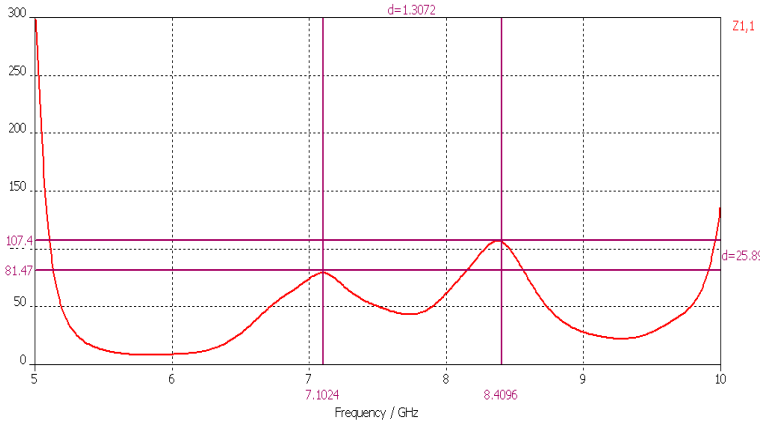

Fig. 3.18: Simulated real part of Impedance (ohms) of the final antenna design showing main resonances

3.4.2 Antenna Electric Field

As a starting point it is worth observing the electric field or 'E-field' of the antenna at the resonant frequencies since the E-field gives an indication of the potential difference (voltage) between two points. When the antenna is supplied with RF energy an electric field is created around it which is continually oscillating. A magnetic field is also created and both mutually perpendicular oscillating fields travel together in phase [18]. The E-field intensity falls off in direct proportion to distance travelled and is measured in volts per metre.

Fig. 3.19 shows a 3-D plot of the E-field around the UWB PIFA antenna structure at the first resonance (7.1 GHz). Since the E-field is continually oscillating, the plot is taken at a phase of 180º. The scale of the E-field intensity is in volts per metre and both the size and colour of the arrows are representative of the strength of the field at a particular point in space. As can be seen from the plot, the E-field is strongest at the open-circuit end of the structure and weakest at the feed point of the antenna. This suggests high voltage at the open-circuit end and low voltage at the input. Since the positions of this minimum and maximum do not change as the field oscillates, it suggests a standing wave, which is a quarter of a wavelength long. This is the fundamental quarter-wave resonance of the PIFA antenna. It is also interesting to note how the E-field is skewed towards the ground plane.

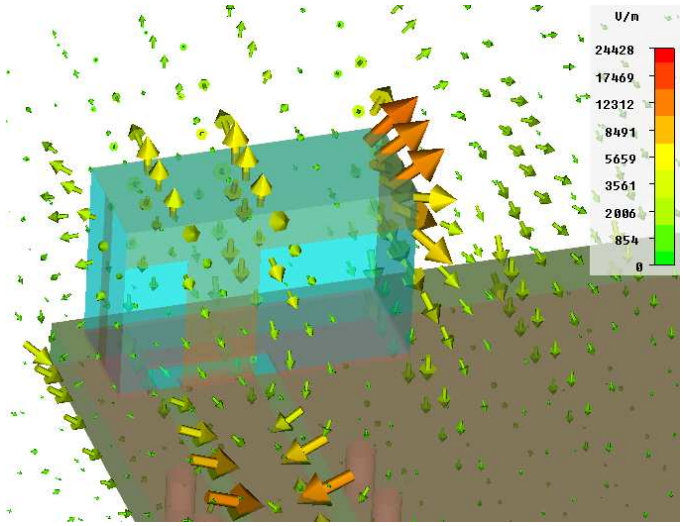

Fig. 3.19: CST Simulation of E-field of PIFA antenna at 7.1GHz

3.4.3 Surface Current

The performance of an antenna is based on fundamental frequencies at which the structure resonates and radiates optimum power. These fundamental frequencies are related to resonant lengths within the antenna structure itself. These resonant lengths are caused by current paths within the structure and the resonant frequencies are directly proportional to the length (or some fraction) of these paths. The most basic antenna is a quarter-wave monopole, where the length of the monopole is equal to a quarter of the wavelength of operation of the antenna. Fig. 3.20 below shows a quarter-wave monopole, a half-wave dipole, a full-wave dipole and their corresponding voltage and current distributions along the respective structures. At its resonant frequency, a quarter-wave antenna is characterised by high voltage and low current at the open-circuit end and the opposite at its input. At resonance, a half-wave antenna will have low current at both ends and high current in the centre of the structure, with the voltage having the opposite distribution.

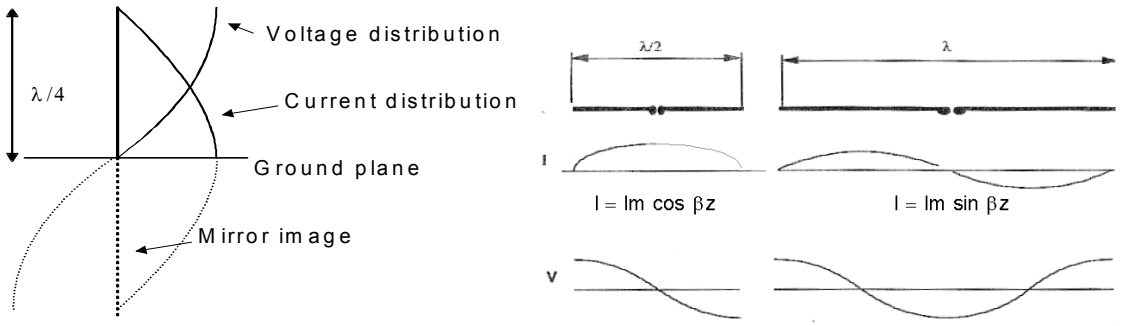

Fig. 3.20: Voltage and Current standing waves for (a) Quarter Wave Monopole, (b) Half Wave Dipole and (c) Full Wavelength Dipole Antennas

CST Microwave studio also allows us to look at the surface current of the antenna along any conducting surface at certain frequencies. Fig. 3.21 shows the absolute value of the surface current of the antenna at the resonant frequency of 7.1GHz. Surface current is measured in Amps/Metre and the colour is related to the strength of the surface current at any particular point. As can be seen from the plots, there is a clear quarter-wave resonance at 7.1GHz, with the peak current at the input to the antenna and minimum current at the open-circuit end.

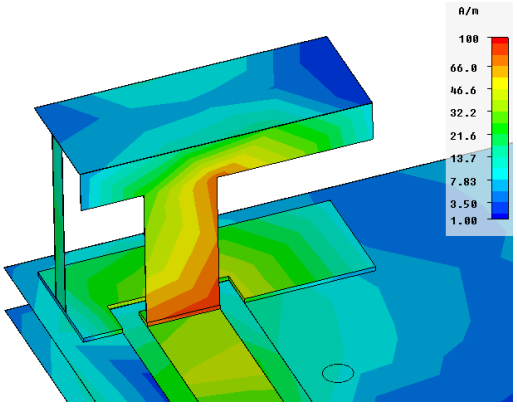

Fig. 3.21: CST Simulation of surface current of PIFA antenna at 7.1GHz

3.4.4 Far-Field Radiation Pattern

As mentioned before, the radiation pattern of an antenna is a 3D graphical representation of the angular distribution of energy transmitted or received by an antenna. It allows us to see the direction of peak gain of the Antenna as well as any side-lobes or back-lobes in the Antenna's characteristic. It also gives an indication of how omni-directional or directive the Antenna is overall.

Fig. 3.22 shows a CST 3D plot of the radiation pattern of the simulated UWB antenna at 7.1GHz. The shape and colour of the pattern represent the strength of the fields of the antenna in a particular direction, measured in dBi or decibels with respect to an isotropic radiator (*i.e.* the ratio of the gain of the antenna in a particular direction to the gain of an ideal isotropic antenna, which uniformly distributes energy in all directions.). As can be seen from the plots, the direction of maximum gain is in the direction of the open-circuit end of the PIFA structure (max gain is 3.18dBi – important due to EIRP restrictions), but the pattern in general is fairly omni-directional, with the exception of a few minor nulls. As we mentioned before, a UWB antenna for use within a handset needs to have good omni-directional performance to allow reliable connectivity even though the location and orientation of the handset may be constantly changing when in use.

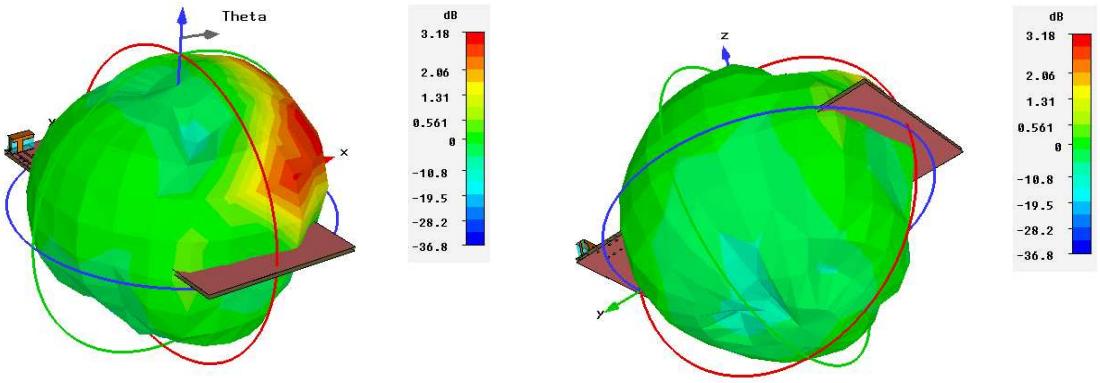

Fig. 3.22: CST Simulation of far-field radiation pattern of PIFA antenna at 7.1GHz

3.5 Summary

An antenna design has been researched for use in a mobile handset environment to enable UWB functionality at band groups 3 & 6 (6.3 – 9 GHz). With a maximum volume limit of 60mm^3, a CST model of a microstrip patch antenna was built up and a grounding strip introduced to create a PIFA structure. Since a very broad bandwidth of operation is required from the PIFA, which typically tends to exhibit a fairly narrow-band response, the model was parameterised to allow all important dimensions to be adjusted and optimised to achieve the best possible performance.

Parameter sweeps were carried out on all major dimensions and their results have been presented and discussed. The most important points to note are that the required broad bandwidth was achieved by utilising the ceramic block not only to dielectrically load the main resonance of the PIFA, but also to behave as a Dielectric Resonator Antenna (DRA) and resonate itself at a nearby frequency. This allowed two resonances to be excited in close proximity which could then be combined, enabling the PIFA to achieve a much broader bandwidth than would be possible with its fundamental resonance alone.

Adjusting the block length allowed control over the frequency position of the two resonances and adjusting the block width allowed control over the value of the input impedance at the resonant frequencies. The position of the feed was also critically important to the design and this was adjusted to provide the optimum input impedance match across the band. A fold-over section was also inserted on one side of the ceramic block and optimised to increase the bandwidth further.

The final simulated high band UWB PIFA design was presented. It has dimensions of 6mm x 4mm x 2.4mm (57.6mm^3). Simulated Efficiency and S11 were also presented, with the antenna reaching the required efficiency of 50% from 6.75 – 9 GHz and the required S11 of -6dB from 6.58 – 9 GHz. To improve the performance at the lower end of band a technique of external matching was implemented. This technique involved using an external LC circuit comprising a chip inductor and capacitor located on the mobile handset test board at the input to the antenna. It allowed the overall antenna performance to be improved at the bottom end of the bandwidth and the UWB efficiency and S11 specifications to be met at all points within the 6.3 – 9 GHz band.

CST was then used to carry out a detailed field and current analysis of the simulated structure at the resonant frequencies. The two resonances of the antenna are located at 7.1GHz and 8.4GHz. Data was presented for the lower resonance at 7.1GHz. The quarter-wave resonance of the PIFA can be clearly seen by studying the oscillating maximum and minimums of the E-field or surface current within the structure itself. The E-field plots also illustrate how the fields surrounding a radiating antenna can be interrupted and skewed by the presence of a nearby ground plane, which tends to draw the fields towards it.

The simulated far-field radiation patterns at the resonant frequencies were also observed and data for the field at 7.1GHz is presented. As can be seen from the plots, the radiation pattern is distinctly omni-directional which is very desirable for mobile handset UWB applications, as the location and orientation of the handset will be constantly changing. The maximum gain is 3.18dBi which is also worth noting as it impacts on the Effective Isotropic Radiated Power (EIRP) of the antenna, which is strictly regulated for all UWB systems.

Chapter 4:
High-Band UWB Antenna Measurement

4.1 Introduction

To verify the simulation results, prototype test samples of the ceramic PIFA antenna were built up and measured. This chapter discusses the manufacture of the prototypes as well as measurement techniques used to measure antenna efficiency, gain and radiation patterns. A comprehensive review of the measured results is presented and correlation between simulated and measured data is observed and discussed.

4.2 Measurement Prototypes

A number of prototype samples were printed using a standard block ceramic screen-printing process. The process prints the required metallic patterns onto the six faces of a block of ceramic material using an aluminium paste. A ceramic material with a dielectric constant of 7.5 was used, similar to the material used in the simulation model. The dimensions of the ceramic block were 6mm x 2.4mm x 4mm (a total volume of 57.6mm^3). Fig. 4.1 shows samples of the measurement prototypes.

Once the prototypes were built up, S11 measurements were taken as follows: A prototype was mounted on a test board, similar in dimensions and layout to the simulated mobile handset style test board (80mm x 40mm FR4 substrate with copper ground planes on both sides connected together by copper vias) and with a similar feed-line structure (see fig. 4.2). An SMA connector was attached to the underside of the board, corresponding to the simulated SMA model which was used for all simulations. The external matching network was also mounted as per simulation. As was mentioned before, the aim was to have the

simulation setup as close as possible to the actual measurement setup, to aid in correlation of the simulated and measured data. S11 data was then measured by connecting the SMA connector to a Hewlett Packard 8719 network analyser.

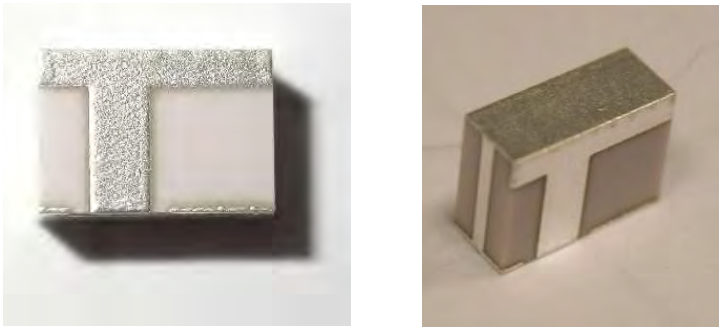

Fig. 4.1: Samples of the UWB PIFA measurement prototype showing the aluminium antenna pattern printed onto a ceramic block substrate

Fig. 4.2: UWB PIFA Antenna mounted on 80mm x 40mm mobile handset test board

4.3 Far-Field and Near-Field Measurement Techniques

Whilst S11 is relatively straightforward to measure as described above, measuring antenna gain, efficiency, directivity and far-field radiation pattern data requires a somewhat more complex setup.

The traditional technique for measuring these parameters is far-field measurement, where the antenna under test is placed in the far-field of some reference antenna. This is normally done in an anechoic far-field chamber, which tends

to require a large amount of clear space as well as a motorized positioning system to allow the antenna to rotate during measurements.

More recently near-field measurement techniques have been developed, which allow measurement of electric fields within the near-field of the antenna. The near-field of an antenna is the area close to the antenna where electric charge and electromagnetic induction effects occur. These effects fade out far more rapidly with increasing distance from the antenna (proportional to the cube of the distance) than the radiated electromagnetic far-field, which fades out proportional to the distance. Near-field effects become negligible more than a few wavelengths away from the antenna. Once the near-field data has been measured, a Fourier transform can be carried out to calculate the equivalent far-field data. Due to the nature of the measurement, near-field chambers tend to take up a lot less space than their far-field counterparts.

For the measurement of the UWB PIFA prototype, a Satimo Starlab 0.6 – 18GHz near-field measurement chamber was used. This chamber uses the near-field measurement technique described above to calculate the equivalent far-field data of the antenna under test. The antenna, mounted on the test board described above, is positioned in the centre of a circular 'arch' which contains 15 separate measurement probes as can be seen in Fig. 4.3. These probes are spaced equally apart along the circular surface. The antenna is rotated horizontally through 360° and the combination of this rotation and the array of probes allows a full 3D scan of the antenna to be carried out, allowing full 3D radiation patterns to be measured, plotted and analysed. Efficiency, gain and directivity information can then be calculated from the far-field radiation pattern data.

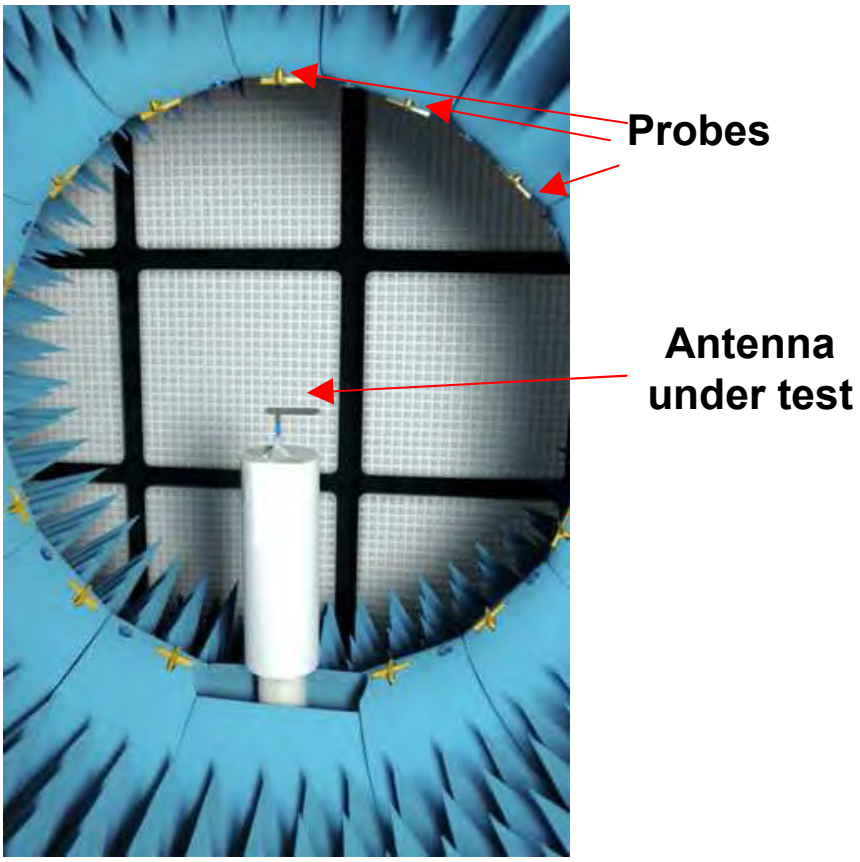

Fig. 4.3: Satimo Starlab near-field measurement chamber with antenna under test

4.4 S11 and Efficiency Measurements

For the UWB PIFA prototype measurements, firstly the matched antenna S11 (dB) was measured and compared with simulation data (see fig. 4.4 (a)). The antenna prototype performed well within band groups 3 and 6, achieving the required -6dB at all points across the 6.3 – 9 GHz band. Measured data also correlated reasonably well with simulated data although the frequencies of the fundamental resonances are shifted slightly. This could be due to a number of reasons, some of which will be discussed in the next section.

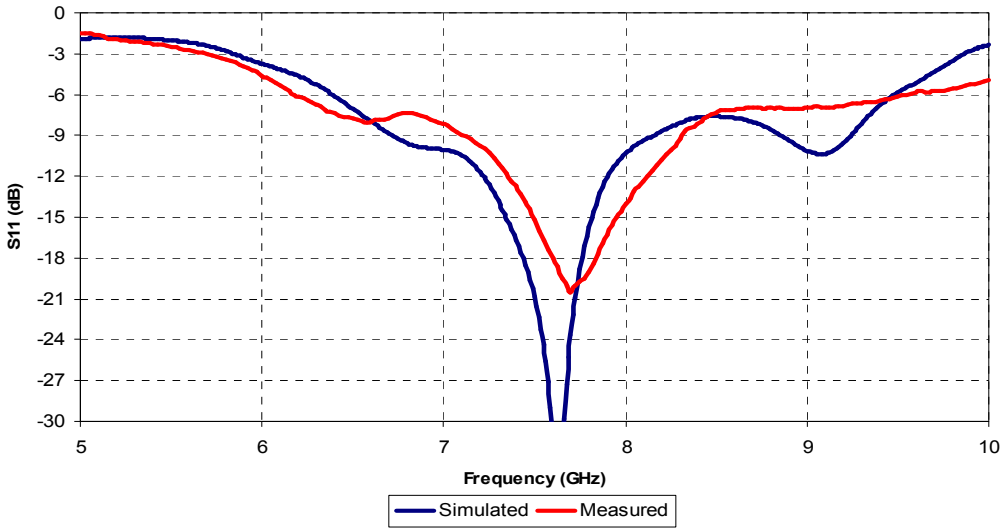

Fig. 4.4: (a) Simulated vs. Measured S11 (dB) for UWB PIFA prototype

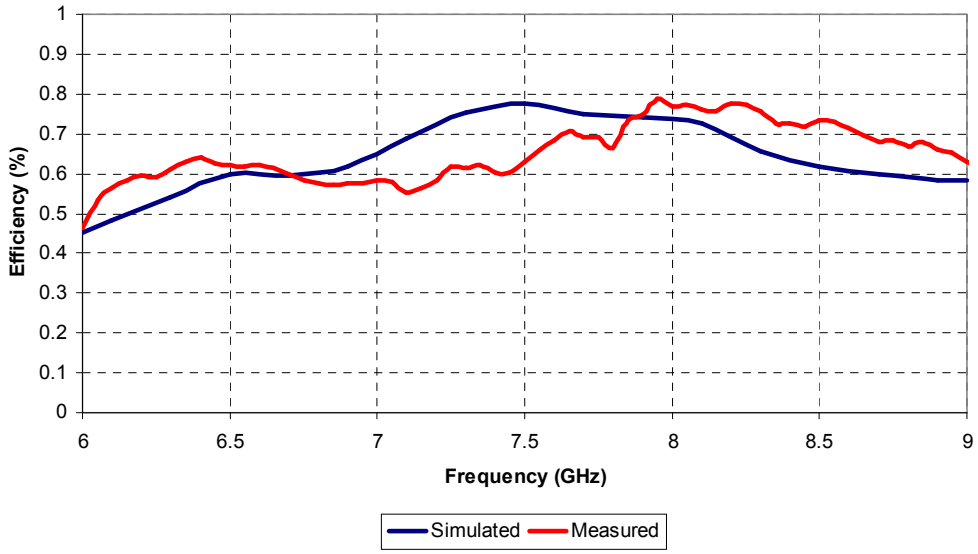

Fig. 4.4 (b) Simulated vs. Measured Efficiency for UWB PIFA prototype

Fig. 4.4b shows a comparison of measured and simulated data for the total antenna efficiency (%) vs. frequency (GHz). Again, correlation between measured and simulated data is reasonably good, while still exhibiting some minor discrepancies. Total efficiency across the band for the measured prototype looks extremely good, with an efficiency of more than 50% (and for the most part more than 60%), across UWB band groups 3 & 6.

4.5 Far-Field Radiation Pattern Measurements

Fig. 4.5 shows a comparison of the measured radiation patterns of the UWB PIFA prototype vs. simulated data at the two resonant frequencies of 7.1GHz and 8.4GHz. The data is presented as 2-dimensional cuts of the 3-dimensional radiation pattern, taken on three orthogonal planes described around simple XYZ coordinates. If we consider the mobile handset board to be in a horizontal position, the XY plane represents the Azimuth plane of the antenna and is the horizontal plane in parallel with the mobile handset board. The YZ plane is the vertical plane which cuts through the mobile handset board in parallel with its longer side. The XZ plane is the vertical plane which cuts through the mobile handset board in parallel with its shorter side. The diagrams in fig. 4.5 can be used as a guide to the planes of the 2D cuts.

The radiation patterns are split into horizontal and vertical components for each cut and the data is plotted for each component separately. The data is plotted using polar coordinates with a scale ranging from -40dBi to +10dBi. Gain, directivity, pattern nulls and overall pattern shape can be clearly observed from the plots. Correlation between the measured data and simulated data predicted by CST can also be seen. It is worth noting that although only 3 cuts of the overall radiation pattern are presented, the measured efficiency was calculated using the full 3D pattern and so is an accurate representation of the total efficiency of the antenna.

Radiation Pattern 2D Cuts at 7.1GHz

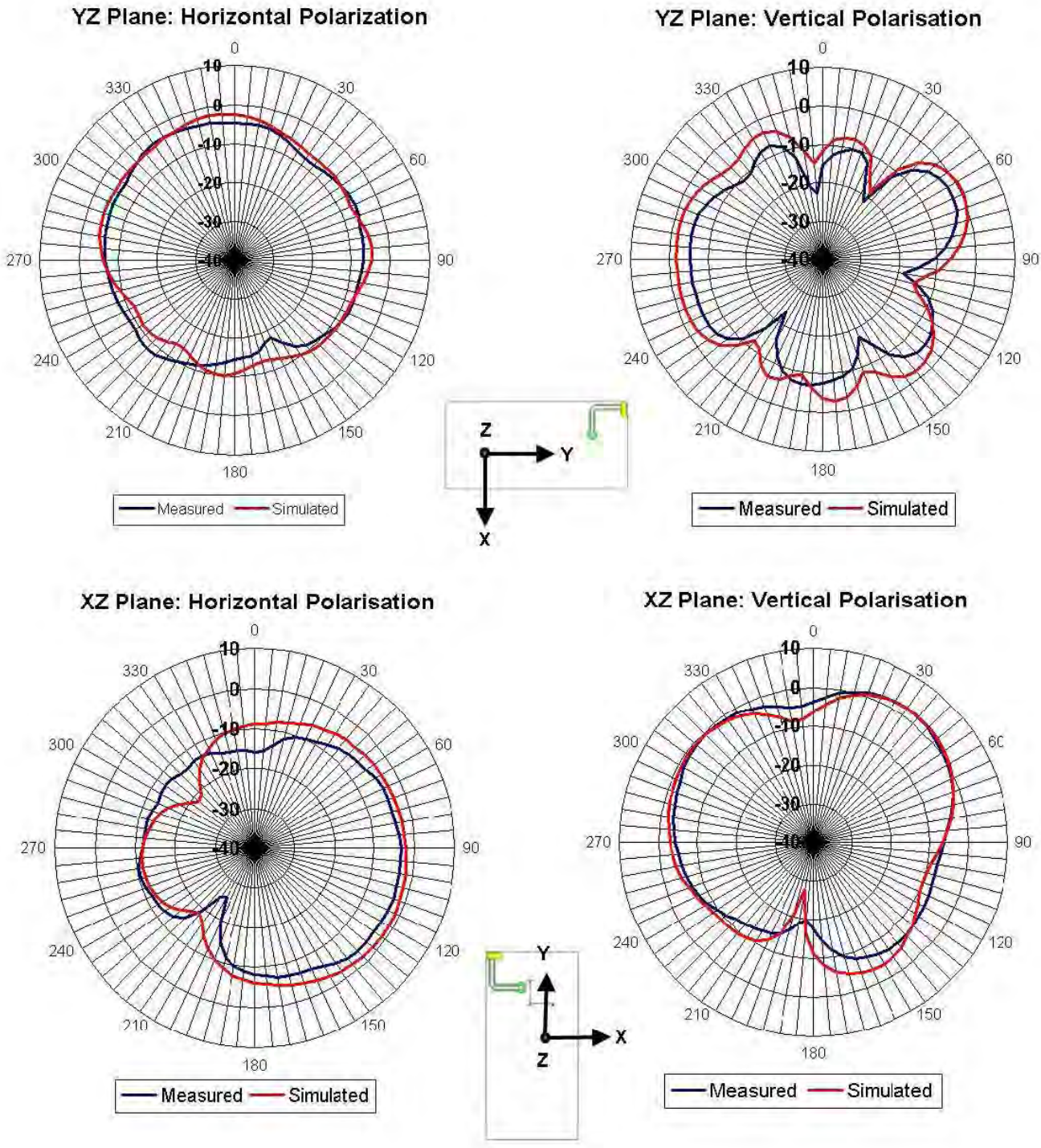

Fig. 4.5: Measured vs. Simulated 2D Radiation Pattern cuts at 7.1GHz for the UWB PIFA Antenna

Radiation Pattern 2D Cuts at 7.1GHz

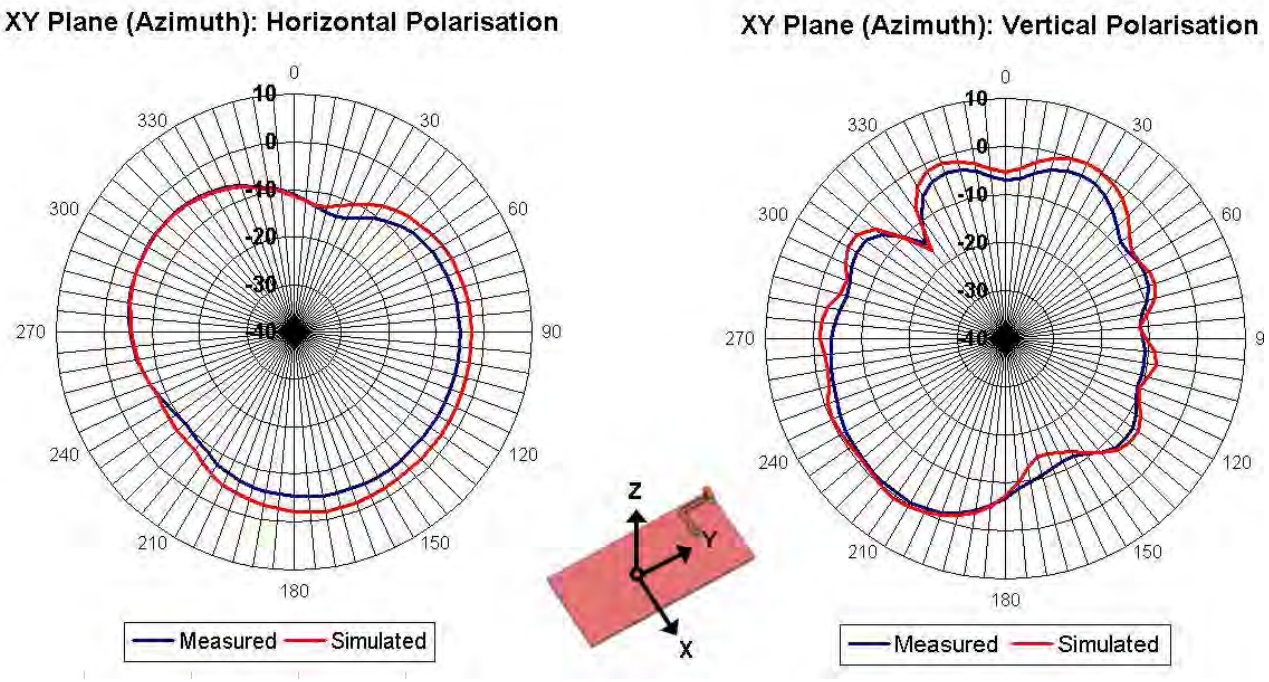

Radiation Pattern 2D Cuts at 8.4GHz

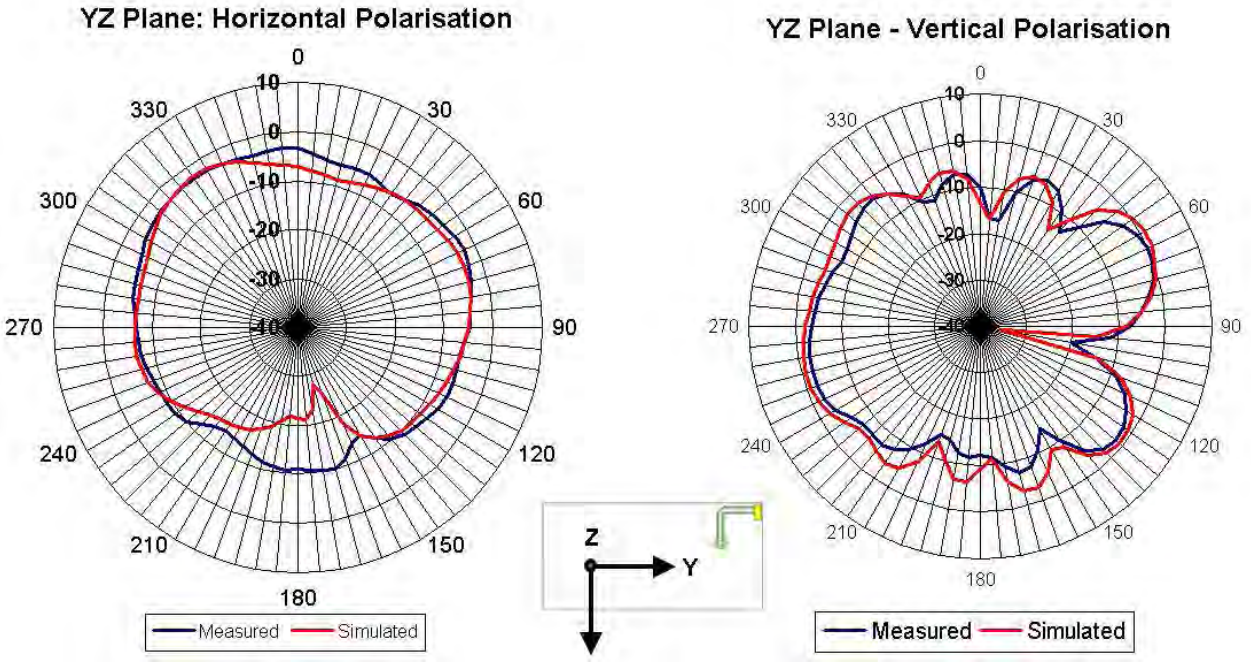

Fig. 4.5: Measured vs. Simulated 2D Radiation Pattern cuts at 7.1GHz, 8.4GHz for UWB PIFA Antenna

Radiation Pattern 2D Cuts at 8.4GHz

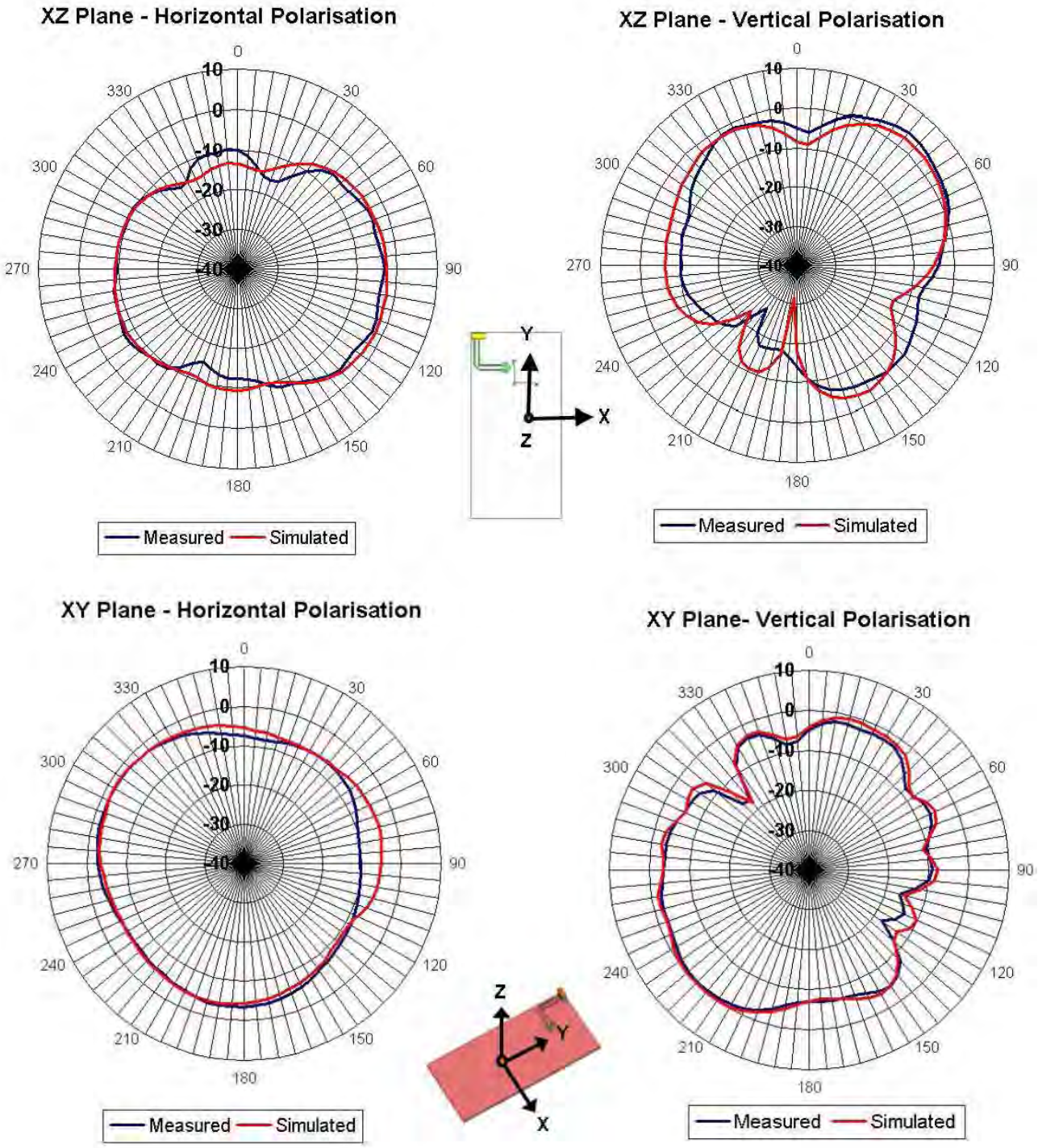

Fig. 4.5: Measured vs. Simulated 2D Radiation Pattern Cuts at 8.4GHz for UWB PIFA Antenna

As can be seen from the plots, correlation between measured and simulated radiation pattern data is good. The accuracy of the Satimo Starlab near-field measurement system which was used for the measurements during this research has been systematically improved over the past 24 months. A novel calibration technique has recently been introduced, which allows reliable calibration across all frequencies and thus provides particularly accurate measurements.

Although some nulls are evident, especially at the higher frequency, the patterns tend to be generally omni-directional. A maximum measured gain of 2.44dBi is observed at 7.1GHz, in the direction in which the open-circuit end of the PIFA is facing. This correlates well with the simulated prediction, which calculated a maximum simulated gain of 3.18dBi in the same direction. This can clearly be seen in the horizontal component of the XY (Azimuth) plane cut, where the 90° point is in line with the direction the open circuit end is facing. The peak gain is in this direction, while being skewed slightly to one side, due to the influence of the mobile handset ground plane.

4.6 Simulation & Measurement Correlation

Although a relatively good correlation was observed between simulated and measured data, in general, there will always be some degree of discrepancy between simulated and measured results. While it might not always be possible to align the simulated and measured data completely, it is useful to pinpoint the causes of the discrepancies. There are three main factors which tend to cause such discrepancies and they are outlined below.

4.6.1 Simulation Error

The first factor which may cause potential problems when correlating simulated and measured results is simulation error. As any electromagnetic simulation tool is based on a certain analytical calculation method, simulated results will only be as accurate as the simulation method. The knowledge and experience of the operator

are also critical factors, as they ensure the simulation environment is set up to model as accurately as possible the desired conditions. Errors can be introduced when simulation parameters such as frequency, mesh size, energy dissipated, boundary conditions etc., are set up incorrectly.

Some time was spent prior to this work on creating a reliable SMA connector model within CST, as well as ensuring all mobile handset test board and feed-line dimensions corresponded exactly to those used in the actual test set-up.

4.6.2 Measurement Error

The second factor which can lead to discrepancies is measurement error. As with simulated data, measured data is only as good as the measurement system used. If the measurement system is unreliable or faulty, measurements will be inconsistent, unreliable and inaccurate. When performing antenna gain and efficiency measurements, the quality of the near-field or far-field chamber is critically important. High quality absorber must be used to line the chamber and a suitable and accurate calibration must be carried out before all measurements. The Satimo Starlab near-field chamber for example, requires all 15 measurement probes to be calibrated using a system calibration involving a horn antenna, placed in a number of orientations within the chamber. Due to the broad bandwidth and relatively high frequency range of band group 3 & 6 UWB, a calibration of this nature can be tricky. If care is not taken it is surprisingly easy to perform a bad calibration leading to erroneous results.

4.6.3 Test Set-Up / Prototype Error

Other factors which can lead to erroneous measurement results include defects in the printed wiring board which is used to measure the antenna. If there are inconsistencies between the dimensions of the layer stack, the feed-line, the board itself, or even the dielectric constant of the dielectric material used as a substrate (in this case FR4) and the data which has been input into the simulation model,

inaccurate results will occur and correlation between the two will be poor. Similarly, errors can be introduced if the make-up and dimensions of the ceramic material and/or aluminium paste used in the actual antenna prototype are not exactly as specified in the model. For these reasons it is important to have very low tolerances on all dimensions and materials in the manufacturing process so as to minimise any errors which may be caused by these factors.

4.6 Summary

A measurement prototype of the UWB PIFA antenna designed in chapter 3 has been built up and measured to validate the simulated data presented previously. The prototype was built up using a standard screen-printing process to print the antenna patterns on the six faces of a ceramic block substrate using aluminium paste. The prototype was then mounted on an 80mm x 40mm mobile handset test board similar to the model used in the simulation work.

S11 data for the prototype has been measured and results confirm that the antenna achieves the required -6dB UWB in-band specification, as well as correlating well with simulated results. Near-field and far-field measurement techniques have been described for measuring efficiency, gain and radiation pattern data for a small antenna and a near-field measurement technique has been used to measure these characteristics for the UWB PIFA design. Measured efficiency, gain and radiation pattern data correlate well with simulated data and a reasonably omni-directional radiation pattern has been measured. Measured efficiency also achieves greater than the specified 50% across the band required for UWB operation. A brief review of potential causes of discrepancy between simulated and measured results has also been presented.

Chapter 5:
Low Band UWB - Antenna Simulation Work

5.1 Introduction

In this chapter a second antenna is proposed for integration into a mobile handset which will provide UWB functionality over the lower frequency band group 1 (3.1 – 4.8 GHz) band. The antenna has a novel 'dual-PIFA' type architecture which incorporates two separate PIFA antennas into a single feed antenna structure. The purpose of this is to allow two separate resonances to be excited which can be independently controlled and combined to achieve the broad bandwidth required. As with the high band UWB design, the antenna is printed on a ceramic chip to be mounted in the top corner of a mobile handset board.

A brief background of UWB band group 1 is presented as well as a review of the particular challenges facing antenna designers in this band. This is followed by a description of the proposed ceramic dual-PIFA antenna structure and the reasons for choosing it for this application. A parameterised model of the antenna is then created and a number of key parameter sweeps are presented and discussed. The design is then optimised for use in band group 1 and efficiency and S11 are presented for the final design.

Finally, a field and current analysis is carried out to gain some more insight into the operation of the antenna. Simulated E-field, surface current, far-field radiation patterns and peak gain are presented and discussed.

5.2 UWB Band Group 1

As described in the first part of this research, it is likely that UWB integration into mobile handsets will be crucial to the overall success of UWB as a technology. An antenna solution for integration into a mobile handset type device to provide UWB

functionality across band groups 3 & 6 was reviewed in chapters 3 & 4. The other UWB band of interest for mobile handset applications is band group 1, which is at the lower end of the UWB spectrum authorized by the FCC, and which has a bandwidth of 3.1 – 4.8 GHz. It is split up into 3 sub-bands of 528MHz each (see fig. 5.1). Although outside the US, channels 1 and 2 are unusable by UWB at present, by 2010 most territories plan to implement UWB across all band group 1 bands, with a Detect And Avoid (DAA) system in place to minimize interference with other services operating within the same bands.

As with specifications for band groups 3 & 6, there is a requirement for the antenna to have a good omni-directional pattern, efficiency of greater than 50% and an S11 of better than -6dB over an extremely wide bandwidth (the fractional bandwidth in this case is 43%). Even greater challenges face the antenna designer in this band group however, since achieving the required performance at these lower frequencies will inevitably require a larger electrical size in a device where volume is already severely limited. The likelihood of increased chip size will also lead to potential cost issues. On top of these size and cost issues, since the 3 – 5 GHz bandwidth is likely to be crowded with other services including WiMAX and LTE (as well as Bluetooth and WLAN operating close by) the regulations regarding EIRP limitations are even stricter than at the higher bands, with an EC imposed EIRP density limit of -85dBm/MHz in this area.

The above factors coupled with the already substantial issues associated with designing a small-size, high-efficiency, broadband antenna, create a unique and considerable challenge for the antenna designer.

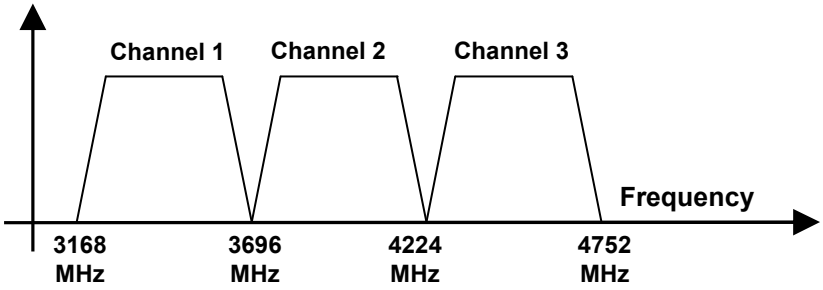

Fig 5.1: UWB Band Group 1 Sub-bands

5.3 'Dual-PIFA' Antenna

Following on from the research carried out in chapters 3 & 4, a number of novel and unique ceramic chip PIFA antenna options were investigated for UWB band group 1. Typical mobile handset specifications for UWB band group 1 antennas state a maximum height of 6mm and a maximum length of 20mm and these figures were taken into account when evaluating the antenna options. After extensive research into a number of novel structures, the one with the most potential to provide the performance required over the 3.1 – 4.8 GHz band was a 'dual-PIFA' structure as in fig. 5.2. This structure is designed to allow two separate resonances to be excited, independently controlled and ultimately combined to give the desired broadband performance across the 3.1 – 4.8 GHz band.

The overall structure of the antenna shares a lot of similar features with the high-band UWB PIFA structure from chapters 3 & 4. A CST model was built up using a similar test set-up to this antenna. As with the high-band UWB PIFA, the antenna was mounted on a standard 80mm x 40mm mobile handset test board consisting of an FR4 substrate sandwiched between two copper ground planes, which are connected together through the FR4 by cylindrical copper vias. The antenna was fed using an SMA connector attached to the underside of the test board, which connected through the board to a 50Ω ground-backed co-planar waveguide feed-line, which in turn connected to the input of the antenna. A parameterised model of the actual antenna structure was then created as in fig 5.2. A ceramic material with dielectric constant of 7.5 was used as in the high-band UWB PIFA case.

The dual-PIFA consists of a vertical feeding strip running from the input of the antenna to the top face of the block. Where the original antenna had one radiating element, the dual-PIFA has two separate radiating elements, facing opposite directions on the top surface of the block. These two radiating elements are fed using a forked feed structure and separated from each other on the block substrate. To allow the resonances to be independently controlled, two separate vertical ground strips, located on the opposite vertical face to the forked feed, connect each respective radiating element to the ground plane.

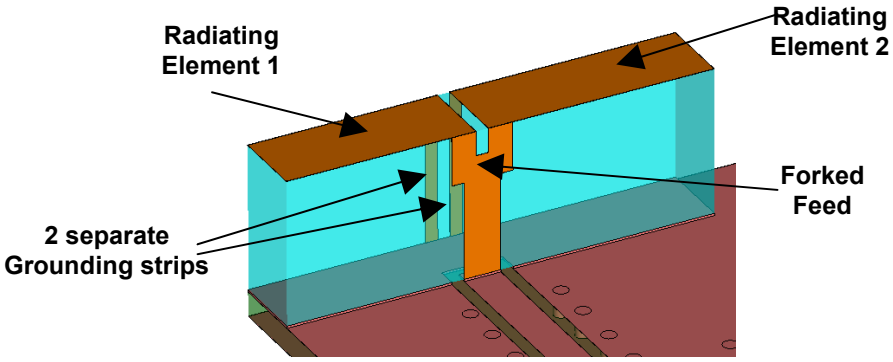

Fig. 5.2: CST Simulation Model of proposed Dual-PIFA Structure

The radiating elements are designed to excite two separate resonances within the 3.1 – 4.8 GHz band, which are similar in frequency but spaced some distance apart. The aim of this is to allow the two resonances to be combined, resulting in a broadband response which can be optimized to cover the desired band group 1 bands. 'Radiating element 1' in fig. 5.2 above excites the higher of the two resonances and 'Radiating element 2', which is slightly longer, will excite the lower resonance. The parameterised model was used to optimise the dimensions of the radiating elements along with the positions and dimensions of the forked-feed structure and the grounding strips.

It is worth noting that one significant difference between the PIFAs of this structure and the high-band UWB PIFA is that the grounding strips are now on the opposite face of the ceramic block to the feeding strip. In the high-band UWB PIFA, the ground strip was on a perpendicular face to the feed and so there were a number of degrees of freedom which could be adjusted to get the optimum feed-ground distance. In the dual-PIFA structure, the distance between feed and ground is restricted by the block width. This width restricts the minimum distance possible between feed and ground and limits somewhat the optimum match possible at the input.

5.4 Optimisation: Simulated Parameter Sweeps

To illustrate the operation of the proposed dual-PIFA antenna structure, a number of simulated CST parameter sweeps are presented. Firstly, to demonstrate how the separate PIFA radiating elements excite two respective resonances which can be independently controlled, the lengths of the radiating elements are swept and the resulting S11 and impedance characteristics observed.

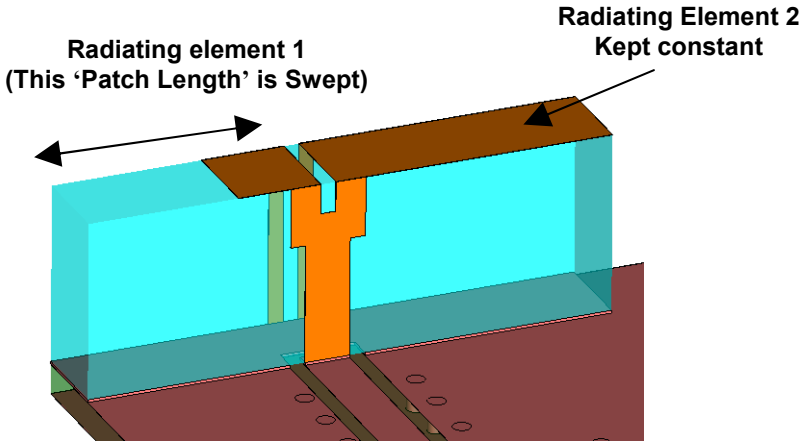

Fig. 5.3: Radiating Element 1 Parameter Sweep

5.4.1 Sweep 1: 'Radiating Element 1' Length

The length of the 'Radiating Element 1' patch is swept from 3.75mm to 7.75mm, as in fig. 5.3. The resulting real value of the input impedance (Ω) and S11 (dB) vs. frequency (GHz) are plotted in fig. 5.4. The resonance at around 3GHz on the impedance plot represents a board resonance due to the mobile handset test board. The resonance which is evident at just below 4GHz on the impedance plot is due to the resonance of 'Radiating Element 2'. As can be seen from the plot, since the dimensions of this element are not changing, the position of this resonance remains essentially constant as the length of the other element is swept. The resonances which are evident ranging from around 4.7GHz to 5.8GHz correspond to various lengths of 'Radiating Element 1', the orange characteristic representing

a patch length of 7.75mm, which brings the element right to the edge of the ceramic block. It is clear from the plots that as the length of 'Radiating Element 1' is increased, this second resonance is pulled down in frequency. From the corresponding S11 plots we can see that as the upper resonance is pulled down close enough to the stationary lower resonance, the responses of the separate resonances begin to combine, creating a broad-band response.

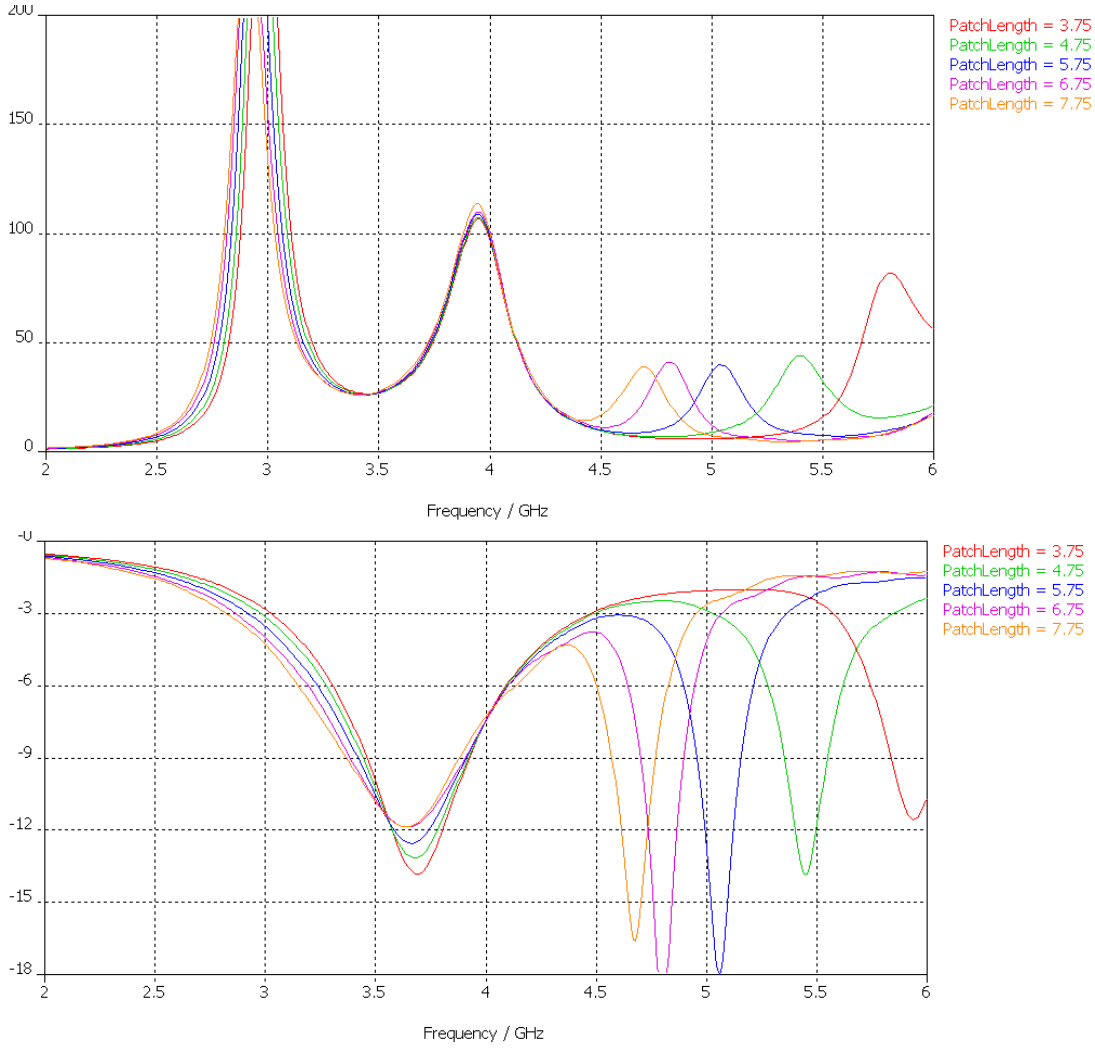

Fig. 5.4: (a) Real part of the Input Impedance (Ω) and (b) S11 (dB) vs. Frequency (GHz) as length of 'Radiating Element 1' is swept

The dual-PIFA structure will be optimised using this broad-banding technique to endeavour to provide an antenna which meets the required UWB specifications over the entire UWB band group 1 band. As long as good understanding and control of the separate narrow-band resonances exists, there is potential to obtain distinctly large fractional bandwidths from a relatively small-size antenna structure.

5.4.2 Sweep 2: 'Radiating Element 2' Length

The second parameter sweep presented illustrates how the frequency of the lower resonance (which remained constant during the previous sweep) can be controlled by sweeping the length of the 'Radiating Element 2' patch from 5.25 to 9.25mm as in fig. 5.5 (9.25mm corresponds to the patch reaching the edge of the ceramic block). The resulting real value of the input impedance (Ω) and S11 (dB) vs. frequency (GHz) and are plotted in fig. 5.6.

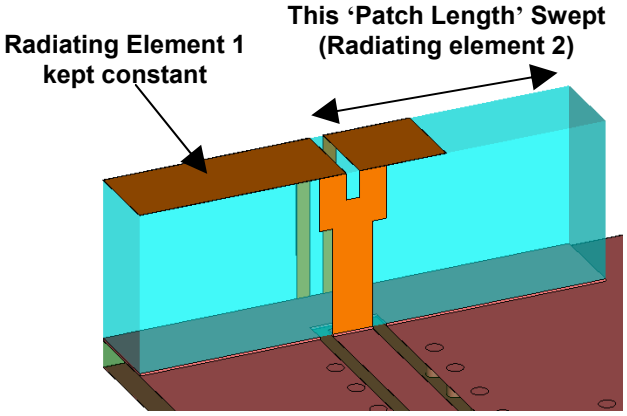

Fig. 5.5: Radiating Element 2 Parameter Sweep

As can be seen from the input impedance plots, the upper resonance due to 'Radiating Element 1' remains static at around 4.75 GHz. As 'Radiating Element 2' is reduced in length, the lower resonance at just below 4GHz is pushed up in frequency until it finally merges with the upper resonance. The corresponding S11

plot illustrates clearly how combining the two relatively narrow-band resonances can create the desired broad-band response.

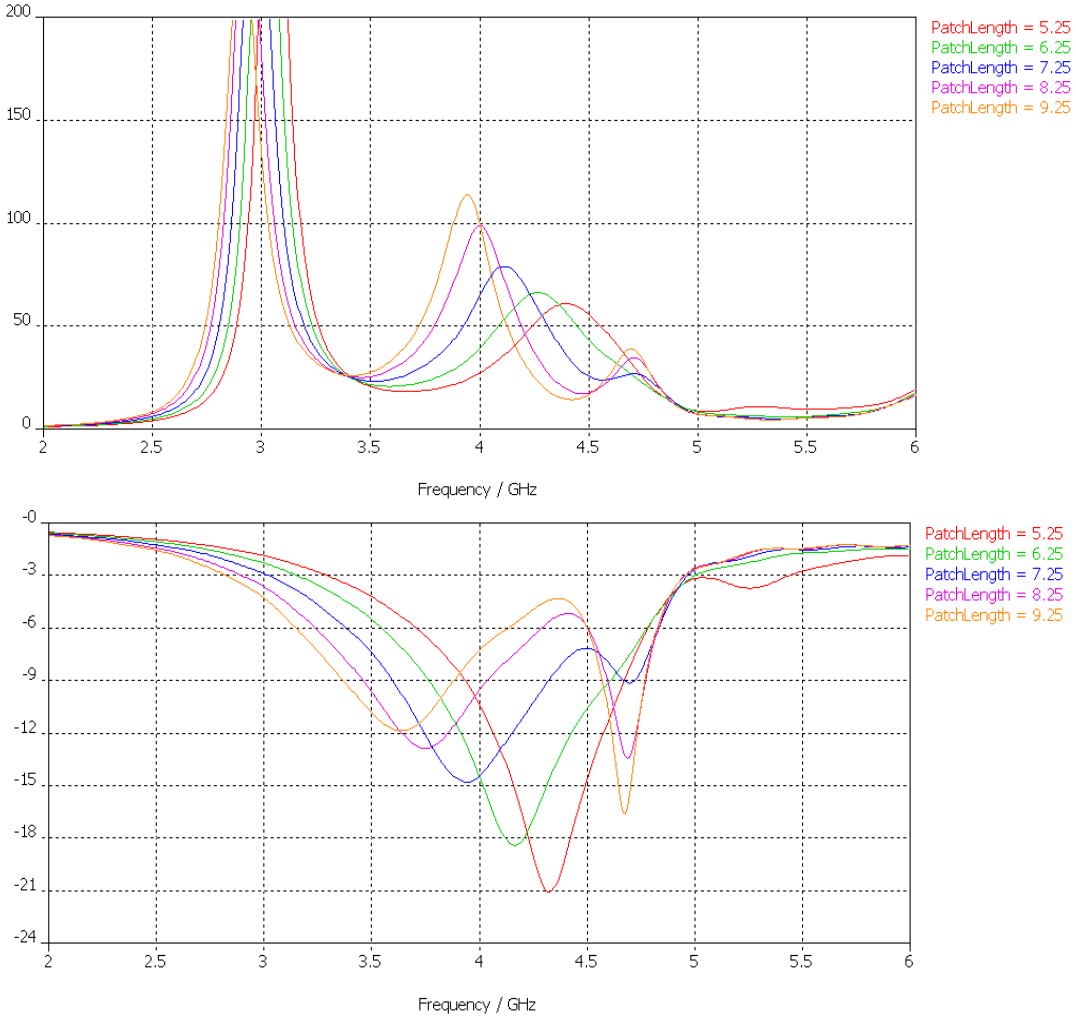

Fig. 5.6 (a) Real part of the Input Impedance (Ω) and (b) S11 (dB) vs. Frequency (GHz) as the length of 'Radiating Element 2' is swept

It is clear from this sweep that the lower resonance can be controlled independently of the upper resonance. Since both resonances can be controlled exclusively, we now have the capability to optimise them separately to achieve a potentially broad bandwidth.

5.4.3 Sweep 3: Ceramic Dielectric Constant

To illustrate the dielectric loading effect of the ceramic block, a parameter sweep of the dielectric constant of the block is presented. The dielectric constant was swept from 3.5 to 9.5 and the resulting real value of the input impedance and S11 plots are shown in fig. 5.7. As can be seen from the impedance plot, as the value of the dielectric constant is increased, both the upper and lower resonances are loaded and shifted down in frequency.

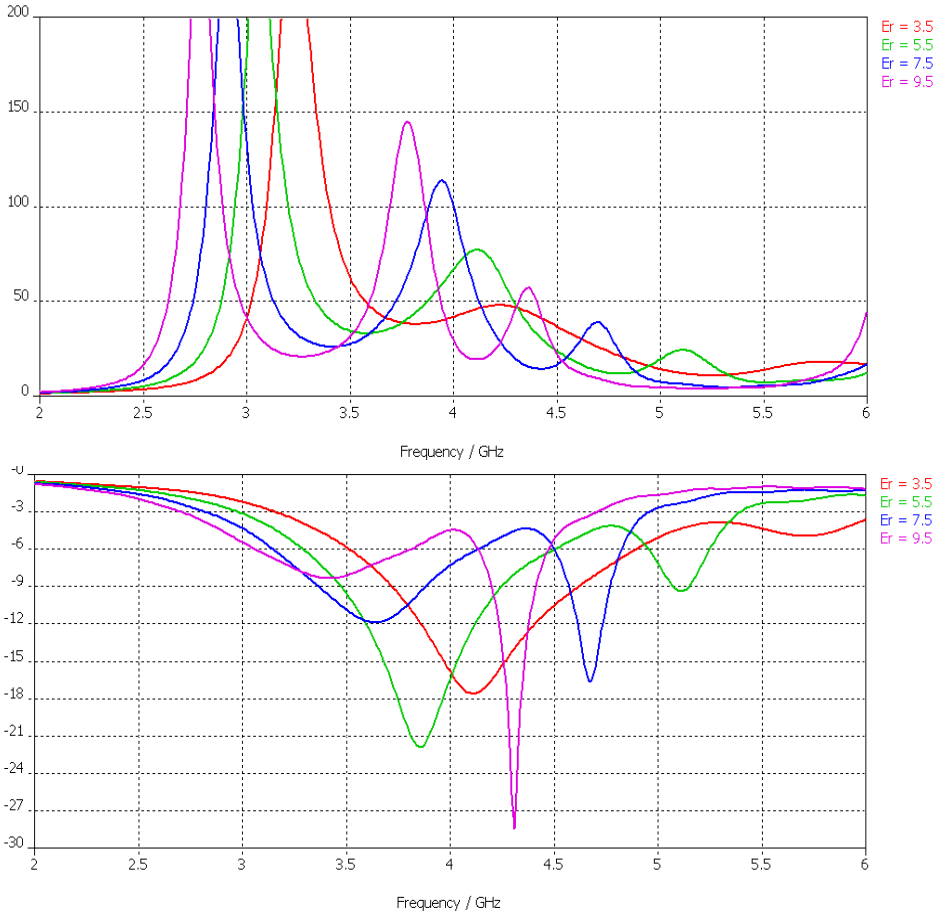

Fig. 5.7 (a) Real part of the Input Impedance (Ω) and (b) S11 (dB) vs. Frequency (GHz) as dielectric constant of the ceramic block is swept

As an example, in the red plot, which corresponds to a dielectric constant of 3.5, the two resonances can be seen at around 4.75 and 5.75GHz. When the dielectric constant is increased to 9.5 (pink plot), these resonances have shifted down to 3.8GHz and 4.85GHz respectively. Increasing the dielectric constant tends to increase the *Q* for a PIFA antenna and thus reduces the overall bandwidth. For this reason, there will always be a trade-off between low frequency performance and bandwidth.

It is also worth noting that the real value of the input impedance at resonance increases as the dielectric constant increases. A value of 7.5 was chosen as for the previous design.

5.4.4 Sweep 4: Fork Sweep

To illustrate how the dual-PIFA design can be optimised further, a sweep of the forked feed is presented. The sweep varies the vertical point along the feed at which the feed splits in two or 'forks' to connect to each separate radiating element as in fig. 5.8. The figure shows one position of the forked feed, with the swept parameter 'ForkTop' = 3mm. This parameter was swept from 1mm to 4mm and the resulting plots are shown in fig. 5.9.

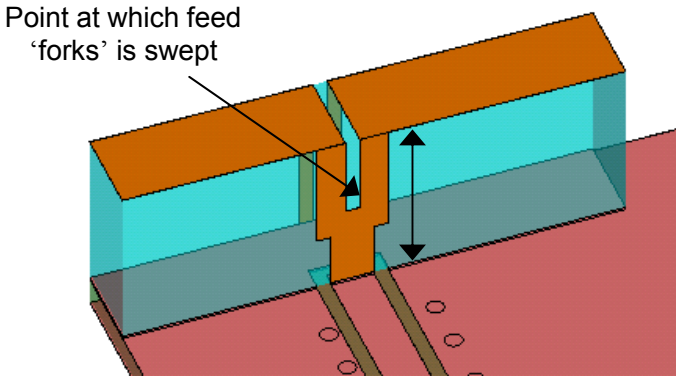

Fig. 5.8: Forked Feed Sweep – Point at which feed splits into two is swept (figure shows ForkTop = 3mm)

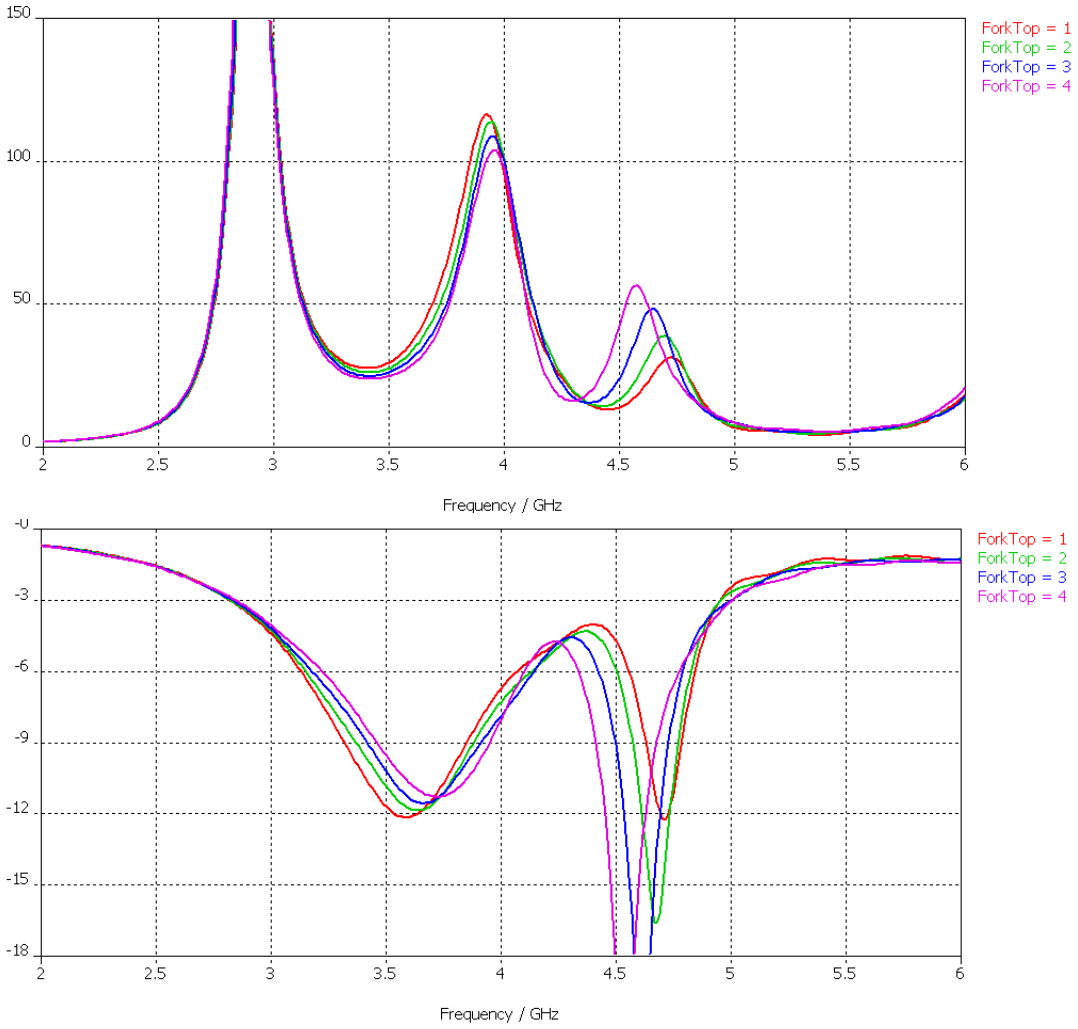

Fig. 5.9 (a) Real part of the Input Impedance (Ω) and (b) S11 (dB) vs. Frequency (GHz) as 'Radiating Element 2' is swept

Optimising the exact dimensions of the fork allows us to fine-tune the antenna response. As can be seen from the plots, adjusting the point at which the feed forks for example, effects both the lower and upper resonances. As the point at which the feed forks is shifted down (ForkTop=1mm corresponds to the feed forking at the very top of the block, while ForkTop=4mm has the feed splitting towards the bottom of the block), the lower resonance is shifted up in frequency slightly, while the upper resonance is shifted down. Similarly the value of the real part of the impedance is shifted down for the lower resonance and up for the upper resonance.

These effects are due to a small amount of inductive loading caused by the relatively narrow portions of the forked feed after it splits in two. Since the effect on each resonance is slightly different, an optimum position for the forked feed can be found which provides an optimum balance of good performance between the two resonances. This is found to be at the point ForkTop=2mm. At this point we get the optimum balance of performance between top and bottom ends of the bandwidth.

5.5 Final Simulated Dual-PIFA Design

After extensive optimisation of the dimensions described above as well as a number of other parameters including block height, block width, grounding strip width, grounding position etc., a final design was chosen which gave the best overall performance across the required bandwidth. The final design has dimensions as in fig. 5.7 (all dimensions are in millimetres) and efficiency and S11 responses as in fig. 5.8.

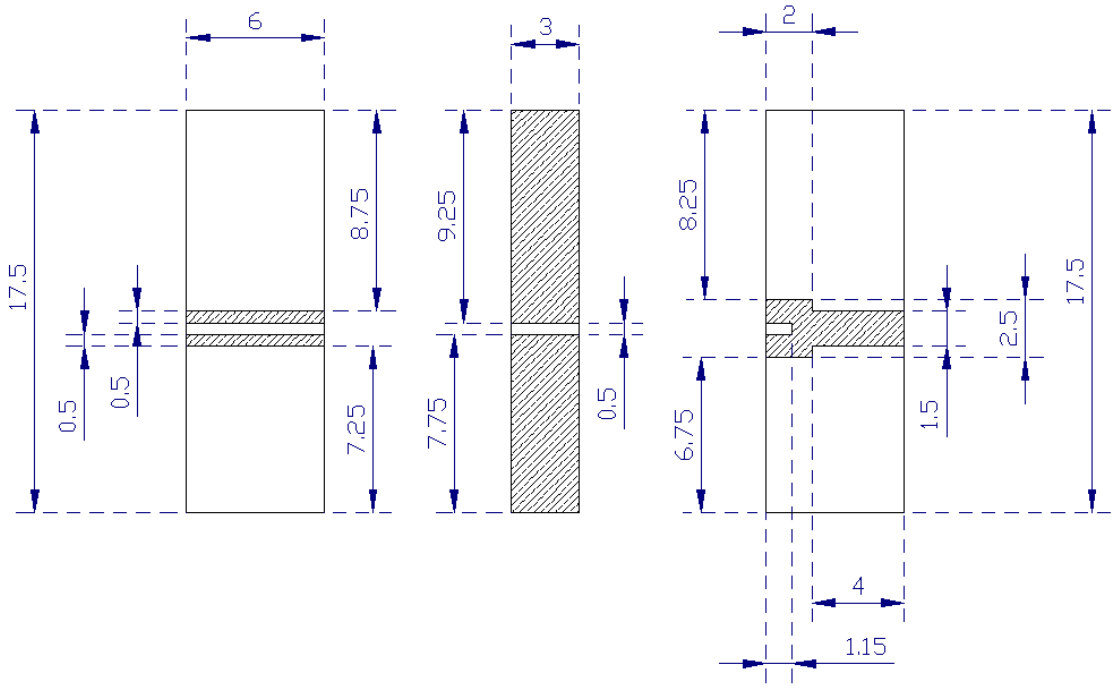

Fig. 5.7: Main dimensions of final Dual-PIFA design (all dimensions in mm)

As can be seen from the S11 plot in fig. 5.8, the two resonances of the dual-PIFA structure have been combined to give a -4dB bandwidth which covers the 3.1 – 4.8 GHz band. This response is reasonably good but due to the re-entrance which occurs at around 4.35GHz, the -6dB requirement is not met across the band. The corresponding efficiency is however greater than 50% across this bandwidth. To reduce this re-entrance we will use the technique of external matching at the input described for the high-band UWB PIFA.

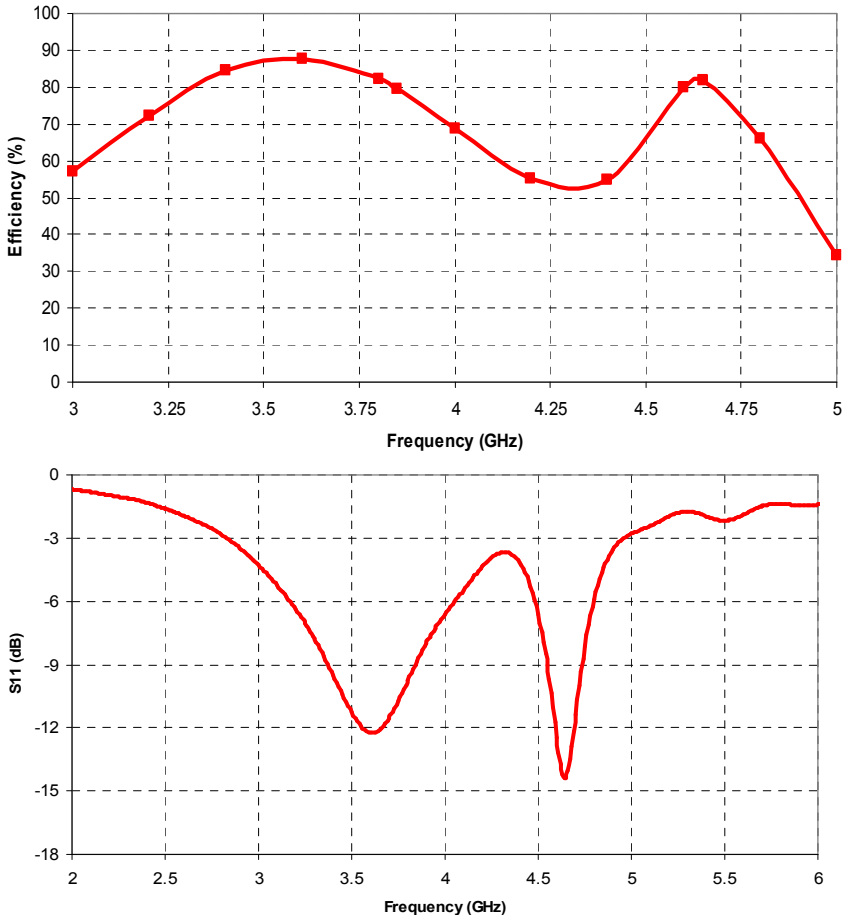

Fig. 5.8: Plots of (a) Efficiency (%) and (b) S11 (dB) vs. Frequency (GHz) for Dual-PIFA antenna

It is worth noting that the performance of the antenna could potentially be further improved by adding cavities to the ceramic block substrate. This facility was not

available to the author but block ceramic etching techniques exist to implement this kind of design. Introducing a cavity within the block ceramic and controlling its size and shape could allow more control over the dielectric loading effect of the ceramic block and potentially allow the bandwidth to be increased further.

An external matching circuit as in fig. 5.9 was used to tune the response around 4.35GHz and improve the match in this area. The aim of this was to minimise the re-entrance and thus optimise the performance of the antenna around this frequency, allowing the antenna to achieve the required -6dB S11 across the entire 3.1 – 4.8 GHz band. Smith chart data illustrating the improved match from 4 – 4.5 GHz is shown in fig. 5.10 and the results of the simulated external matching are presented in fig. 5.11. Simulated efficiency and S11 for both the matched and unmatched antenna are compared.

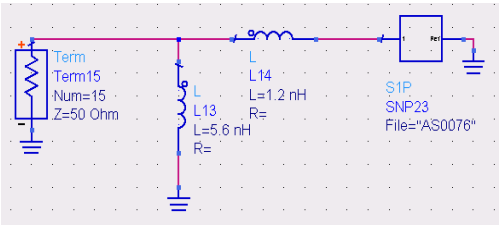

Fig. 5.9 External Matching Circuit for Dual-PIFA Antenna

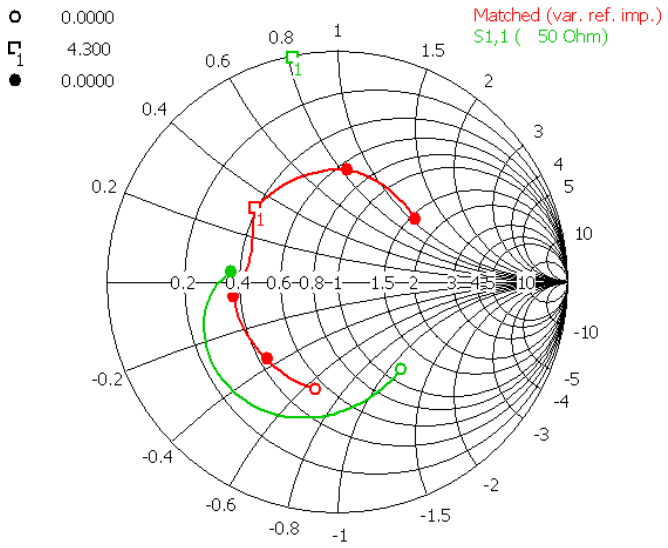

Fig. 5.10:Input Impedance of Antenna without matching (green) and with matching (red) from 4 to 4.5 GHz (Smith chart normalised to 50Ω).

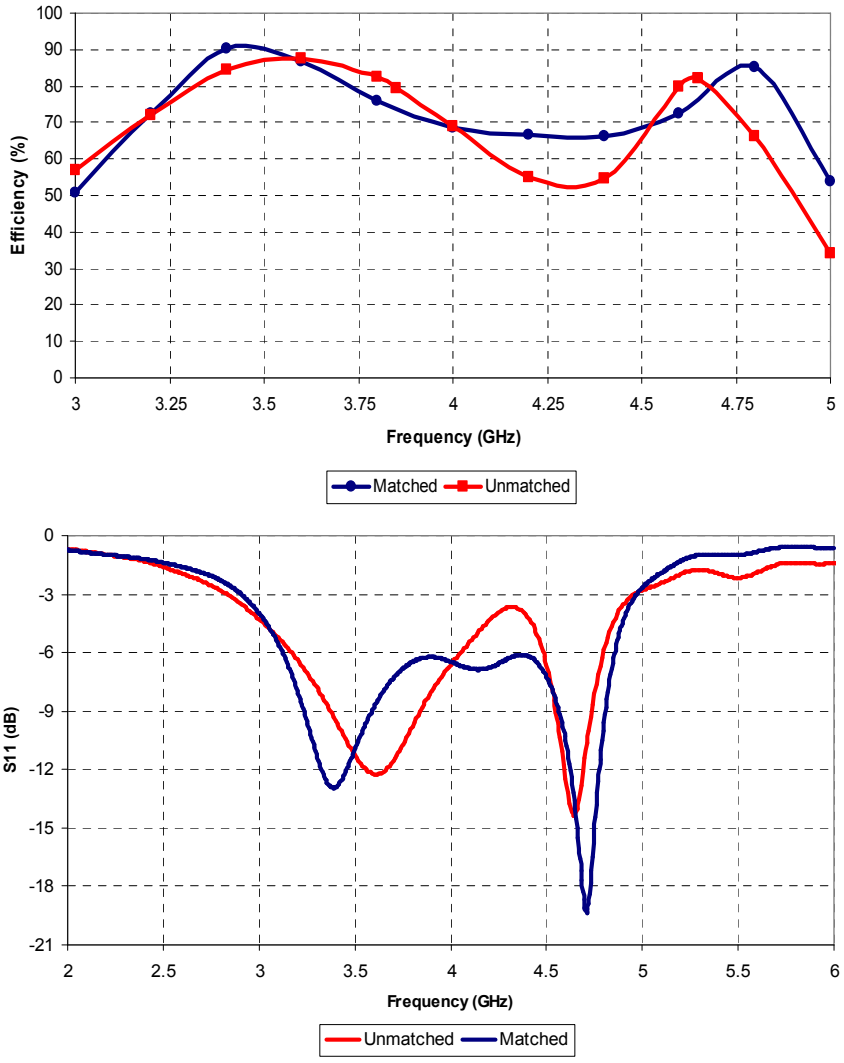

Fig. 5.11: Plots of (a) Efficiency (%) and (b) S11 (dB) vs. Frequency (GHz) for matched and unmatched dual-PIFA antenna

As can be seen from the plots, with the external matching circuit implemented, the re-entrance which was evident at 4.35GHz in the S11 response has been neutralised and we now have an S11 response which achieves the required -6dB across the band. The corresponding efficiency is also above 50% across the band.

5.6 Field and Current Analysis at Resonant Frequencies

To gain some more insight into the operation of the antenna, surface current, E-field, peak gain and radiation patterns at the fundamental resonance frequencies are presented and discussed.

5.6.1 Surface Currents

Fig 5.11 shows the absolute value of the surface currents on the structure at the two fundamental resonances of 3.65GHz and 4.7GHz respectively. Surface current is measured in Amps per Metre. At 3.65GHz, 'Radiating Element 2' is resonating and there is maximum current at the input of the antenna and minimum current at the open-circuit end of the horizontal radiating element. This represents the quarter-wave resonance which runs from the input of the antenna to the end of

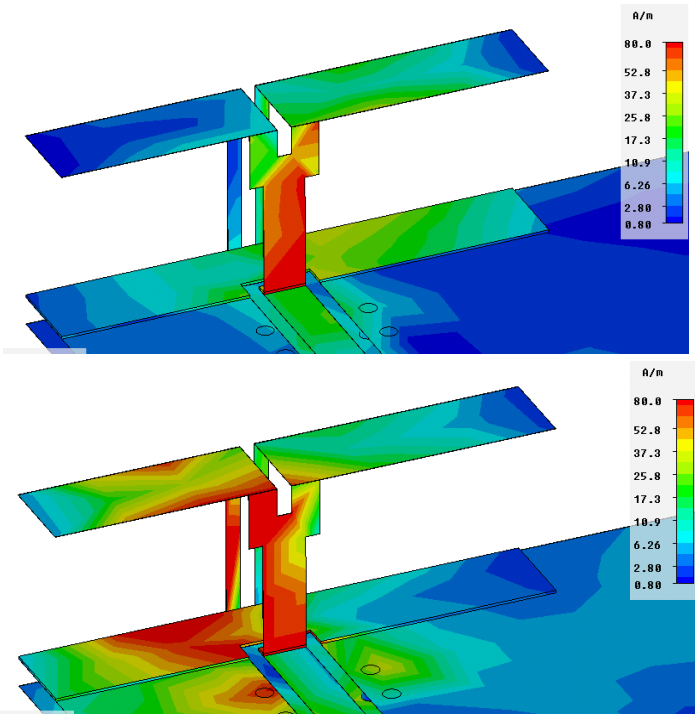

Fig. 5.11: Surface currents in the dual-PIFA structure at (a) 3.65GHz and (b) 4.7GHz

'Radiating Element 2'. At this frequency 'Radiating Element 1' is contributing very little to the overall performance of the antenna.

At 4.7GHz 'Radiating Element 1' is resonating and the quarter-wave resonance along this element can be clearly seen in this case. The maximum current is at the antenna input and minimum current at the open-circuit end of 'Radiating Element 1', while 'Radiating Element 2' contributes little to the performance of the antenna at this frequency. The broad bandwidth of this novel antenna structure is achieved by allowing 'Radiating Element 2' to operate over the lower end of the bandwidth while 'Radiating Element 1' covers the upper end.

5.6.2 E-Field

Fig 5.12 shows the E-fields around the structure at the two fundamental resonances of 3.65GHz and 4.7GHz respectively. E-field is measured in Volts per Metre. As we saw with the surface currents, at 3.65GHz, 'Radiating Element 2' is resonating and the maximum E-field is at the open-circuit end of this element and minimum E-field is at the input to the antenna. This represents the quarter-wave resonance which runs from the input of the antenna to the end of 'Radiating Element 2'. As we saw before, at this frequency 'Radiating Element 1' is contributing very little to the overall performance of the antenna.

At 4.7GHz it is 'Radiating Element 1' which is resonating and the quarter-wave resonance can also be clearly seen in this case. The maximum E-field is at the open-circuit end of 'Radiating Element 1' and the minimum E-field is again at the input to the antenna. Radiating Element 2 contributes little to the performance of the antenna at this frequency.

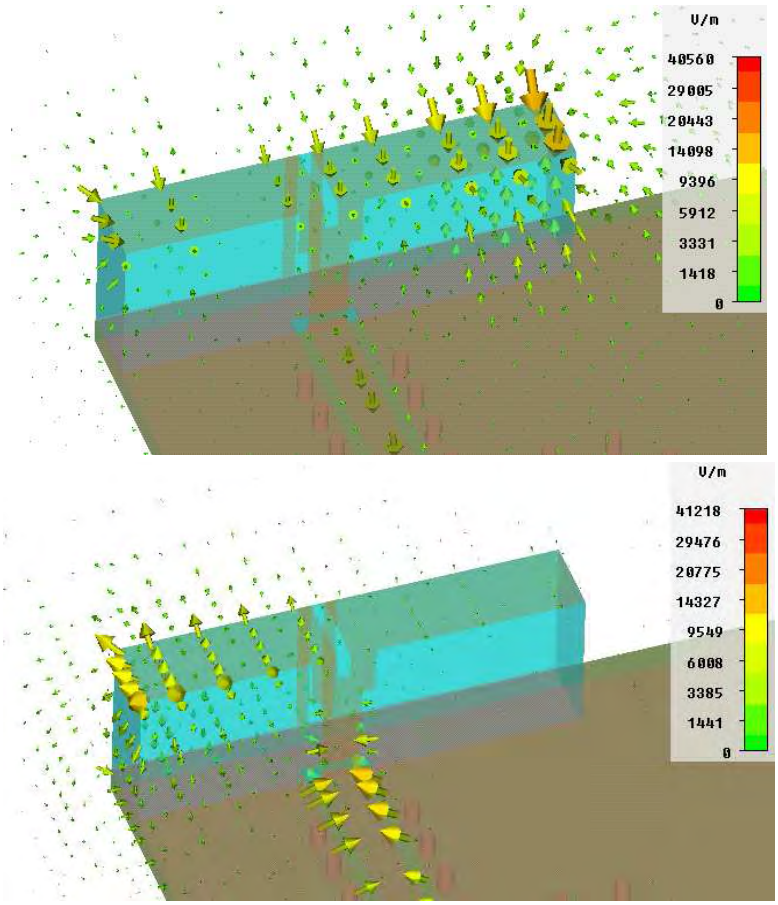

Fig. 5.12: E-fields around the dual-PIFA structure at (a) 3.65GHz and (b) 4.7GHz

5.6.3 Far-Field Radiation Patterns

The directivity and gain of the dual-PIFA antenna can be examined by observing simulated radiation pattern plots at the resonant frequencies. These will be compared with measured results in chapter 6. Fig. 5.12 shows radiation pattern plots for the antenna at the lower resonant frequency of 3.65GHz. Gain is measured in dBi. As can be seen from the plots, the overall pattern of the antenna is fairly omni-directional with very few nulls evident. As we discussed before, omni-directionality is critical for reliable UWB performance within a mobile handset environment, due to the constantly changing location and orientation of the handset.

Unlike the high-band UWB PIFA design described in chapters 3 & 4, the direction of peak gain of the dual-PIFA is not in line with the direction that either open-circuit end of the structure is facing. At 3.65GHz, since the 'Radiating Element 2' element dominates, the direction of peak gain leans towards the direction that the open circuit end of this side of the antenna structure is facing and has a value of 4.6dBi.

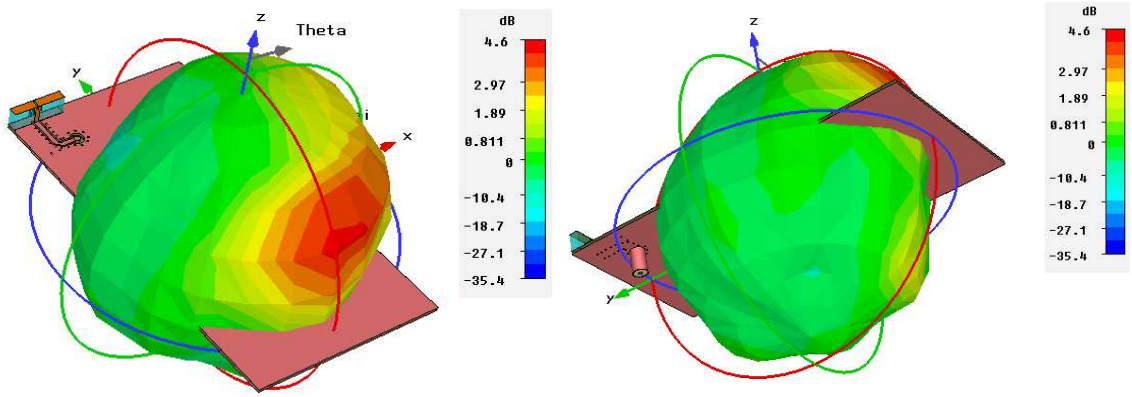

Fig. 5.12: Simulated Radiation Pattern plots for Dual-PIFA Antenna at 3.65GHz

Fig. 5.13 shows the radiation pattern of the dual-PIFA at the upper resonance at 4.7GHz. As can be seen from the figure the antenna exhibits a good omni-directional pattern and there are few nulls evident. As the 'Radiating Element 1' element dominates at this frequency, the direction of peak gain leans slightly towards this side of the antenna structure. The value of the peak Gain at 4.7GHz is 3.15dBi. These results will be compared with measured results in chapter 6.

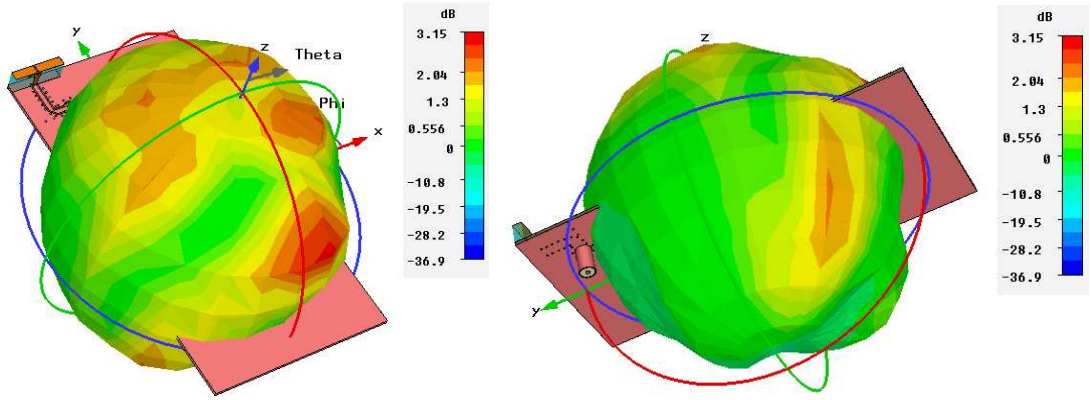

Fig. 5.13: Simulated Radiation Pattern plots for Dual-PIFA Antenna at 4.7GHz

5.7 Summary

An antenna design has been presented for integration into a mobile handset to cover UWB band group 1 (3.1 – 4.8 GHz). Due to the considerable demands on performance and restrictions on size at these frequencies, a novel dual-PIFA type structure has been proposed for this application. The structure is printed on a ceramic chip, similar to the high-band UWB PIFA described in earlier chapters, but consists of two separate PIFAs fed by a forked feeding structure, which can be independently controlled and their responses combined to achieve the broadband performance required. The final structure has dimensions of 17.5mm x 6mm x 3mm which is within the specifications for integration into a mobile handset. Block ceramic material with dielectric constant = 7.5 similar to the high-band UWB PIFA, was used.

To illustrate the operation of the antenna, a number of parameter sweeps which were used in the optimisation of the design have been presented. The ability to independently control the two resonances has been demonstrated by sweeping each radiating element separately and observing the resulting input impedance and S11 responses. How the two resonances can then be combined to achieve the desired broadband response has also been illustrated and discussed. Efficiency and S11 plots for the final design have been presented, with the antenna achieving the required >50% efficiency across the band group 1 band, while an S11 of -4dB is achieved across the band. This could be improved further by external matching or potentially by the introduction of cavities to the ceramic block substrate.

A surface current and field analysis at the resonant frequencies has also been presented to give some more insight into the operation of the antenna. Both quarter-wave resonances which make up the broadband response of the antenna have been illustrated using surface current plots and the maximum gains of the antenna have also been presented. At the lower resonance of 3.65GHz, the antenna has a maximum gain of 4.6dBi and at the upper resonance of 4.7GHz, the antenna has a maximum gain of 3.15dBi. These results will be confirmed by measurement in chapter 6.

Chapter 6:
Low Band UWB – Antenna Measurement

6.1 Introduction

Prototypes of the dual-PIFA antenna proposed in the previous chapter are built up and measured to verify simulated data. S11, gain, efficiency and radiation patterns are measured and the correlation between measured and simulated data is observed. For S11 correlation, both the matched and unmatched responses are compared and the correlation between the two is analysed. Radiation pattern measurements are presented as 2-dimensional cuts of the 3-dimensional radiation pattern, taken on three orthogonal planes as with the high-band UWB PIFA. Measurements are compared to simulated radiation patterns and the correlation discussed.

6.2 Measurement Prototypes

As with the high-band UWB PIFA, a number of prototype samples were built up using the standard block ceramic printing process described previously. The required antenna pattern is printed onto the six faces of a block of ceramic material using an aluminium paste. A ceramic material with a dielectric constant of 7.5, similar to the one used for the high-band UWB PIFA prototypes, was used. The dimensions of the ceramic block were 17.5mm x 3mm x 6mm (a total volume of 315mm^3) as in the simulation model. Fig. 6.1 shows some samples of the measurement prototypes.

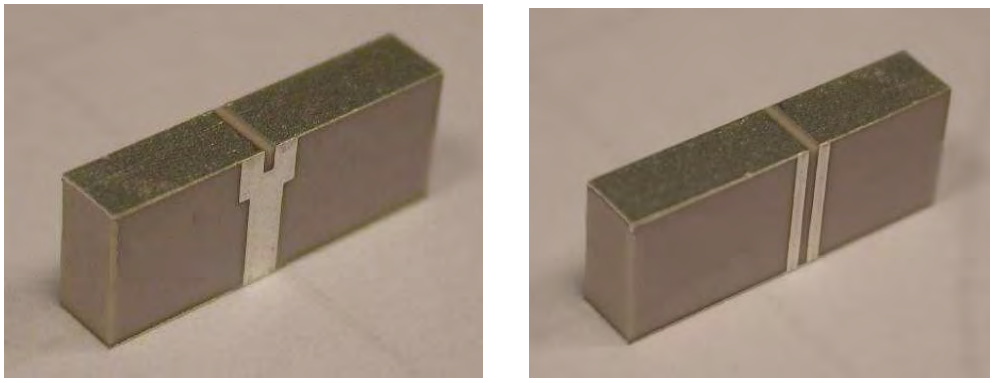

Fig. 6.1: Front and back of UWB Dual-PIFA measurement prototype

As with the high-band UWB PIFA Antenna, a prototype was mounted on a test board, similar in dimensions and layout to the simulated mobile handset test board (80mm x 40mm FR4 substrate with copper ground planes on both sides connected together by copper via-holes) and with a similar feed-line structure (see fig. 6.2). An SMA connector was attached to the underside of the board, corresponding to the simulated SMA model which had been used for all simulations. As was mentioned before, the aim was to have the simulation setup as close as possible to the actual measurement setup, to aid in correlation of the simulated and measured data.

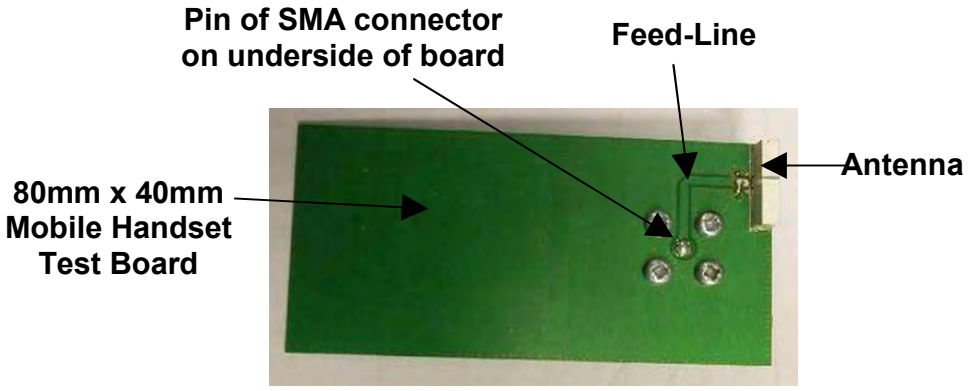

Fig. 6.2: Dual-PIFA Measurement Prototype mounted on 80mm x 40mm Mobile Handset style test board

6.3 S11 Measurements

S11 data across UWB band group 1 was measured. As described in chapter 5.5, a similar external matching technique to the one used in the high-band UWB PIFA case was also used here. An external matching circuit consisting of a shunt chip inductor and a series chip inductor was mounted on the test board at the input of the antenna to optimise the performance. To demonstrate the correlation between measured and simulated results, both the matched and unmatched data are presented here. Fig. 6.3 shows measured and simulated S11 (dB) vs. frequency (GHz) data for the unmatched antenna across the 3.1 – 4.8 GHz band.

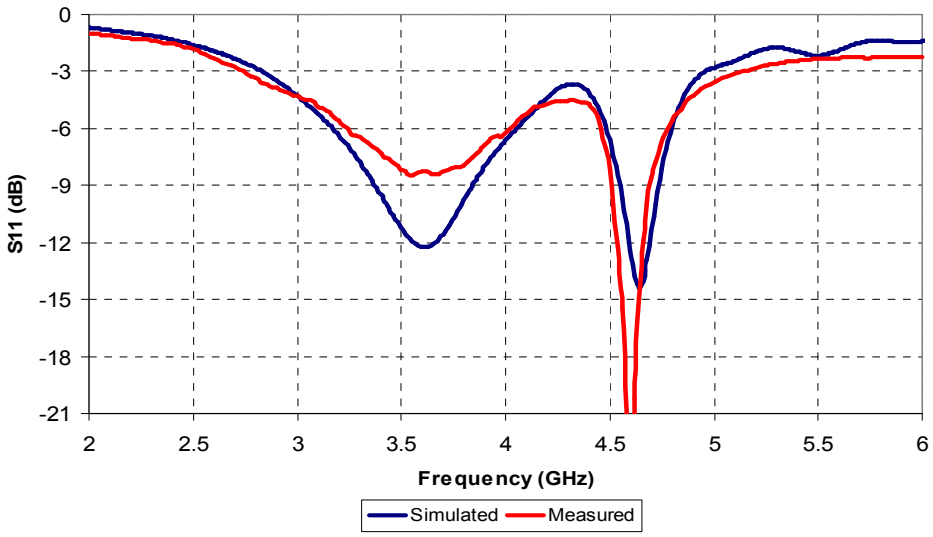

Fig. 6.3: Measured vs. Simulated S11 (dB) vs. Frequency (GHz) for the unmatched Dual-PIFA Antenna

As can be seen from the plot, there is good correlation between measured and simulated data. The frequencies of the fundamental resonances are almost identical in both cases, with the only difference being in the match at these resonances. The simulation predicts a better match at the lower resonance and thus a slightly broader bandwidth than is actually measured, but overall the bandwidths are very similar. The re-entrance predicted by the simulation, which occurs between the two resonances at 4.35GHz, is also present in the measured data. An external matching circuit as described in chapter 5.5 was used to minimise this re-entrance and thus optimise the performance of the antenna around this frequency.

Fig. 6.4 shows measured and simulated S11 (dB) vs. frequency (GHz) data for the matched antenna across the 3.1 – 4.8 GHz band. The correlation between measured and simulated data is not as good as was seen in the unmatched case. This is most likely due to the ideal matching component models used by the simulator. The real components tend to exhibit parasitic capacitances or inductances at frequencies above 3GHz which are not accurately modeled by the ideal component models. In some cases it is necessary to re-tune the matching circuit for the measurement set-up due to these discrepancies between simulated and measured performance of the matching components.

As can be seen from the plots, the re-entrance at around 4.35GHz has been reduced greatly by the matching circuit in both simulated and measured data and we now have a measured antenna response which exhibits an S11 of -6dB across UWB band group 1. Thus the antenna S11 performance required for UWB operation at these frequencies has been achieved.

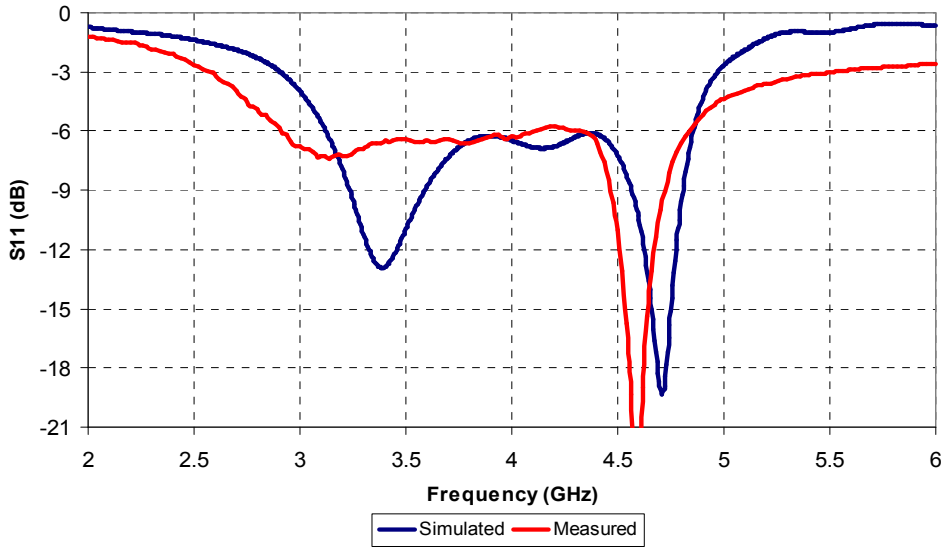

Fig. 6.4: Measured vs. Simulated S11 (dB) vs. Frequency (GHz) for the Matched Dual-PIFA Antenna

6.4 Efficiency Measurements

The total efficiency of the dual-PIFA antenna was measured using the Satimo near-field measurement chamber as described in chapter 4.3. Fig. 6.5 shows a comparison of measured and simulated responses for the total antenna efficiency (%) vs. frequency (GHz) across the 3.1 – 4.8 GHz band. This data includes the external matching circuit described previously. Again, correlation between measured and simulated data is good, although the overall efficiency of the measured samples is 10 - 20% lower than that predicted by the simulation. Total efficiency across the band for the measured prototype still looks extremely good however, with an efficiency of greater than 50%, across the UWB band group 1. This performance is good enough to provide reliable UWB performance across this entire bandwidth while the antenna itself remains physically small enough to be ideal for mobile handset integration.

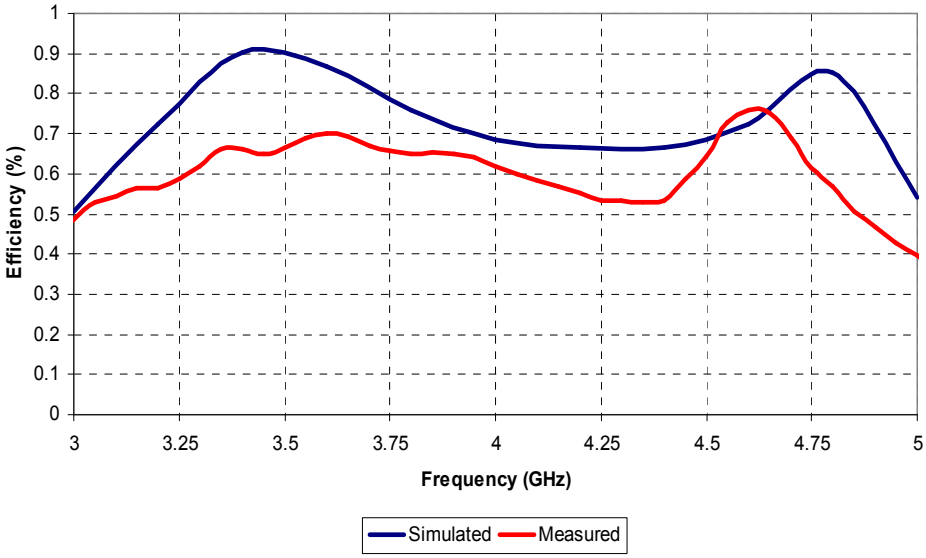

Fig. 6.5: Measured vs. Simulated Efficiency (%) vs. Frequency (GHz) for the matched Dual-PIFA Antenna

6.5 Far-Field Radiation Pattern Measurements

Fig. 6.6 shows a comparison of the radiation patterns of the measured dual-PIFA prototype vs. simulated data at the two resonant frequencies of 3.65GHz and 4.7GHz. The data is presented as 2-dimensional cuts of the 3-dimensional radiation pattern, taken on three orthogonal planes described around simple XYZ coordinates. As with the high-band UWB PIFA case, if we consider the mobile handset board to be in a horizontal position, the XY plane represents the Azimuth plane of the antenna and is the horizontal plane in parallel with the mobile handset board. The YZ plane is the vertical plane which cuts through the mobile handset board in parallel with its longer side. The XZ plane is the vertical plane which cuts through the mobile handset board in parallel with its shorter side. The diagrams in fig. 6.6 can be used as a guide to the planes of the 2D cuts.

Radiation Pattern 2D Cuts at 3.65GHz

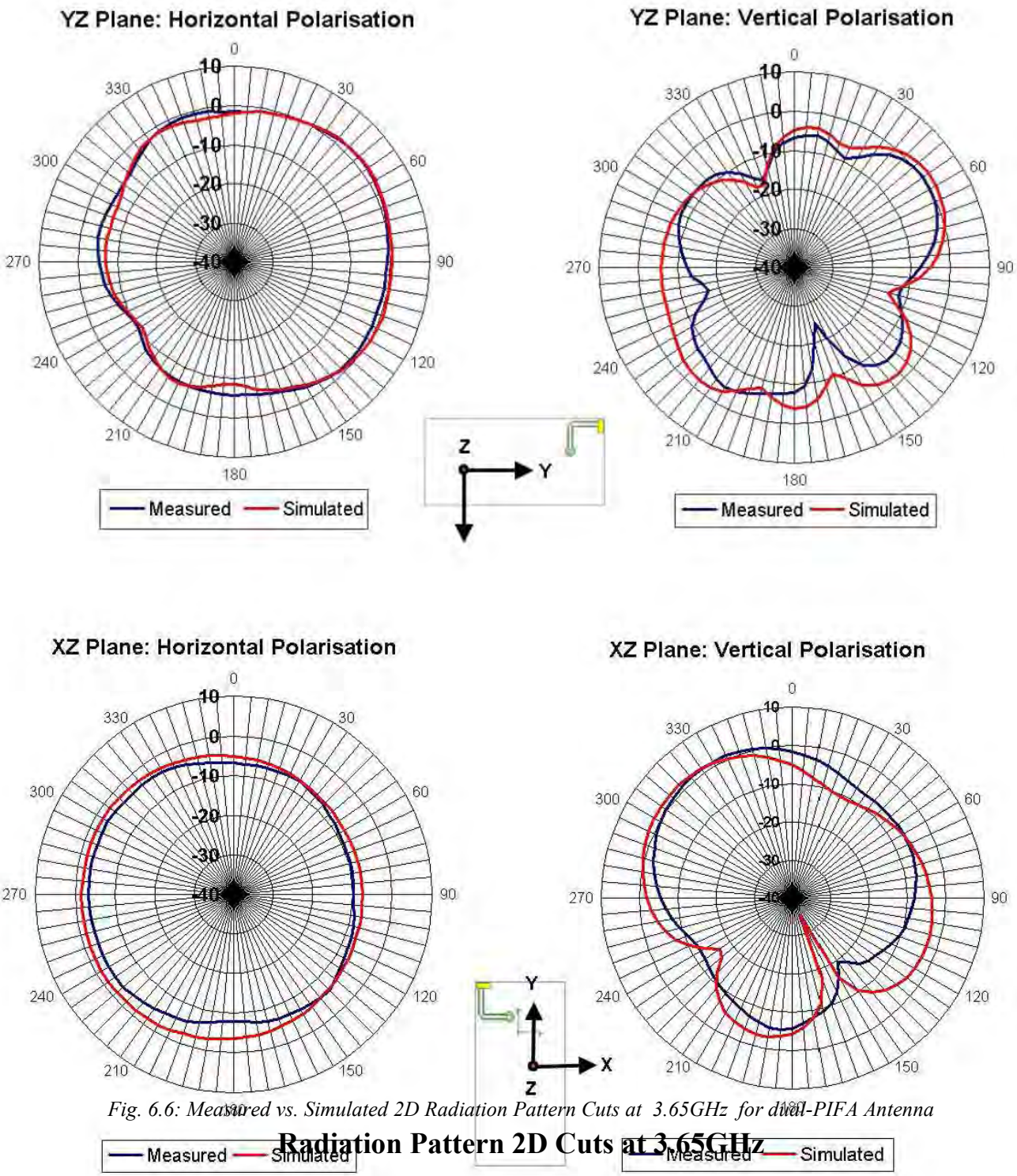

Fig. 6.6: Measured vs. Simulated 2D Radiation Pattern Cuts at 3.65GHz for dual-PIFA Antenna

Radiation Pattern 2D Cuts at 3.65GHz

Fig. 6.6: Measured vs. Simulated 2D Radiation Pattern Cuts at 3.65GHz for dual-PIFA Antenna

Radiation Pattern 2D Cuts at 3.65GHz

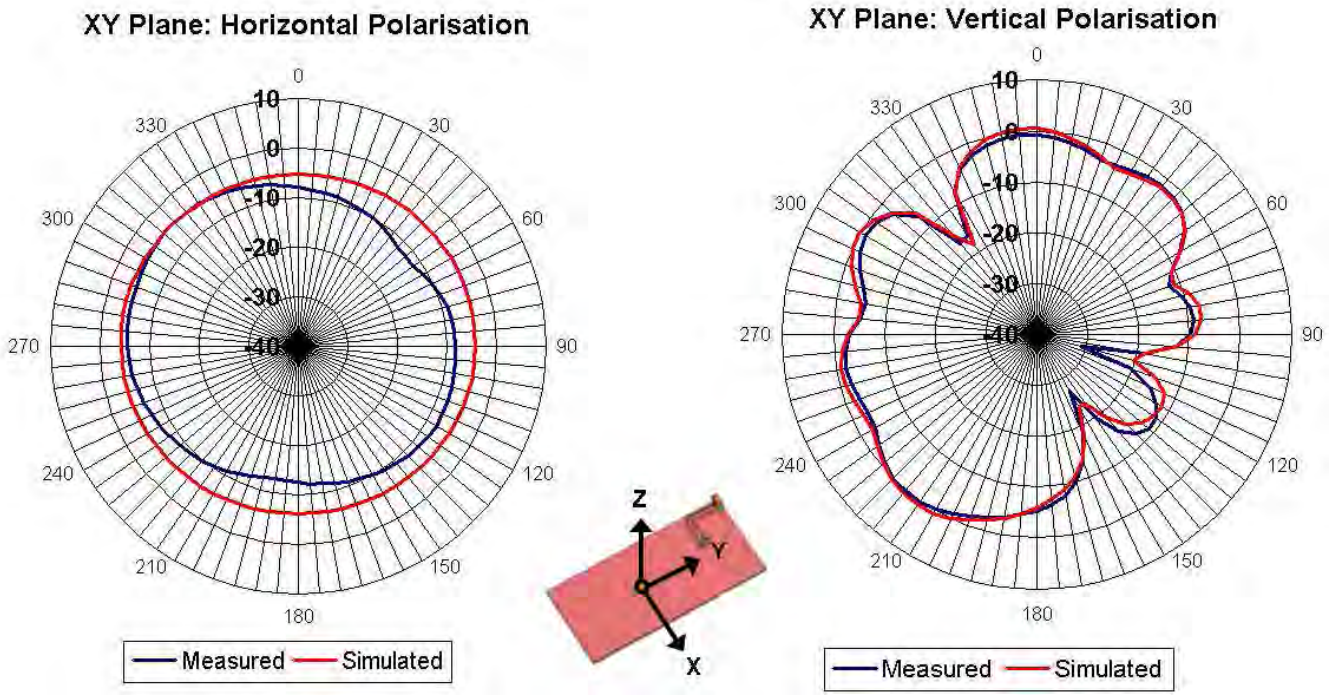

Radiation Pattern 2D Cuts at 4.7GHz

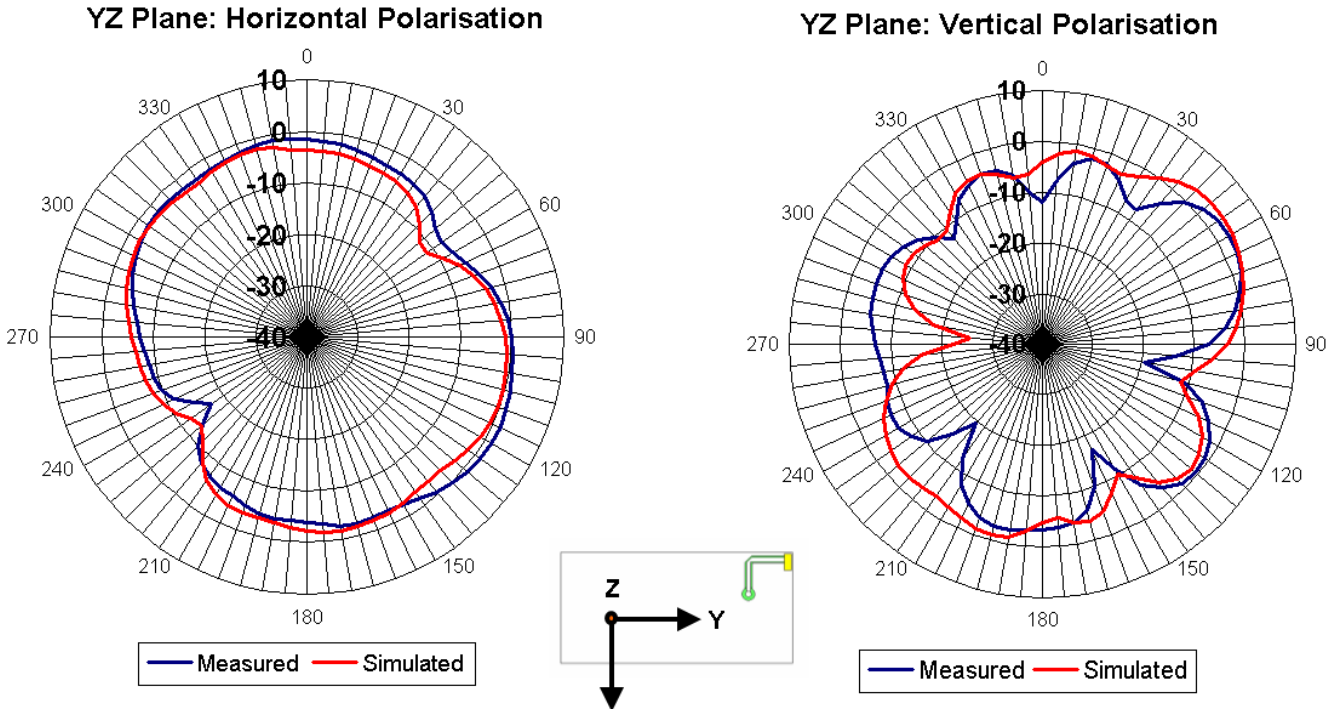

Fig. 6.6: Measured vs. Simulated 2D Radiation Pattern Cuts at 3.65GHz, 4.7GHz for dual-PIFA Antenna

Radiation Pattern 2D Cuts at 4.7GHz

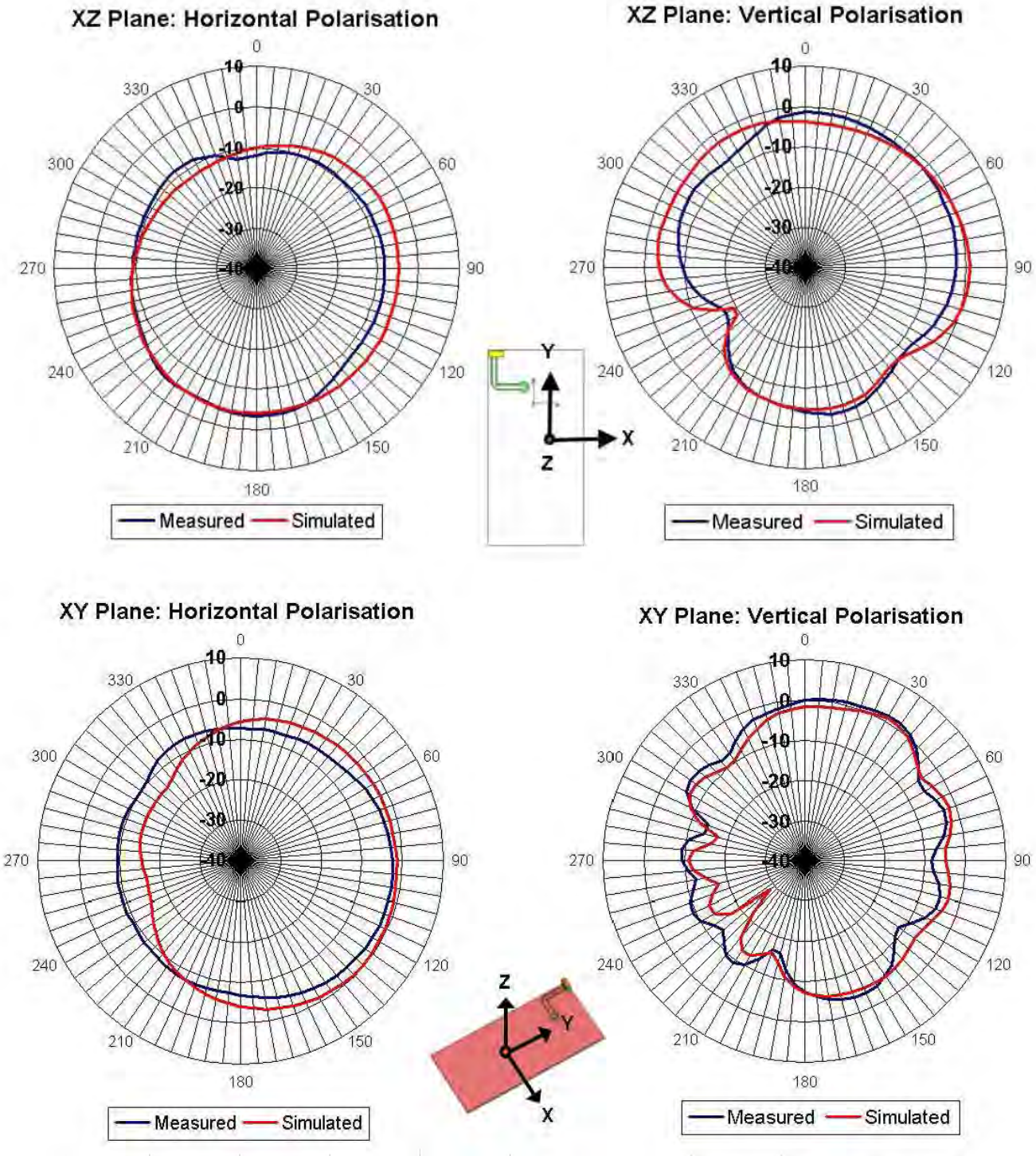

Fig. 6.6: Measured vs. Simulated 2D Radiation Pattern Cuts at 4.7GHz for dual-PIFA Antenna

Again, the radiation patterns are split into horizontal and vertical components for each cut and the data is plotted for each component separately. The data is plotted using polar coordinates with a scale ranging from -40dBi to +10dBi. Gain, directivity, pattern nulls and overall pattern shape can be clearly observed from the plots. Correlation between the measured data and simulated data predicted by CST can also be seen. It is worth noting that although only 3 cuts of the overall radiation pattern are presented, the measured efficiency was calculated using the full 3D pattern and so is an accurate representation of the total efficiency of the antenna.

As can be seen from the plots, correlation between measured and simulated radiation pattern data is good. Although some nulls are evident in the patterns of the vertical components, their overall shape is omni-directional and the patterns of the horizontal components are almost perfectly omni-directional. There are some more nulls in the patterns at the higher frequency, but overall the patterns look good.

A maximum measured gain of 4.08dBi is observed at 3.65GHz, in the direction orthogonal to the direction the radiating elements are pointing, as predicted by simulation. The simulation calculated a maximum gain of 4.6dBi in this direction, as described in chapter 5.6.3. At 4.7GHz a maximum measured gain of 3.41dBi is observed, which compares well with the simulated prediction of 3.15dBi.

6.6 Summary

Prototypes of the antenna proposed and simulated in Chapter 5 have been built up and measured to confirm the validity and accuracy of the simulation work. As with the high-band UWB PIFA antenna, the prototypes were built up using a screen-printing process to print the required pattern onto a ceramic block using aluminium paste. A ceramic of dielectric constant 7.5 was used and the block dimensions were 17.5mm x 6mm x 3mm.

Measurements were taken and the correlation between measured and simulated S11 was observed for the matched and unmatched antenna. The unmatched results correlated extremely well, while there was some discrepancy in

the matched results which is most likely due to inaccuracies in the ideal inductor and capacitor models used to simulate the matching network. Measured S11 confirmed that the antenna meets the specified -6dB across the entire band group 1 bandwidth.

Correlation between measured and simulated efficiency has also been presented for the matched antenna and measured results confirm the antenna provides greater than 50% efficiency across the 3.1 – 4.8 GHz bandwidth. Finally measured and simulated 2-dimensional cuts of the far-field radiation pattern show good correlation with a maximum measured gain of 4.08dBi at 3.65GHz and a maximum measured gain of 3.41dBi at 4.7GHz. The patterns also exhibit good omni-directional performance; in particular the horizontal components exhibit no nulls and a very smooth isotropic pattern.

Chapter 7:
Conclusions and Discussion

Two antenna designs have been investigated and presented which will support UWB functionality in a mobile phone handset environment. The first is a 6mm x 4mm x 2.4mm ceramic chip PIFA type antenna which covers UWB band groups 3 and 6 (6.3 – 9 GHz) and the second is a 17.5mm x 6mm x 3mm novel ceramic dual-PIFA antenna which covers UWB band group 1 (3.1 – 4.8GHz).

As has been shown, it is possible to design a small-size antenna with low profile, suitable for mobile handset integration, to cover these UWB bandwidths. Although electrically small antennas are limited by key theoretical considerations as discussed in the literature review (the trade-off between size, bandwidth and efficiency being the fundamental challenge for any small antenna design), by employing the dielectric loading properties of ceramic substrate materials and by utilizing novel PIFA structures, the desired UWB bandwidths can be achieved from what has traditionally been used for relatively narrow-band applications. Both antennas achieved the required S11 and Efficiency specifications across the bands of interest and both antennas exhibited omni-directional far-field radiation, ideal for use within a handset.

The surface currents, E-fields and far-field radiation patterns of both antenna designs have been presented and analysed to illustrate the operation of each antenna, and all simulated data has been verified using measured data. Measurement prototypes have been built up and their responses correlated well with the data predicted by simulation.

A technique of external matching has been described, which can prove invaluable when fine tuning an antenna response, even when the bandwidth of operation is very large as in the case of UWB. Measurement techniques using far-field and near-field measurement systems which were used over the course of this research have also been described and their various merits discussed.

UWB as a technology will likely see eventual albeit delayed market success when it is integrated into mobile phone handsets allowing very high data rates and a level of connectivity which will revolutionise the transfer of data between portable devices. This research has shown that it is realistically possible

to build a mountable chip antenna to support UWB functionality in a mobile handset environment within the size specified by handset vendors. In other devices which are not as size-restrictive, the potential antenna size could be much larger allowing for a broader bandwidth to be achieved or higher efficiency to be acquired. Again, the trade-off between size, bandwidth and efficiency is critical to any such design.

It has also been illustrated that a ceramic chip type antenna is a good option for UWB mobile handset integration due to its low cost, robustness and relative ease of manufacture. It is also ideal for mobile handset integration due to its versatility – either ceramic antenna described herein could easily be mounted at any location on a mobile handset board and any de-tuning effects negated by re-optimising the external matching circuit.

Although the same bandwidths cannot be as easily achieved from a PIFA type antenna as from a planar monopole, for example, the PIFA size is much smaller, and the structure allows for ground-plane to run directly under the antenna, allowing handset manufactures much more freedom when placing other components in the vicinity of the antenna.

It is likely some form of UWB integration into mobile handsets will be seen in the coming years and it is likely that ceramic chip antennas, and very possibly PIFA type structures will provide the necessary functionality required by these revolutionary devices.

References

[1] H.A. Wheeler, “Fundamental Limitations of Small Antennas”, *IRE Proc. 1947, 35, pp 1479-1484*

[2] H.A. Wheeler, “Small Antennas”, *IEEE Trans. Antennas Propagat., vol. AP-23, pp. 462-469, July 1975*

[3] L.J. Chu, “Physical Limitations of Omni-Directional Antennas”, *J. Appl. Phys., 1948, 19, pp. 1163-1175*

[4] R.F. Harrington, “Effect of Antenna Size on Gain, Bandwidth and Efficiency”, *J. Res. Nat. Bur. Stand., Vol. 64-D, pp.1-12 Jan/Feb 1960*

[5] J.S. McLean, “A Re-Examination of the Fundamental Limits on the Radiation Q of Electrically Small Antennas”, *IEEE Trans. Antennas Propag., 1996, AP-44 pp. 672-676*

[6] R.C. Hansen, ”Fundamental Limitations in Antennas”, *Proc. IEEE, 1981, 69, pp.170-181*

[7] R.C. Hansen, “*Electrically Small, Superdirective and Superconducting Antennas*” Wiley, 2006

[8] T. Herscovici, “Challenges in Modern Antenna Design”, Chelton Microwave Corp.

[9] F.F. Caimi, “Theoretical Size Constraints for Antennas based on Quality Factor, Q”, IEEE P802.15 Working Group for Wireless Personal Area Networks (WPANs), SkyCross, 2002

[10] R.W. Ziolkowski, A. Erentok, “At and below the Chu limit: passive and active broad bandwidth metamaterial-based electrically small antennas”, *IET Microw. Antennas Propag. 2007, 1, (1), pp. 116-128*

[11] J. Chang, "What is Happening with UWB", *Electronics Weekly Article*, pp 20 – 21, 3-9 December 2009

[12] D. McEuen, "The UWB Market Shakeout" ABI Research, Nov. 2008

[13] B. O'Rourke, "UWB 2008: Short-Term Problems and Long-Term Potential", Instat Research, Dec. 2008

[14] M. Bowles "Ultra-Wideband implementation issues" [Online] Available: http://www.wireless-usb.eu/wusb/?p=100

[15] J. Lansford, "UWB in the 6 to 10-GHz Spectrum Present opportunities and challenges", Sept 2008 [Online] Available: http://electronicdesign.com/Articles/Index.cfm?AD=1&ArticleID=19691

[16] S.M. Mishra, S. Brink, R. Mahadevappa, R.W. Broderson, "Detect and Avoid: An Ultra-Wideband/WiMAX Coexistence Mechanism", *IEEE Communications Magazine,* vol. 45, No. 6, pages 68-75, June, 2007

[17] Z.N. Chen, M.Y.W. Chia, "*Broadband Planar Antennas"*, Wiley, 2006

[18] C.A. Balanis "*Antenna Theory: Analysis and Design*", Wiley, 2005

[19] D.M. Nashaat, H.A. Elsadek, "Single Feed Compact Quad-Band PIFA Antenna for Wireless Communication Applications", *IEEE Trans. Ant. & Prop*., Vol. 53, pp 2631-2635, August 2005

[20] Z. Li, Y. Rahmat-Samii, T. Kaiponen, "Bandwidth study of a Dual Band PIFA on a Fixed Substrate for Wireless Communication", IEEE Antennas ad Propagation Society International Symposium, 2003, pp 435 – 438, Vol. 1

[21] D. Tsamakis, Z. Wu, "Modeling and Experimental Study of Dielectric Loaded Monopoles for UWB Applications", IEEE Antennas and Propagation Society International Symposium, 9-15 June 2007, pp 541 - 544

[22] Z.N. Chen, T.S.P. See, X. Qing, "Small Printed Ultra-wideband Antenna with Reduced Ground Plane Effect", *IEEE Trans. Antennas Propag.,* 2007, Vol. 55, Issue 2, pp. 383 – 388

[23] H.T. Chattha, Y. Huang, Y. Lu "PIFA Bandwidth Enhancement by Changing the Widths of Feed and Shorting Plates", *IEEE Antennas and Wireless Propagation Letters: Accepted for future publication* (IEEE Xplore 2009)

[24] N.C. Karmakar, "Shorting Strap Tunable Single Feed Dual-Band Stacked Patch PIFA", *IEEE Ant. & Prop. Letters*, Vol. 2, pp 68-71, 2003

[25] D. Kajfez, A.A. Kishk, "Dielectric Resonator Antenna – Possible Candidate for Adaptive Antenna Arrays", in Proceedings of the International Symposium on Telecommunications, Next Generation Networks and Beyond (VITEL '02), Portoroz, Slovenia, May 2002.

[26] K.L. Wong, "*Compact and Broadband Microstrip Antennas*", Wiley 2002

[27] D.M Nashaat, "Novel Ultra-Wideband and Multi-band Triangular Planar Inverted-F Antenna for Wireless Applications", *Microwave an Optical Technology Letters*, Vol. 49, No. 8, August 2007 pp 2039 - 2043

[28] I.T. Tang, D.B. Lin, W.L. Chen, J.H. Horng, C.M.Li, "Compact Five-Band Meandered PIFA by Using Meandered Slots Structure", IEEE Antennas and Propagation Society International Symposium, 9 – 15 June 2007, pp 653 - 656

[29] H.S. Yoon, S.O. Park, "A dual-band internal antenna of PIFA type for Bluetooth/WLAN in mobile handsets", IEEE Antennas and Propagation Society International Symposium, 9-15 June 2007, pp:665 – 668

[30] C. Holland, "Europe Approves UWB Regulations", *EE Times Europe*, May 3rd 2007

[31] J.D. Brunett, R.M. Ringler, V.V. Liepa, “On Measurements for EIRP compliance of UWB Devices”, International Symposium on Electromagnetic Compatibility, 2005.(EMC 2005) Volume 2, Issue , 8-12 Aug. 2005 pp 473 - 476